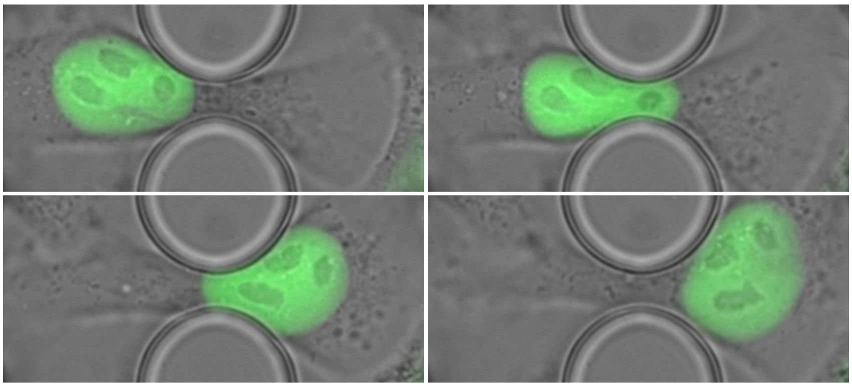

Studying cancer cell migration under confinement and with correlative microscopy

Joana Marques Pinto Monteiro

Thesis to obtain the Master of Science Degree in

Biomedical Engineering

Supervisor(s): Prof. Gabriel António Amaro Monteiro
Dr. Edgar Rodrigues Almeida Gomes

Examination Committee

Chairperson: Prof. João Miguel Raposo Sanches
Supervisor: Dr. Edgar Rodrigues Almeida Gomes
Member of the Committee: Dra. Ana Luísa Ferro Magalhães

November 2021

Declaration

I declare that this document is an original work of my own authorship and that it fulfills all the requirements of the Code of Conduct and Good Practices of the Universidade de Lisboa.

Preface

The work presented in this thesis was performed at the Edgar Gomes Lab of Instituto de Medicina Molecular João Lobo Antunes, Faculty of Medicine of the University of Lisbon (Lisboa, Portugal), during the period March-October 2021, under the supervision of Dr. Edgar Gomes and Dr. Francisco Calero-Cuenca. The thesis was co-supervised at Instituto Superior Técnico by Professor Gabriel Monteiro.

Acknowledgments

To Edgar Gomes I thank all of his support, help, and availability during these months, as well as his encouragement when it was needed. Thank you for this opportunity. I also thank Francisco Calero-Cuenca for showing me how to conduct a great part of my work, and for helping me and guiding me through the whole process. To professor Gabriel Monteiro I thank his guidance and his availability for clarification of all of my doubts.

To my lab mates I want to thank all the support and help when it was needed. I want to thank Cátia Janota in particular for her help in the maintenance of cells for my work, Raquel Pereira for showing me how to perform SRRF and discussing my work with me, and David Barata for always being available to help with engineering-related matters.

I would like to thank Pedro Pereira for giving me material to build NanoJ-Fluidics and for helping me whenever I needed. I would also like to thank Ricardo Henriques for his help and for providing the 3D-printed pieces to build the pumps.

To my family I want to thank all of their support and for believing in me. Thank you for caring for me and for providing me everything that I needed to get where I am.

To my friends, I thank all of their understanding and support when it was needed. Thank you for helping me even without request and for believing in me. Thank you for all the joyful moments and for making things easier.

Last, but not least, I want to thank Rodrigo for his support during this time, and for giving me tranquility when it was needed.

Resumo

Vários fenómenos clinicamente relevantes implicam a migração de células cancerígenas, tal como a metastização de tumores. Por isso, é particularmente importante estudar a migração destas células em ambientes tri-dimensionais fisiologicamente pertinentes. Neste trabalho, a migração de células de cancro da mama MDA-MB-231 através de constrições físicas foi estudada, através do uso de dispositivos de polidimetilsiloxano (PDMS) contendo microconstrições de larguras 2, 3 e 5 µm. Tendo em conta que as proteínas Eps8L2 e Ctdnep1 estão envolvidas em migração celular bi-dimensional, investigou-se o papel destas proteínas em migração tri-dimensional. A duração de três períodos de transmigração – enter, cross e exit – foi calculada. Foi observado que a migração celular através de constrições implica a deformação nuclear, especialmente para constrições mais estreitas. Constrições de tamanhos diferentes não mostraram afetar a dinâmica de migração nuclear. Notavelmente, o período exit foi, em média, mais curto do que o período enter para constrições mais estreitas. Não foi possível avaliar o papel das proteínas Eps8L2 e Ctnep1 na migração celular tri-dimensional devido a dados insuficientes. Foi também implementado um procedimento de microscopia correlativa para o estudo de dinâmica celular, usando imagens de contraste de fase para células vivas seguida de imagens de fluorescência e super-resolution radial fluctuations (SRRF) para células fixadas. Particularmente, o sistema NanoJ-Fluidics foi construído para executar automaticamente a coloração de fibroblastos NIH 3T3. Com este procedimento, foi possível correlacionar dinâmica celular com informação estrutural subjacente. As estratégias apresentadas neste trabalho podem abrir o caminho para mais estudos sobre migração de células cancerígenas.

Palavras-chave: cancro, migração celular, constrições, deformação nuclear, microscopia correlativa

Abstract

Cancer cell migration is implicated in several clinically relevant phenomena, namely the formation of metastasis. It is then important to study the mechanisms involved in the migration of cancer cells, particularly in physiologically relevant 3D environments. In this work, we studied the migration of MDA-MB-231 breast cancer cells under confinement using polydimethylsiloxane (PDMS) devices comprising microconstrictions of different widths (2, 3 and 5 µm). Since Eps8L2 and Ctdnep1 were found to be involved in 2D cell migration, we investigated the role of these proteins in 3D cell migration. We calculated the duration of three nuclear transmigration periods – enter, cross and exit. We observed that nuclear deformation was necessary for confined cell migration, especially for narrower constrictions. However, we did not find an effect of constriction size in nuclear migration dynamics. Notably, the exit period of nuclear transmigration was, on average, shorter than the enter period for cells migrating across 2 and 3 µm-wide constrictions. It was not possible to assess the role of Ctdnep1 and Eps8L2 in confined cell migration due to insufficient data. Moreover, we implemented a correlative microscopy workflow for the study of cell dynamics, consisting in phase contrast live-cell imaging followed by fluorescence and super-resolution radial fluctuations (SRRF) imaging. Particularly, the NanoJ-Fluidics system was assembled to perform automatic staining of NIH 3T3 fibroblasts. Using this workflow, we successfully correlated cell dynamics with its underlying structural information. The strategies presented in this work can pave the way for further studies on cancer cell migration.

Keywords: cancer, cell migration, confinement, nuclear deformation, correlative microscopy

Contents

Acknowledgments v
Resumo vii
Abstract ix
List of Figures xiii
List of Acronyms xv

1 Introduction **1**
1.1 Motivation 1
1.2 Methodology and Objectives 2
1.3 Thesis Outline 2

2 Background **5**
2.1 Cancer and cell migration 5
  2.1.1 Metastatic cancer 5
  2.1.2 Mechanisms of two-dimensional cell migration 5
  2.1.3 Mechanisms of three-dimensional cell migration 8
2.2 Platforms to study confined cell migration 12
  2.2.1 Three-dimensional hydrogels 13
  2.2.2 Microfabricated devices 13
  2.2.3 Three-dimensional bioprinting 16
2.3 Correlative microscopy for the study of cell migration 16
  2.3.1 NanoJ-Fluidics - a system for automated multimodal microscopy 18
  2.3.2 Super-resolution imaging - SRRF 19

3 Materials and Methods **21**
3.1 Cell culture 21
3.2 Production of MDA cell lines expressing NLS-GFP and LifeActin-mcherry 21
3.3 siRNA transfection in MDA cells 22
3.4 Migration devices fabrication 22
3.5 Preparation of devices and cell seeding 23
3.6 Preparation of devices for microscopy 25
3.7 Imaging of cells in migration devices 25

3.8 Analysis of images from cell migration in PDMS devices 26
3.8.1 Statistical analysis 27
3.9 Assembly of pumps for correlative microscopy with NanoJ-Fluidics 28
3.10 Pump control electronics hardware 30
3.11 Pump control firmware and software 30
3.12 NanoJ-Fluidics labware 30
3.13 Pump usage 31
3.14 Pump calibration 31
3.15 Live imaging of NIH 3T3 fibroblasts 32
3.16 Staining protocol used for experiments with NanoJ-Fluidics 33
3.17 Imaging of fixed cells 35
3.18 SRRF imaging of fixed cells 36

4 Results 37
4.1 MDA cells migrating through 2, 3 and 5 µm-wide constrictions 37
4.2 Measurement of microconstriction widths 39
4.3 Confined migration of MDA cells transfected with control siRNA 40
4.4 Effect of siRNA transfection in MDA cells for confined nuclear migration 42
4.5 Widefield images from correlative microscopy experiments 44
4.6 SRRF imaging of fixed cells 47

5 Discussion 49
5.1 Aspects affecting quantification of MDA cell migration in PDMS devices 49
5.2 Size and shape of constriction pillars in migration devices 51
5.3 Confined migration of MDA cells transfected with control siRNA 52
5.3.1 Effect of constriction size in nuclear migration periods 52
5.3.2 Differences between nuclear migration periods 54
5.4 Role of Ctdnep1 and Eps8L2 in migration of MDA cells under confinement 56
5.5 Performance of NanoJ-Fluidics in correlative microscopy 56

6 Conclusions 61
6.1 Achievements 61
6.2 Limitations and Future Work 62

Bibliography 65

A Additional Materials 73
A.1 LEGO® pieces used for the assembly of syringe pumps 73

List of Figures

3.1 Images from the PDMS devices used to study cell migration under confinement 24

3.2 Representation of four key time points considered for confined nuclear migration 27

3.3 Two versions of LEGO® pumps assembled for NanoJ-Fluidics 29

3.4 Values from the calibration of syringe pumps 32

3.5 NanoJ-Fluidics set-up for correlative microscopy experiments 34

3.6 Staining protocol defined in the NanoJ-Fluidics GUI 36

4.1 MDA cells transfected with control siRNA migrating through PDMS microconstrictions . . 38

4.2 MDA cells transfected with Eps8L2 siRNA migrating through PDMS microconstrictions . . 39

4.3 MDA cells transfected with Ctdnep1 siRNA migrating through PDMS microconstrictions . 40

4.4 Constriction widths measured for cells whose nuclear migration dynamics were quantified 41

4.5 Nuclear migration periods for MDA cells transfected with control siRNA (data grouped by period) 41

4.6 Nuclear migration periods for MDA cells transfected with control siRNA (data grouped by constriction size) 42

4.7 Nuclear migration periods for MDA cells transfected with control, Eps8L2 and Ctdnep1 siRNA - 2 µm-wide constrictions 43

4.8 Nuclear migration periods for MDA cells transfected with control, Eps8L2 and Ctdnep1 siRNA - 3 µm-wide constrictions 43

4.9 Nuclear migration periods for MDA cells transfected with control, Eps8L2 and Ctdnep1 siRNA - 5 µm-wide constrictions 44

4.10 Widefield images of a ”static” cell obtained with correlative microscopy 45

4.11 Widefield images of a ”dynamic” cell obtained with correlative microscopy 46

4.12 Widefield and SRRF images of a ”static” cell 47

4.13 Widefield and SRRF images of a ”dynamic” cell 48

A.1 Part 1 of list of LEGO® pieces used to assemble pumps for NanoJ-Fluidics 74

A.2 Part 2 of list of LEGO® pieces used to assemble pumps for NanoJ-Fluidics 75

A.3 Part 3 of list of LEGO® pieces used to assemble pumps for NanoJ-Fluidics 76

A.4 Part 4 of list of LEGO® pieces used to assemble pumps for NanoJ-Fluidics 76

A.5 Part 5 of list of LEGO® pieces used to assemble pumps for NanoJ-Fluidics 77

List of Acronyms

2D	Two-Dimensional
3D	Three-Dimensional
Ctdnep1	C-terminal domain nuclear envelope phosphatase 1
DNA	Deoxyribonucleic Acid
ECM	Extracellular Matrix
Eps8L2	Epidermal growth factor receptor kinase substrate 8-like protein 2
FBS	Fetal Bovine Serum
GFP	Green Fluorescent Protein
GUI	Graphical User Interface
HGF	Hepatocyte Growth Factor
LINC	Linker of Nucleoskeleton and Cytoskeleton
MMP	Metalloproteinase
NLS	Nuclear Localization Signal
PBS	Phosphate-Buffered Saline
PDMS	Polydimethylsiloxane
PFA	Paraformaldehyde
siRNA	small interfering Ribonucleic Acid
SRM	Super-Resolution Microscopy
SRRF	Super-Resolution Radial Fluctuations
TAN	Transmembrane Actin-associated Nuclear

Chapter 1

Introduction

1.1 Motivation

Breast cancer is the most common malignancy in women [1], being the most prevalent type of cancer in the world [2]. Metastasis formation is the primary cause of death from cancer [2], in particular for the case of breast cancer, which has a high metastatic potential [3]. Since cancer cell migration is a key event in the formation of metastasis, the study of this topic is of high relevance in order to better understand the mechanisms involved in this process. Moreover, cancer cells encounter complex three-dimensional (3D) environments while migrating in enclosed spaces in the body, for example when passing across narrow openings, such as endothelial junctions for blood vessel intravasation and extravasation, and squeezing through tight pores of the tumor stroma extracellular matrix [4]. As such, it is particularly relevant to study cancer cell migration under confinement, through the use of appropriate systems recreating the complex 3D environments where migrating cancer cells can be found *in vivo*. Studying the characteristics and mechanisms involved in single-cell migration in confined spaces can then contribute to a better understanding of cancer progression, with special emphasis on aspects such as plasticity, heterogeneity and drug-resistance, which are of high clinical relevance [4].

A variety of proteins have been found to play important roles in mechanisms involved in cell migration. For example, Ctdnep1, a nuclear envelope phosphatase, and Eps8L2, an actin regulator, were found to be involved in nuclear positioning for two-dimensional (2D) mouse fibroblast migration [5]. However, to our knowledge, the role of these proteins in 3D migration has not been studied yet. It is therefore pertinent to assess whether these proteins are also involved in cell migration in confined spaces. In particular, it is important to perform these studies in human cancer cells, in order to increase the clinical relevance of the obtained findings.

The mechanisms driving cell migration are complex and intricate, especially in 3D settings, where more environmental variables are involved. Cellular structures interact with one another and with the surrounding environment to drive the necessary dynamics for cell migration. Bearing these aspects in mind, it is essential not only to study the observable dynamics of migrating cells, but also understand which structures are involved and how they interact in mechanisms driving these dynamics. Therefore, it is important to devise convenient approaches for the study of cell migration which enable the correlation of cell dynamics during migration and the structures that play a role in such dynamics. This could be performed in complement to studies of cell migration under confinement using appropriate systems. Applied to cancer, this can allow a better understanding of how certain phenomena involved in cell migration for the formation of mestastasis occur and what cellular elements are involved in the respective mechanisms. Such knowledge can then be used, for example, in the development of new drugs or devisal of preventive measures for the metastasis formation.

1.2 Methodology and Objectives

In this work, different strategies were employed for the study of cancer cell migration. To investigate on breast cancer cell migration under confinement, we used microfabricated devices made of polydimethylsiloxane (PDMS) comprising microconstrictions of different widths. In particular, we used MDA-MB-231 cells, a highly metastatic breast cancer cell line, expressing NLS-GFP and LifeActin-mcherry for better visualization of the nucleus and actin filaments, respectively. In order to assess the role of Ctdnep1 and Eps8L2 in confined cancer cell migration, MDA-MB-231 cells were treated with small interfering RNA (siRNA) to perform the knockdown of these to proteins, as well as with a third siRNA for control. Cells were imaged while migrating across the microconstrictions of the devices with both brightfield and fluorescence widefield microscopy. We then quantified nuclear migration dynamics, namely the duration of nuclear transmigration across the microconstrictions, divided into three periods - enter, cross, and exit. Hence, the main objectives of this workflow were, on one hand, to observe the dynamics of cell transmigration across microconstrictions, and, on another hand, to assess the role of Ctdnep1 and Eps8L2 in the migration of MDA-MB-231 breast cancer cells under confinement, as well as understand the effect of constriction size on cell transmigration dynamics.

Moreover, we devised a correlative microscopy workflow for the study of cell dynamics using phase contrast live-cell imaging followed by fluorescence and super-resolution fixed-cell imaging. In particular, the NanoJ-Fluidics system [6] was built and used to perform automatic staining of NIH 3T3 fibroblasts. Super-resolution radial fluctuations (SRRF) images were posteriorly generated to visualize with more detail certain cellular structures, as well as to assess the potential of the established correlative microscopy set-up for the performance of super-resolution microscopy. The main objectives of this workflow were, therefore, the assembly of a practical system capable of correlating cell dynamics with its underlying structural information and evaluate its applicability for the study of cancer cell migration.

1.3 Thesis Outline

In the following chapters, the topics described above will be detailed in what pertains to their background, implementation for this work, obtained results and respective discussion, and the main conclusions that could be drawn. In the Background chapter, an overview on cancer and cell migration is provided, with particular focus on metastatic cancer and the mechanisms involved in both 2D and 3D cell migration. We then present a view on the current platforms that are used for the study of confined cell migration, focusing on 3D hydrogels, microfabricated devices and 3D bioprinting. Finally, we briefly explore the use of correlative microscopy for the study of cell migration, discussing the NanoJ-Fluidics system and super-resolution microscopy approaches that can be used in correlative microscopy, with special emphasis on SRRF.

In the Materials and Methods chapter, we detail the materials and the methodologies that were employed in this work for the achievement of the proposed objectives. In particular, we first describe how the MDA-MB-231 and NIH 3T3 cell lines were created, maintained, and/or transfected with siRNA, and how the devices used for the study of confined cell migration were fabricated and prepared. We then specify how the imaging of MDA-MB-231 cells migrating in the devices was performed, and how the respective resulting images were processed and analyzed. Moreover, we describe how we assembled and installed the NanoJ-Fluidics system, as well as the materials that were used. Finally, we detail the correlative microscopy imaging workflow that was employed to image NIH 3T3 fibroblasts and how the respective SRRF images were generated.

In the Results chapter, we show images of MDA-MB-231 cells transfected with different siRNAs migrating through microconstrictions of different sizes, as well as the measurements obtained for the constriction widths of cells whose nuclear dynamics were quantified. We then exhibit plots with the data resulting from the quantification of nuclear transmigration periods, firstly only for cells transfected with control siRNA, and after for cells transfected with all siRNAs, grouped by constriction size. We then display images obtained with the correlative microscopy experiments using NIH 3T3 fibroblasts, namely for two example cells exhibiting different dynamics, together with the corresponding SRRF images that were constructed.

In the Discussion chapter, we discuss several topics pertaining to the results shown in their dedicated chapter. Firstly, we address the aspects that affected the quantification of cell migration across microconstrictions and comment on the morphology of the microstructures in the migration devices. We then discuss the effect of constriction size in the nuclear migration periods, as well as differences among each period, for cells transfected with control siRNA. The role of Ctdnep1 and Eps8L2 in the migration of these cells under confinement is also discussed. Lastly, we reflect on the performance of NanoJ-Fluidics in the correlative microscopy experiments.

Finally, in the Conclusions chapter, we summarize the main achievements of the present work and comment on limitations associated with it. Moreover, we reflect on future work that could be performed in light of the present topics.

Chapter 2

Background

2.1 Cancer and cell migration

2.1.1 Metastatic cancer

Breast cancer is the most prevalent cancer in the world, with 2.26 million cases having been found in 2020 [2], and is the most common malignancy in women all over the world [1]. Widespread metastases are the primary cause of death from cancer [2]. In the case of breast cancer, which has a high metastatic potential [3], there were 685 000 deaths from this disease in 2020 [2]. Metastasis occurs when cells from the primary tumor escape from it and travel in the blood or lymph vessels to then extravasate into another tissue, initiating the development of a new tumor [7, 8]. Therefore, cell migration is of utmost relevance for the metastatic process [8]. However, factors such as the heterogeneous nature of the microenvironments that cancer cells come across when migrating *in vivo* as well as of the cancer cells themselves in the primary tumor and metastases, together with the diversity of migration mechanisms employed by cancer cells, hinder the treatment and prevention of metastases in the clinical setting [7, 8]. Hence, it is critical to study cancer cell migration in a wide range of setting and complexities to deeply understand how metastasis are formed and how their occurrence can be prevented or treated. Specifically, because metastasis is a phenomenon in which individual cancer cells break from the primary tumor to migrate and invade other tissues, it is relevant to study single-cell migration rather than collective cell migration [4]. For this, and in the context of breast cancer, MDA-MB-231 cells, a highly metastatic breast cancer cell line, are commonly used to study cancer cell migration [3].

2.1.2 Mechanisms of two-dimensional cell migration

The characteristics of cell migration, including the mode of migration, are influenced by several factors, such as the cell type and the physical and biochemical properties of the extracellular matrix (ECM) [9]. Different modes of single-cell migration in two dimensions, including the mesenchymal and amoeboid modes, are characterized by distinct properties, namely relative to cytoskeleton dynamics, adhesion and morphologies [9–11]. In mesenchymal migration, cells usually exhibit actin-rich protrusions, which can be the classic flat lamellipodia or thin elongated filopodia, and adhere strongly to the ECM through focal adhesions (mediated by integrins) by turn connected to the extremities of actomyosin stress fibers, resulting in slow migration speeds [9, 11]. On another hand, amoeboid migration is characterized by rounded cell shapes, weak or no adhesion to the ECM and absence of mature focal adhesions and stress fibers, being much faster than the mesenchymal migration mode [9, 11, 12]. To migrate in this mode, cells either use actin-driven finger-like protrusions (pseudopods) or employ a contraction-based migration with the formation of blebs [9, 11, 13]. There are many factors contributing to the mode of migration, as well as its efficiency and purpose, that is employed by a cell [9, 10]. These include, essentially, cellular determinants, such as cytoskeleton organization, cell deformability, cell-cell adhesions and cell-ECM adhesion, and tissue determinants, such as the spectrum of ligands surrounding the cell and the physical characteristics of the environment [10].

Cytoskeletal dynamics driving two-dimensional migration

In short, 2D single-cell migration can be defined as a process of multiple sequential steps where the microtubules, intermediate filaments and actin microfilaments, comprising the cytoskeleton, interact and coordinate in a cyclic manner themselves to provide the necessary dynamics that allow cells to move [9, 13]. Despite the intricate continuous interplay among these cytoskeleton components, a cycle of mesenchymal cell migration can be roughly divided into five steps: cell front-rear polarization, protrusion formation at leading edge, establishment of new adhesions, contraction of cell body, and retraction of the cell rear [9, 11, 13]. The three cytoskeletal networks, namely microtubules, intermediate filaments and actin filaments, polarize in the direction of migration [9]. The Golgi apparatus and centrosome, as microtubule organizing centers, often localize in front of the nucleus in mesenchymal migration, stimulating microtubule expansion in the direction of the cell front [9, 14]. Microtubules play an important role in cell polarity as microtubule-dependent transport aids in the delivery of molecules to the leading edge of the cell, which by turn participate in the process of microenvironment-sensing, as well as in the control of focal adhesions dynamics and cell locomotion directionality and speed [9]. The formation of protrusions is crucial for cell migration as they provide the generation of forces at the leading edge of the cell, at the same time sensing mechanical and chemical cues to drive migration directionality [11, 13]. The forces generating the formation of protrusions arise from actin polymerization at the cell front [9, 11, 13], which is stimulated by Rho-family GTPases, primarily Cdc42 and Rac1, and signaling lipid phosphatidylinositol trisphosphate [15]. Small focal adhesions initially form at the leading edge, turning afterwards into mature focal adhesions connected to the extremities of actomyosin stress fibers, with the help of microtubule-mediated vesicle transport to the cell front [9, 13]. For the cell body to contract, it is essential that actin associates with myosin II, allowing the establishment of stress fibers anchored to focal adhesions along which contractile forces are generated [9, 13]. Microtubules mediate the transport of vesicles containing RhoGTPase signaling molecules to the cell front, which, together with interactions between the three cytoskeletal networks, regulate actomyosin contractility [9]. Studies have suggested that intermediate filaments contribute to the maintenance of cell and organelle integrity during actomyosin contraction [9]. Additionally to the establishment of actomyosin stress fibers, there is the occurrence of retrograde flow of the actin network towards the cell rear, which is caused by mechanical resistance of the plasma membrane [9, 11]. With contraction of the cell body, mature focal adhesions dismantle from the cell rear, thus allowing the cell rear to detach from the substrate [9, 13]. The cell rear then retracts and the forces resulting from actin polymerization and retrograde flow allow the cell to move forwards [9, 11].

In the case of amoeboid migration, the process is similar to that of mesenchymal migration, following the same steps overall, although with a few variations [13]. In addition to the differences between these two migration modes described above, protrusion formation in blebbing amoeboid migration is driven by forces arising from changes in hydrostatic pressure, which originate from local variations in myosin contractility [11]. These contractile traction forces are applied across the whole cell body, namely front, back, and the sides, resulting in highly motile locomotion [13]. Moreover, in opposition to mesenchymal migration, cells migrating in an amoeboid manner commonly experience changes in the direction of migration in an apparently random fashion, which may be explained by changes in the pool of available actin monomers employed by the cell [16]. However, the mechanisms of amoeboid migration are not as well understood as those of mesenchymal migration, and therefore more research on this subject is needed [12, 16].

Nuclear positioning during two-dimensional migration

The position and structure of the nucleus is crucial for the proper migration of a variety of cell types [17]. As several organelles and the cytoskeleton need to be arranged inside the cell for the establishment of polarity in the direction of migration, nuclear positioning is also particularly important for this process, namely for mesenchymal cells, neurons, fibroblasts and most cancer cells [17]. In particular, the nucleus is positioned to the cell rear, which is driven by a retrograde flow of actin moderated by Cdc42 and myosin [17, 18]. In order to guide the nucleus towards the cell rear, retrograde moving dorsal actin cables are connected to the nuclear envelope via the LINC complex, which is composed of SUN proteins, present in the inner nuclear membrane, and nesprin, present in the outer nuclear membrane [17, 19, 20]. In particular, SUN proteins in the inner nuclear membrane bind to Lamin A/C, present in the nuclear lamina, thus providing a stable connection of the LINC complex to the nucleus [17]. Lamin A/C is also involved in the modulation of nuclear rigidity and shape [17, 21]. Additionally, Transmembrane Actin-associated Nuclear (TAN) lines connecting the dorsal actin cables to the LINC complex, being composed of actin filaments, Nesprin-2 and SUN2, allow for the actin retrograde flow to guide nuclear positioning [17, 20]. The translocation of the nucleus together with the cell body during migration occurs with the help of myosin II in actomyosin fibers, by pulling and pushing the nucleus [17, 22].

Role of Ctdnep1 and Eps8L2 in two-dimensional cell migration

The protein Ctdnep1 (CTD nuclear envelope phosphatase 1; or Dullard) [23] is a serine/threonine phosphatase present in the nuclear envelope [5, 24]. This protein is involved in the regulation of neural tissue in development [5, 25] and nuclear membrane biogenesis [5, 24]. Additionally, it has been shown that the Ctdnep1 gene might be a suppressor gene for medulloblastoma progression, which is the most frequent type of malignant brain tumor in children [5, 23, 24]. Eps8L2 (Epidermal growth factor receptor kinase substrate 8-like protein 2) is a protein member of the Eps8 family [26]. This protein family is involved in the capping and bundling of actin filaments, playing a role in filopodia and lamellipodia generation and transduction signal for Rac activation (RhoGTPases), resulting in actin remodeling for cell migration [5, 27, 28]. Eps8L2 has been found to be upregulated in bladder cancer [26], progressive renal cell carcinoma [29], and endometrial carcinoma [30]. Additionally, Eps8 was found to be overexpressed in breast cancer [31].

In NIH 3T3 fibroblasts migrating in two dimensions, Calero-Cuenca et al. (2021) found Ctdnep1 and Eps8L2 to be involved in nuclear positioning and cell migration, since their depletion with siRNA resulted in the inhibition of nuclear positioning and less cell migration in comparison to control [5]. Moreover, the authors found that Ctdnep1 and Eps8L2 interact directly and that this interaction is involved in nuclear positioning and cell migration [5]. Additionally, it was found that these two proteins have a role in the formation and maintenance of dorsal actin cables, which are by turn required for the formation of TAN lines that participate in nuclear positioning in the migration of fibroblasts [5]. It is currently unknown whether these two proteins are involved in cell migration on a 3D environment.

2.1.3 Mechanisms of three-dimensional cell migration

Cell migration in two dimensions is a fairly well-described subject for a wide range of cell types, given its simplicity of implementation *in vitro* and relative ease of cellular structures analysis in this setting. However, a variety of cell migration phenomena occurring *in vivo*, namely the migration of cancer cells for the formation of metastases, cannot be completely understood merely via the performance of studies in two dimensions. Specifically, for the case of cancer cells, they experience confinement *in vivo* as 1) tumor growth often induces cells to undergo high levels of confinement and 2) cell invasion for metastasis formation frequently implicates squeezing through tight pores of the ECM of the tumor stroma and cell passage across narrow spaces, such as endothelial junctions for blood vessel intravasation and extravasation [4]. Therefore, it is of utmost relevance to study the mechanisms of cell migration in a 3D environment in order to better understand phenomena involving cell migration *in vivo*, in particular the migration of cancer cells for the formation of metastases.

It is known that the environment in which cells are found *in vivo*, often the ECM, has a significant impact in the regulation of cell behavior, namely in conditioning cell migration and modulating cell morphology in 3D environments, as well as phagocytosis and cell division [9, 15]. Moreover, cells are highly adaptive to their environment, employing and changing between a variety of migration modes in different contexts [9, 15]. In the past years, research has been carried out in order to better understand the mechanisms that underlie the cellular responses to 3D environments [9]. As opposed to migration in a 2D environment, 3D migration is highly reliant on environmental factors, which can be sub-categorized into mechanical (matrix rigidity and viscosity), chemical (degradability of the substrate, chemical cues and adhesive ligands) and geometrical (matrix pore size and topology) [9, 15]. To sense the properties of the environment, cells use integrins, employing a migration strategy based on the probing of different regions of the neighboring ECM beforehand [9]. Cells undergoing confinement often degrade the ECM and remodel the matrix by protease activity in order to properly migrate through obstacles [9]. Different modes of migration in a 3D environment, as well as the adhesion properties that cells exhibit, are modulated by RhoA-ROCK-mediated actomyosin contractility [9].

Strategies employed by cells during three-dimensional migration

Additionally to the mesenchymal and amoeboid modes of migration that have been described for 2D single-cell migration, cells can also employ a third mode of migration in 3D environments, conserving the subjacent fundamentals of force generation and transmission: a lobopodial type of migration [9, 15]. The known cell migration modes exhibit a few differences depending on whether the environment is two- or three-dimensional [15]. In the case of 3D mesenchymal migration, in addition to what was mentioned in subsection 2.1.2, the centrosome of the cell localizes in front of the nucleus and cells demonstrate a high ability for matrix degradation, whereas in 3D amoeboid migration the centrosome often localizes behind the nucleus and cells display low protease activity [9, 15]. In lobopodial migration, which can be seen as a hybrid between the mesenchymal and amoeboid migration modes, cell exhibit blunt protrusions similar to blebs named lobopodia, which are formed using hydrostatic pressure, nuclear pistoning and actomyosin contractility [9, 15]. Additionally, cells migrating in the lobopodial mode are highly adherent to the ECM and display very low protease activity [9, 15]. Moreover, cells migrating in the amoeboid and lobopodial modes demonstrate high RhoA-ROCK-MyoII contractility, while cells migrating in the mesenchymal mode demonstrate low RhoA-ROCK-MyoII contractility [9].

Notably, cells migrating in three dimensions have the ability to rapidly alternate between the different modes of migration. For example, if cells experience a high degree of confinement and exhibit high actomyosin contractility, by forming less adhesions to the matrix they can change from a mesenchymal to an amoeboid mode of migration [9, 15].

As cells exhibiting a mesenchymal mode of migration have high proteolytic activity and strong adhesion to the substrate, they are capable of ECM degradation and or modification when migration through confined environments. However, for the case of cells migrating in the amoeboid mode, hence exhibiting low capacity for ECM degradation and weak adhesion to the substrate, the ability to degrade or rearrange ECM fibers is limited. Hence, these cells often employ strategies to adapt to the microenvironment, migrating through tissues by choosing the path of least resistance [15].

In vivo, cells can encounter gaps with diameters ranging from 0.1 to 30 µm, which is, depending on the cell type, either proportionate to the size of the cell or considerably smaller [32]. In general, there are two main mechanisms that cells employ to migrate through confined spaces: expanding the constriction by proteolytic degradation and/or physical remodeling of the ECM or alteration of cell shape and stiffness to fit in the gap [32, 33]. If a cell is migrating across a tight space that is narrower than the cell diameter, then its body adjusts its morphology accordingly, thus decreasing the resistance imposed by the confining tissue [33]. Regarding the cytoplasm and cell membrane, these structures adjust easily to migrate through gaps with a diameter smaller 1 µm [32]. However, when it comes to the nucleus, as it is the largest and stiffest organelle of eukaryotic cells, it is likely to challenge cell invasion or transmigration in cases where the size of the gap is smaller than the diameter of the cell nucleus [4, 32, 33].

Nuclear mechanics in confined migration

Nucleus composition and structure are key factors involved in nuclear mechanics during confined migration, as they modulate nuclear shape and stiffness [33]. As a consequence of significant deformation, the nucleus is likely to suffer conformational changes, possibly having repercussions in mechanotransduction and ultimately altered cell phenotypes [4]. Numerous studies have found that the ability of the nucleus to deform is indeed the major limiting factor in migration through confined spaces [32, 34–36]. There can be several factors regulating the obstacle effect that the nucleus exerts in migration through tight spaces, including alterations in nuclear deformability and the forces that the cytoskeleton applies to the nucleus via the cytoskeleton-nucleus linkers described in subsection 2.1.2 [32].

Two of the main aspects determining the ability of the nucleus to squeeze or deform are chromatin and the nuclear lamin network [32, 37, 38]. Chromatin is composed of DNA involved around histone octamers, and it exists in two configurations: open euchromatin, which allows DNA transcription, and compact heterochromatin, related to inactive genes [32]. Fu et al. (2012) hypothesized that the squeezing capacity of the cell nucleus to migrate through constrictions might be related to chromatin condensation status, given that MTA, a chromatin decondensation drug, reduced the efficiency of MDA-MB-231 cells migration under confinement [34]. Regarding nuclear lamins, they can be subdivided into two subcategories: A-type (A,C,C2) and B-type (B1-3) lamins [32]. Besides modulating nuclear shape and stiffness, lamins are involved in DNA repair, chromatin organization and transcriptional regulation [32]. Harada et al. (2014) and Davidson et al. (2014) found that the loss of Lamin A/C resulted in enhanced capacity for cell migration in confined environments, by increasing nuclear deformability [36, 39]. In addition to nuclear stiffness roughly increasing with Lamin A/C expression, it was found that lamin B1 may also contribute to nuclear rigidity [32]. Studies have hinted at a capacity for cells to modulate their stiffness during migration due to their ability to vary Lamin A/C expression levels and organization as a function of cytoskeletal tension and environment stiffness [32].

It is not completely clear whether cells mainly employ pull or push mechanisms in order to translocate the nucleus via the LINC complex for migration across narrow constrictions, since both types of mechanisms have been reported [32]. Similarly to what was described in subsection 2.1.2 for 2D migration, studies have suggested that actomyosin contractility may also be a mechanism to pull the nucleus onward during 3D cell migration [32]. Wolf et al. (2013) have shown that traction mediated by integrin at the leading edge and actomyosin contractility are necessary for nuclear transport across tight spaces in cells employing a mesenchymal lamellipodia-based migration mode [35]. In a different mode of 3D migration, namely lobopodial, Petrie et al. (2014) found that actomyosin bundles containing non-muscle myosin IIA (NMIIA) cooperate with vimentin filaments to pull the nucleus onward, through connection to nesprin-3α (present in the LINC complex) via plectin [40]. Additionally, nuclear migration across narrow spaces using pulling mechanisms might also be mediated by microtubule motors [32]. As for pushing mechanisms driving nucleus translocation through constrictions, Thomas et al. (2015) unraveled a new mechanism in breast cancer cells consisting in the recruitment of non-muscle myosin IIA (NMIIB) to the perinuclear cytoskeleton and rear of the cell to apply pushing forces to the nucleus, thus facilitating confined nuclear transmigration [41]. However, it is not clear yet whether if this NMIIB-dependent actomyosin contraction is a general process in nuclear translocation and whether nesprin-3α and vimentin filaments play a role in this process [32].

When a cell is migrating through a confined space, the fact that the nucleus occupies most of the space of a constriction forces the cytoplasm to compartmentalize at the front and back of the nucleus in order to transmigrate [32]. With this mechanism, intracellular pressure is generated by the nucleus, which then acts as a ”piston” [32]. Petrie at al. (2014) demonstrated that this mechanism is actually beneficial for cell transmigration across narrow spaces in lobopodial-based migration, since the pulling of the nucleus driven by actomyosin filaments places the cell front under compression, promoting the formation of novel protrusions at the leading edge [40].

As the nucleus carries the genetic information of the cell, it is important to assess whether confined migration can result in its deterioration. Some studies have reported nuclear envelope rupture and DNA damage during cell migration across very narrow spaces, which causes apoptosis when the DNA is not properly repaired [39, 42, 43]. However, further research is needed to assess if mechanical stress alone in confined migration is sufficient to give rise to DNA damage [32].

Cancer cell migration in three-dimensional environments

There are at least three ways for cancer cells to migrate *in vivo*: gradual ECM degradation, migration through pre-existing gaps or tracks resembling channels and following cancer cells (or cancer-associated cancer cells) that disclose passages for migration [8]. Cancer cells have a high capacity to migrate along tracks without the need for ECM degradation by employing an amoeboid migration mode, while also being able to employ, alternatively, a metalloproteinase (MMP)-dependent mesenchymal migration, doing so accordingly to the characteristics of the surrounding 3D environment and intrinsic cell properties [8, 44]. Moreover, cancer cells are highly responsive to physicochemical parameters such as hypoxia, a characteristic feature of solid tumors [44]. Hypoxia has been demonstrated to induce single-cell amoeboid migration in conjointly invading cancer cells, contributing to cancer dissemination [44]. Notably, unlike other cell types, cancer cells exhibit a high plasticity of migration mechanisms, being able to employ various migration modes depending on their surrounding 3D environment [8, 44]. This high plasticity may confer these cells with a unique ability to adapt to a wide range of environments, thus promoting disease progression [44].

It has been shown that lamins are misregulated in many types of cancer, contributing to the ability of these cells to deform while migrating across confined spaces [32]. For example, lower levels of Lamin A/C expression have been reported in several types of cancer, including breast cancer, being correlated with poorer disease outcome [32, 45]. Moreover, a study by Fu et al. (2012) found that metastatic breast cancer cells, namely MDA-MB-231 cells, depict higher nuclear deformation and are more capable of migrating across confining channels than MCF7 cells, which are poorly metastatic [34]. In another study, Mak et al. (2011) found that MDA-MB-231 cells showed a significantly higher ability to permeate into narrow channels when compared to non-metastatic cells (MFC-10A) [46]. Comparably, Chiotaki at al. (2014) showed that invasive breast cancer cells (Hs578T and MDA-MB-231) are able to deform their highly-elastic nuclei more extensively than normal and non-malignant controls [47]. These findings suggest that cancer cells are less stiff than non-malignant cells, which thereby enhances their metastatic ability.

Cancer progression can be further induced *in vivo* as a consequence of cancer cell migration through significantly narrow spaces. Nuclear envelope rupture and DNA damage that may occur as a consequence of cell passage across very tight spaces might be a source of genetic instability experienced by cancer cells, further enhancing its aberrant invasive characteristics [8].

2.2 Platforms to study confined cell migration

There is currently a wide variety of systems developed by researchers for the study of cell migration in 3D environments, which are often adapted to focus on certain cell characteristics or phenomena. In general terms, the current state-of-the-art engineered 3D microenvironments can be categorized into 1) hydrogels recreating the ECM, 2) microfabricated devices comprising microconstrictions and 3) 3D bioprinting [48]. These systems allow the study of different aspects of cell dynamics and structure, such as the ability of cells to migrate through very narrow spaces or to degrade fibers from ECM-like environments, and the changes in morphology exhibited by cells when placed under confinement [4].

It is important to note that, due to the common complexity of these systems in an attempt to more accurately recreate *in vivo* environments, it can be difficult to accurately perform certain measurements or retrieve specific types of data from the sample for the analysis of complex cell behavior [4]. Moreover, despite the usefulness and convenience of these systems, they do not fully contemplate the complexity of a tumor microenvironment, thus possibly limiting the clinical relevance of the studies [48]. To overcome this issue, *in vivo* models could be used instead, although they are significantly more costly and access to tumor invasion sites for imaging is limited [48]. A possible solution to avoid the mentioned limitations could be the use of decellularized matrices and *ex vivo* platforms comprising structures and cells that are naturally present in the tumor in order to best mimic its microenvironment [48]. However, these systems allow for little control over the degree of physical confinement, may not be appropriate for the performance of high-resolution imaging, and can exhibit high variability and heterogeneity [48]. Thus, when bearing in mind the discussed variables, the three engineered 3D microenvironment strategies mentioned above, namely 3D hydrogels, microfabricated devices and 3D bioprinting, seem to be appropriate choices for accurate study of cell migration, as they allow for precise control of certain variables of the environment, such as material properties, force, and geometry [48]. These three types of strategies will be explored in the subsections below.

2.2.1 Three-dimensional hydrogels

Hydrogels are insoluble cross-linked polymer meshes that can absorb high amounts of water which can be tuned to mimic desired properties of the ECM [48]. This adjustment can be performed by several means, including the choice of polymer types, their concentration as well as their cross-linking degree, together with certain molecules with bioactive properties [48]. Based on the primary constituents of the ECM, some of the most common types of polymers to use in the creation of ECM-like hydrogels are fibronectin, collagen, hyaluronic acid and fibrin [48]. By mechanically tuning these hydrogels, the effects of ligand density, substrate stiffness and pore size on cell migration can be studied [49]. This system has the advantage of allowing the formation of migration tracks similar to those found *in vivo* and, often unlike with microfabricated devices, with physiologically relevant stiffness [49].

Pore size in hydrogels can be varied by controlling the degree of cross-linking between polymers: the higher the degree of cross-linking, the smaller the pore size [49]. However, the pores created in these gels are often smaller than the ones existing *in vivo*, in addition to the fact that it is not possible to control the track length and width as it is with other systems, such as microfabricated devices [49]. Additionally, 3D hydrogels gels have viscoelastic properties and the degree of cross-linking, for example, is hardly perfectly homogeneous, being heterogeneous at the cell scale, which may affect quantification of certain cell dynamics, such as velocity of migration [4].

Examples of studies with 3D hydrogels include a study by Wolf et al. (2013) in which the authors used physiological collagen networks to investigate the substrate conditions that affected the migration of different cell types in 3D extracellular matrices, having analyzed cell deformation and migration speed with varying pore sizes [35]. Similarly, Tien et al. (2020) studied the effects of stiffness and pore size in the invasive capacity of MDA-MB-231 cells into collagen matrices, incorporated in a complex setting making use of microfluidics to recreate the initial stage of breast tumor progression [50]. In a comprehensive study of confined cell migration, Lautscham et al. (2015) studied the effects of cell stiffness, nuclear and cytoplasmic volume, adhesiveness and contractility in the migration of several different types of cancer cells in self-assembled collagen networks [51]. To analyze cell migration dynamics in the matrices, the authors performed a variety of calculations, including cytoplasmic volume, cell contractility and the invasion depth [51].

2.2.2 Microfabricated devices

Microfabricated devices for the study of confined cell migration typically make use of PDMS, given that this elastomer is optically transparent, thus allowing clear imaging of cells, biologically inert, and oxygen-permeable [49]. PDMS devices are often fabricated by producing a PDMS replica from a silicon wafer containing the wanted design, which can comprise structures as small as a few nanometers, although most designs are on the micrometer scale [49]. These systems may include straight PDMS channels for the cells to migrate through or may feature constrictions created by micropillars across which cells migrate. Due to their properties, these platforms allow for clear microscope time-lapse acquisitions and precise quantification of cell migration direction, velocity, and intracellular dynamics [48].

PDMS channels mimic different types of structures found *in vivo* through which cancer cells migrate, such as bone cavities, the lumen of blood or lymphatic vessels, or along collagen tracks opened by ”leader” cancer cells [49]. Microconstrictions created by PDMS pillars may mimic endothelial junctions through which cancer cells migrate for vessel extravasation or intravasation, for example.

In early studies of confined cell migration using microfabricated devices, Irimia and Toner (2009) designed a set of microfluidic devices with channels of varying cross section areas to study the dynamics of spontaneous confined migration of several cell types, including migration velocity [52]. In their designs, channel width varied from 6 to 100 µm and channel height was either 3 or 12 µm [52]. Another pioneer study making use of microfluidic devices to study confined cell migration was performed by Fu et al. (2012), in which the authors studied the transmigration of cancer cells across 4, 8 and 12 µm-wide PDMS channels [34]. Furthermore, Davidson et al. (2014) devised a microdevice containing constrictions of different widths, namely 2, 3 and 5 µm, created by round micropillars, and studied the velocity of cell migration across the constrictions as well as the ability for cell nuclei to deform with different Lamin A/C expression levels [36]. In the same study of confined cell migration performed Lautscham et al. (2015) mentioned in subsection 2.2.1, the authors also studied the effects of cell stiffness, nuclear and cytoplasmic volume, adhesiveness and contractility in the migration of several different types of cancer cells across PDMS microconstrictions of widths ranging from 1.7 to 11.2 µm, and a constricting height of 3.7 µm [51]. To quantify cell migration dynamics through the constrictions, the authors performed a variety of calculations, including the probability of cell positions and migration velocity at the entrance, middle, or exit of the constrictions, as well as the squeezing ratio of the nuclei and stalling ratio of the cells at the entrance of the channels [51]. More recently, Mirzaaghaian et al. (2020) studied the relationship between the mechanical properties of two cell types and entry time into microchannels under varying microenvironmental parameters, such as constriction size, cell size, and effective cell surface tension. To this end, the authors developed a model that would be able to predict entry time based on these parameters, with the applicability of later being used to distinguish different cell types.

PDMS constrictions can be coated with a range of proteins of the ECM, such as fibronectin, thus enhancing cell attachment and migration, as it better recreates cell microenvironment *in vivo*. For example, Irimia and Toner coated their microdevices for the study of confined cell migration with collagen type IV [52], whereas Krause et al. (2019) and Zanotelli et al. (2019) used collagen type I for cell migration microdevice coating [53, 54]. In another study, Lautscham et al. (2015) studied the influence of different adhesive ligands, namely collagen and fibronectin at different concentrations, in the migration behavior of MDA-MB-231 cells under confinement [51].

Chemical gradients may be imposed in order to study cell migration in a given direction according to certain chemical cues, thereby recreating chemotaxis phenomena that cancer cells experience while migrating for the formation of metastases [49]. These chemical gradients may be created by adding the desired chemoattractant to the opposite side of a device reservoir in relation to the location in which the cells are initially seeded [49]. For example, Davidson et al. (2014) developed a microfluidic device to study constricted cell migration towards a platelet-derived growth factor (PDGF) gradient [36]. In another study, Tong et al. (2012) performed a study using microfluidic devices with cell-constricting channels through which different cell types migrated according to a fetal bovine serum (FBS) chemotactic gradient, and studied how different strengths of FBS gradients impacted the migration of HOS cells (osteosarcoma cells) [55]. Moreover, research has shown that hepatocyte growth factor (HGF) induces breast cancer cell (MDA-MB-231) invasion [56], thus being an appropriate choice for the generation of a chemical gradient in migration devices for the recreation of *in vivo* breast cancer cell chemotaxis phenomena. More recently, Tweedy et al. (2020) used microfabricated mazes to find that cells can identify the shorter path to reach a chemoattractant stimuli [57]. Although in this study cells are not subjected to confinement, it can further illustrate the potential of using microfabrication and chemical gradients for the study of relevant, complex cellular phenomena occurring *in vivo*.

Other types of gradients, such as voltage and physical gradients, can be imposed in cell migration through microfabricated devices [49]. Electic fields can be found *in vivo* across epithelial and endothelial surfaces, being involved in wound healing and cancer metastasis [49, 58]. For example, Hang et al. (2013) studied the effects of physical confinement and application of an electric field in morphological and physical aspects of fibroblast migration [58]. Regarding physical gradients, these might be relevant to include in microdevices by designing more complex geometries, thereby allowing the study of cells' reaction when facing certain physical prompts in the tumor microenvironment [49]. As an example, Mak et al. (2014) created a device containing decision trees composed of microchannels to assess how mechanical factors such as directionality and dimensionality affected decision making for migrating cells [59].

Further performed studies making use of microfabricated devices for the study of confined cancer cell migration have included different features in order to study, for example, the effects of certain cells, such as endothelial cells, fibroblasts, and tumor-associated macrophages, as well as the influence of certain cytokines, microtracks in ECM-like structures and the presence of blood vessels, on cancer cell invasion [48]. Moreover, some studies have made use of platforms with heterogeneous stiffness to recreate heterogeneity in tumor ECM *in vivo* and adress its effects on cancer cell invasion [48].

Despite the undeniable potential of microfabricated devices for the study of complex microenvironments envolving cancer cell migration, there are a few limitations to these systems. These may include the impossibility for cells to degrade or remodel PDMS, as well as the rigidity of PDMS in comparison to the ECM, modifications in cell-cell signaling as a consequence of flow or adhesion of specific proteins to the device surface, and difficulty in assuring and maintaining stable chemotactic gradients [48].

In an attempt to better recreate the cancerous microenvironments in which cancer cells are integrated *in vivo* and overcome some of the limitations described above, microfabricated systems can, in part, make use of ECM proteins instead of PDMS [48]. For example, Choi et al. (2015) devised a complex biomimetic microsystem to allow the co-culture of breast cancer cells in the form of tumor spheroids with different cell types that are encountered in breast tumor microenvironment, such as mammary fibroblasts and mammary ductal epithelial cells, in a compartmentalized microfluidic device including an ECM membrane to mimic the microarchitecture of breast ductal carcinoma [60]. Moreover, recent advances for the study of metastasis formation include the use of microfluidic devices, namely organs-on-chips or even body-on-chips, which allow the modeling of multiple tissues or organs and their interactions, although more research is necessary to fully or at least more accurately recapitulate complex *in vivo* systems [48, 61].

2.2.3 Three-dimensional bioprinting

In order to create certain 3D microenvironments with precision, bioprinting can be used [48]. In 3D printing, materials of choice are deposited in a layer-by-layer manner to assemble complex 3D geometries from a previously-created digital design [62]. 3D bioprinting emerged as a variation of 3D printing in which biomaterials, ECM components, living cells and possibly biochemical factors are printed onto a pre-existing substrate or liquid reservoir [62]. This technique enables the assembly of complex 3D *in vitro* environments with tunable mechanical properties and varying cell types, and can be used to recreate certain tissues comprising hierarchical architecture and vasculature, for example [48]. Cells can be incorporated in this systems in two different ways, namely by cell encapsulation in hydrogels during the bioprinting process or cell seeding into previously fabricated scaffolds [48]. There are several 3D bioprinting modes available, each being best suited for different applications, and comprising, naturally, their own advantages and disadvantages [48].

Examples of studies of cancer cell migration in 3D environments using 3D bioprinting include a study performed by Zhao et al. (2014), in which the authors devised a system of 3D bioprinting of HeLa cells and a hydrogel mixture containing gelatin, alginate and fibrinogen to develop *in vitro* models for cervical tumor [63]. The expression of MMP, cell proliferation and chemoresistance were measured in the 3D bioprinted tumor constricts and comparisons were performed with 2D culture models [63]. In another study by Hang et al. (2014), the authors studied the influence of vessel geometry on the migration velocity and morphology of HeLa cells using micro-chips 3D-printed with hydrogel by fabricating microchannels with varying widths (25, 45 and 120 µm) [64].

3D bioprinting techniques have a significant amount of applications for the study of 3D cancer cell migration, being able to recreate complex physiological environments. However, there are a few limitations to this approach, which may include lower resolution in the generation of 3D microenvironments at the single-cell level, namely when compared to microfabrication techniques, and low printing velocities, thus possibly diminishing cell viability [48].

2.3 Correlative microscopy for the study of cell migration

Correlative microscopy arises when two or more microscopy techniques are combined in a correlative manner to analyze the same area in the sample, which can be performed simultaneously or sequentially, with the goal of retrieving the strengths of each technique, while downsizing their respective weaknesses [65]. This approach then allows the obtainment of more complex, thorough data from a given biological system in what pertains to its morphology, dynamics, chemical composition, and functionality, for example, than it would be possible using either one of the microscopy techniques involved [65]. There is a wide variety of microscopy approaches that can be correlatively combined in order to optimize the data that is retrieved from a given sample. Microscopy technique pairings may include correlation of light microscopy with super-resolution microscopy (SRM), correlation of SRM with electron microscopy, correlation of SRM with atomic force microscopy, and correlation of light microscopy with electron microscopy [65]. Additionally, variations of the same type of microscopy, such as phase contrast and fluorescence as sub-types of light microscopy, may be correlatively combined.

Cancer cell migration for the formation of metastasis is, naturally, highly reliant on cell dynamics. However, dynamics data alone from cell migration is not sufficient for a full understanding of the mechanisms that drive cancer cell migration in metastization, which is also valid for other cell types in the context of other physiological processes, such as immune cell migration to intervene in immune response. Hence, it is of utmost relevance to develop and employ correlative microscopy techniques that allow not only the study of cell migration dynamics but also the analysis of cellular structures with sufficient resolution. An example of a correlative microscopy approach employed to study cancer cell migration is a remarkable study by Karreman et al. (2016), in which the authors devised a multimodal correlative approach combining intravital microscopy to capture cancer cell dynamics and microscopy X-ray computed tomography together with 3D electron microscopy for cancer cell structure analysis in a mouse model [66]. The workflow devised by these authors lead to informative and unforeseen observations of single tumor cells exhibiting a metastatic behavior integrated in a realistic pathological setting [66]. These findings further emphasize the relevance of developing systems of this kind to better understand complex and clinically pertinent physiological processes such as metastasis formation. An example of a correlative microscopy approach employed to study cancer cell bio-physical properties *in vitro* is a study by Moura et al. (2020), in which the authors combined atomic force microscopy and fluorescence optical sectioning microscopy to study and differentiate single-cell bio-physical properties in heterogeneous human cell cultures [67]. The devised correlative microscopy approach allowed the simultaneous co-localized acquisition of fluorescence images together with nano-mechanical mapping [67]. This strategy and associated findings contribute to the notion that correlative microscopy is a powerful tool in the study of cancer cell migration.

Strengths of light microscopy include the ability to work with live samples and in a wide range of sample dimensions, as well as its ease of access. Additionally, since it can be used to image live cells, cell dynamics can be studied either with transmitted light or fluorescence imaging by the acquisition of time-lapses. In the case of fluorescence microscopy, great molecular specificity can be attained for more than one target by using, for example, synthetic dye immunolabeling or encoding of fluorescent proteins, allowing the imaging of specific, well-defined structures [65]. However, it can be complex to study both cell dynamics and structure simultaneously using the same light microscopy modality. Cell staining is often performed via immunolabeling in order to visualize certain cellular structures with detail, which requires cell fixation. This would then prevent the imaging of these cellular structures during cell dynamics, given that, once fixed, cells are no longer alive. An approach to overcome this limitation could be the generation of cell lines expressing certain fluorescent proteins localized in the structures of interest to analyze, which would then allow both cell dynamics and structure to be imaged at the same time. However, it might be inconvenient and costly to keep generating different cell lines to enable the study of various cellular structures at different times. An alternative for this approach would be the use of a system that would allow the correlation of live cell imaging for the study of cell dynamics with fixed cell fluorescence imaging for the study of cell structure. If performed sequentially, such combination would allow the observation of cellular structures that are involved or associated with certain cell dynamics, which would be particularly relevant in the context of the study of cancer cell migration. Notably, Almada et al. (2019) developed such system, called NanoJ-Fluidics [6]. In addition to a wide variety of potentialities that this system offers, it can serve as a powerful to perform precisely the correlative microscopy problem just described.

2.3.1 NanoJ-Fluidics - a system for automated multimodal microscopy

NanoJ-Fluidics, which was developed in a collaboration between the Ricardo Henriques and Christophe Leterrier laboratories, is an open-source, user-friendly system that allows automatic fluid exchange in microscopy experiments [6]. More specifically, it enables the performance of labeling and treatment protocols directly on the microscope stage in an automatic manner, which would otherwise have to be carried out on the bench, possibly interrupting microscope acquisitions [6]. Hence, by using this system, the same cells can be imaged in different conditions and with varying microscopy modalities, which emphasizes how powerful this framework is for the performance of studies with correlative microscopy.

This system makes use of LEGO®-based syringe pumps for fluid injection onto the sample and a peristaltic pump for liquid waste removal, with the software being open-source and either provided as an ImageJ/µManager plugin or as a stand-alone package if the user wishes to control the pumps independently [6]. For automatic control of the pumps, an Arduino® controller interface is used [6]. The fact that the syringe pumps are built with LEGO® makes NanoJ-Fluidics an affordable and modular framework, allowing the execution of protocols in a repeatable and robust manner [6]. Additionally, and very conveniently, this system is compatible with most microscope set-ups and experimental workflows, together with it not requiring the fabrication of microfluidic devices [6]. Furthermore, the authors of this framework have characterized the accuracy and precision of the volumes injected by the syringe pumps in several conditions, having found that the precision and accuracy were both below 5% of the defined injection volume, which emphasizes the reliability provided by the system for the execution of imaging protocols [6].

There can be several applications of this system in microscopy experiments. An example is event-driven fixation imaging, where an automatic staining protocol, including the fixation step, can be initiated once a certain morphological cue is observed in the sample [6]. This can allow the acquisition of a live-cell time-lapse and subsequent automatic execution of a staining protocol followed by fluorescence imaging of the sample, in order to compare between dynamic and structural information of the same cells during the event of interest [6]. This can also be performed without the need for user intervention between acquisitions, if the decision to activate a fluidics protocol is driven by appropriate software, which can be done by continuous analysis of the image by the software and triggering of protocol initiation once the desired morphological cue is detected [6]. Alternatively, the same experimental workflow can be carried out without the desire to identify a specific event during cell dynamics, in which case the live-cell time-lapse acquisition can have a defined duration, after which the automatic staining protocol can be initiated. Another example is live-to-fixed SRM, which is in everything similar to the examples given above, except super-resolution images are posteriorly generated from fluorescence images of the fixed sample [6]. These examples are all possible solutions to the problem posed above on dynamic-to-fixed correlative microscopy for cancer cell migration studies. Yet another example for the applicability of NanoJ-Fluidics is the ability to perform multimodal multilabel super-resolution imaging [6]. Specifically, the authors showed that multiplexed STORM (stochastic optical reconstruction microscopy) and DNA-PAINT (point accumulation in nanoscale topography) SRM could be easily performed using NanoJ-Fluidics, in which 5 different cell structures were fluorescently labeled and imaged for posterior super-resolution images generation using STORM [6]. This was due to the possibility that the system offers for sample washing in between acquisitions, thus expanding the possibilities for structure labeling and subsequent capturing during microscopy experiments [6].

2.3.2 Super-resolution imaging - SRRF

Although light microscopy is, as described above, a powerful tool for bioimaging, its resolution is limited to approximately 300 nm due to light diffraction [65]. Thus, if the goal is to analyze certain cell structures in high detail, fluorescence microscopy might not be sufficient. In order to overcome this limitation, light microscopy could be correlated with a high-resolution method, such as electron microscopy or atomic force microscopy [65]. However, the significant difference between the resolutions provided by light microscopy and these two modalities hinders the correlation of images obtained with both types of techniques [65]. To overcome this issue, SRM, which yields resolutions down to approximately 10-20 nm, could be used instead for correlation with light microscopy, since the resolution disparity is not as high as it is with high-resolution microscopy [65]. Super-resolution techniques make use of fluorescence microscopy, except very differently in relation to what is performed in light microscopy: the fluorescence signal is often generated, detected and especially processed in distinct manners [65].

There is currently a wide variety of available SRM approaches, each more appropriate for different contexts. In general terms, these include: super-resolution single point scanning (SR-SIM), subdivided into point scanning SIM and interference-based, stimulated emission depletion (STED), reversible saturable optical linear fluorescence transitions (RESOLFT), single molecule localization microscopy (SMLM), super-resolution optical fluctuation imaging (SOFI), SRRF, lattice light sheet (LLS), and expansion microscopy (ExM) [68]. If a SRM technique is intended to be used, the choice of modality can be made depending on whether live or fixed cells are to be imaged and whether an advanced or low cost SRM technique is desired [68].

SRRF, for example, is a low cost SRM modality developed by Ricardo Henriques and colleagues (2016) which allows to image both live and fixed cells [68, 69]. In this approach, a sequence of images acquired in a total internal reflection (TIRF) or widefield microscope is processed to produce a super-resolution reconstruction, without the need for specific detection and localization of fluorophores [69].

To perform SRRF imaging, only the software, which is integrated in ImageJ as a plugin, is needed, thus making this a low cost SRM and virtually enabling any laboratory to accomplish super-resolution imaging [69]. Additionally, it allows the fast processing of images, making it suitable for the generation of super-resolution images in time-lapse acquisitions with a temporal resolution of 1 second, and is capable of producing reconstructions of resolutions better than 150 nm even when the fluorescence signal emitted by the sample is low [69]. SRRF is then a highly versatile technique, allowing to obtain both fixed-cell and dynamic live-cell super-resolution images with the use of conventional fluorophores, thus making it compatible with a wide range of imaging modalities [69]. As opposed to SRRF, it is noted that SIM requires expensive optics, and SMLM is limited to phototoxic laser intensities for image generation, for example [69]. Additionally, the authors evidenced that SRRF outperforms other SRM methods capable of processing data sets of high density in terms of image reconstruction artifacts, given that it did not cause the disappearance of structures or the occurrence of ringing effects [69].

SRRF is a fast algorithm which performs radial and temporal analysis of fluorescence intensity fluctuations in a given image sequence at the sub-pixel level. By performing this analysis, SRRF is able to generate super-resolution images due to the fact that, roughly speaking, on one hand, signal originating from noise is uncorrelated in time, thus being approximately canceled out if a large stack of images acquired sequentially is analyzed, and, on another hand, signal originating from fluorophores is correlated in time. Notably, the SRRF algorithm is able to produce images with resolution approximate to 60 nm [69].

Given its accessibility and several other advantages, SRRF can then be contemplated in various correlative-microscopy frameworks for a more detailed study of cellular structures. In particular, it can be incorporated in experiments with NanoJ-Fluidics for the generation of super-resolution images from fixed-cell fluorescence images, in order to integrate a robust workflow for a thorough study of both dynamic and structural aspects of cancer cell migration.

Chapter 3

Materials and Methods

3.1 Cell culture

MDA-MB-231 cells (herein referred to as MDA cells), a gift from Gonçalo Bernardes Lab (iMM), were cultured in Dulbecco Modified Eagle Medium (DMEM) with sodium pyruvate (11995065, Thermo Fisher Scientific), 10% FBS (F0804-500ML, Merck) and penicillin-streptomycin (15140122, Thermo Fisher Scientific) at 120 units/ml. NIH 3T3 fibroblasts (CRL-1658, ATCC) were cultured in DMEM with no sodium pyruvate (41965039, Thermo Fisher Scientific), 10% bovine calf serum (35-053-CM, Corning), 10 mM HEPES (15630056, Thermo Fisher Scientific) and penicillin/streptomycin at 500 units/ml. Both cell lines were cultured at 37° C in 5% CO_2.

3.2 Production of MDA cell lines expressing NLS-GFP and LifeActin-mcherry

As the cell nucleus and actin filaments were structures of interest to observe in fluorescence microscopy experiments with the migration devices, MDA cells were infected with lentivirus expressing NLS-GFP and LifeActin-mcherry with puromycin resistance, produced in HEK293T cells (pLALI backbone). Cells were firstly infected with lentiviral particles expressing NLS-GFP or LifeActin-mcherry. After changing the medium of cells at approximately 80% confluency in a 6-well plate, 10 µl of viral suspension for NLS-GFP expression were added to each well for half of the plate, and 10 µl of viral suspension for LifeActin-mcherry were added to each of the remaining wells. For selection of transfected cells, puromycin was added at 2.5 mg/ml for four days. To generate a double line, NLS-GFP-expressing cells were infected with lentiviral particles containing a plasmid for LifeActin-mcherry expression, following the same procedure. To obtain a cell line expressing both fluorescence genes for future use in experiments, fluorescence-activated cell sorting (FACS) was used. Three cell lines were kept in culture: one expressing only NLS-GFP, another expressing only LifeActin-mcherry, and a double line expressing NLS-GFP and LifeActin-mcherry.

3.3 siRNA transfection in MDA cells

To investigate the role of Ctdnep1 and Eps8L2 in confined cell migration, we recurred to siRNA to perform the knockdown of these proteins in MDA cells. The siRNAs that were used for cell transfection were Eps8L2 siRNA (HSS185565, Thermo Fisher Scientific), Ctdnep1 siRNA, which was custom made by GeneCust (sequence 5'-3': CAGCAUUGUGAUCCUGGAUTT), and the Silencer™ Select Negative Control No. 1 siRNA (4390843, Thermo Fisher Scientific), all at 20 µM concentration.

Prior to cell transfection, the control, Eps8L2 and Ctdnep1 siRNA mixtures were prepared as described here. 5 µl of siRNA were added to a tube containing 250 µl of Opti-MEM™ (31985047, Thermo Fisher Scientific), and 5 µl of Lipofectamine™ RNAiMAX Transfection Reagent (13778150, Thermo Fisher Scientific) were added to another tube containing 250 µl of Opti-MEM™. The latter was added to the former, carefully mixed by pipetting up and down, and left for incubation at room temperature for 15 minutes. During the incubation period, cells at approximately 50% confluency in a 10 cm dish were washed with phosphate-buffered saline (PBS, 18912014, Thermo Fisher Scientific) and left with 1 ml of trypsin-EDTA (0.05%) (25300062, Thermo Fisher Scientific) at 37° C until adherent cells were dissociated from the dish (approximately 5 minutes). Cells were resuspended in 8 ml of fresh medium and added to 3 wells of a 6-well plate already containing medium, after which the mixtures containing the siRNAs were added to each well. For this transfection protocol, the volumes added to each well were always 1.5 ml of medium, 500 µl of cells and 510 µl of each siRNA together with Opti-MEM™ and Lipofectamine™ RNAiMAX Transfection Reagent. Medium was changed 24 hours after transfection.

3.4 Migration devices fabrication

To produce the PDMS migration devices, we used molds already available in the lab, which were fabricated according to the designs by Jan Lammerding Lab [70]. The molds were fabricated from SU-8 photoresist using standard lithography techniques, following the procedure described by the authors [70].

One migration device is suitable for two conditions, meaning that, for this work, two cell migration experiments each in a given siRNA transfection condition could be performed. The migration devices were designed to include the following features, for one condition (half of a device): 1) two cell inlets through which cell seeding can be performed; 2) an area with round micropillars that create constrictions of different dimensions through which the cells migrate; 3) two areas adjacent to the micropillar area either in which the cells are seeded or in which the cells gather after migration through the constrictions; 4) two reservoirs for medium and a channel that connects the two reservoirs. The micropillar area includes six sections that were designed to consist in, by order, three sections with constrictions 5 µm, 3 µm and 2 µm-wide, respectively, a section with no constrictions for reference during imaging, and two more sections with constrictions 3 µm and 2 µm-wide, respectively (see Figure 3.1A). The two medium reservoirs are used to create a chemotactic gradient to trigger cell migration in a given direction across the micropillars sections. The devices include features with different heights, namely the micropillar sections, which are 5 µm-tall, and the areas in which the cells are seeded and gather after migration through the micropillars, which are 250 µm-tall.

PDMS was prepared using the SYLGARD™ 184 Silicone Elastomer Kit (Dow) by mixing very well the two components of the kit, elastomer base and curing agent, in the 10:1 ratio. A volume of mixture was poured over the SU-8 mold for the devices in a plastic Petri dish to make devices approximately 4 mm-thick and then degassed in a desiccator until no air bubbles could be seen in the mixture. The dish containing the mixture was put in an oven at 70° C for 1 hour to cure the PDMS. The cured PDMS replica was then carefully peeled away from the mold by making cuts with a blade around the mold area and using a pipette tip to detach the cut PDMS block from the surroundings (see Figure 3.1B). The blade was used again to cut out individual devices by following the marked lines and the holes were punched. For this, a 5 mm biopsy punch was used to create the medium reservoirs and a 1.2 mm biopsy punch was used to create the cell inlets, by punching the PDMS perpendicularly and precisely in the marked areas (see Figure 3.1C). After making the cell inlets, a 1 mm biopsy punch was used to go through the small holes to make sure that there were no PDMS remains inside.

To assemble the final microfluidic devices the PDMS replicas were bonded to 24 x 60 mm microscope glass slides, before which both components were washed. For this, the glass slides were placed in a glass container with an aqueous solution of Alconox® Powdered Precision Cleaner (1104-1, Alconox) at 10 g/L to be completely covered. The container with the glass slides was placed in a deionized water ultrasonic bath at 70° C for 1 hour and 30 minutes. Both the PDMS devices and the glass slides were then thoroughly washed with ethanol 70% followed by deionized water and left in a laminar flow hood to dry. For the bonding, the glass slides and the devices with the microfluidic channels facing upwards were placed separately on a metal tray and then put into a UVO-Cleaner® (Jelight Company Inc.) to activate the PDMS for 5 minutes. After the UV cleaning cycle, the machine was left on for 4 minutes before opening the drawer to eliminate excessive ozone. The bonding was then quickly performed by placing the PDMS devices on the glass slides with the microfluidic channels facing downwards and applying slight pressure on the periphery of the device, using tweezers (see Figure 3.1D,E). Two devices were attached to each glass slide, meaning that, in one migration experiment, four siRNA transfection conditions could be imaged.

3.5 Preparation of devices and cell seeding

Two days after transfection with siRNA, either two or three glass slides with PDMS devices were prepared to increase the probability of having a viable pair of devices in the day of imaging. Each glass slide with two devices was placed in a 10 cm dish. The medium reservoirs of the devices were washed once with 100 µl of ethanol 70%, then washed three times with 100 µl of deionized water and finally washed with 100 µl of PBS once, and filled with 100 µl of PBS until use. To enhance cell attachment and migration, a mixture with a ratio of 1000 µl of PBS to 20 µl of human fibronectin (356008, Corning) at 1 mg/ml in PBS was prepared to fill in all reservoirs of the devices. 10 µl of this mixture were first pipetted into each cell inlet and 100 µl were added to each medium reservoir. To minimize evaporation of the mixture in the devices, a 3 cm dish with water was placed inside each 10 cm dish and the devices were

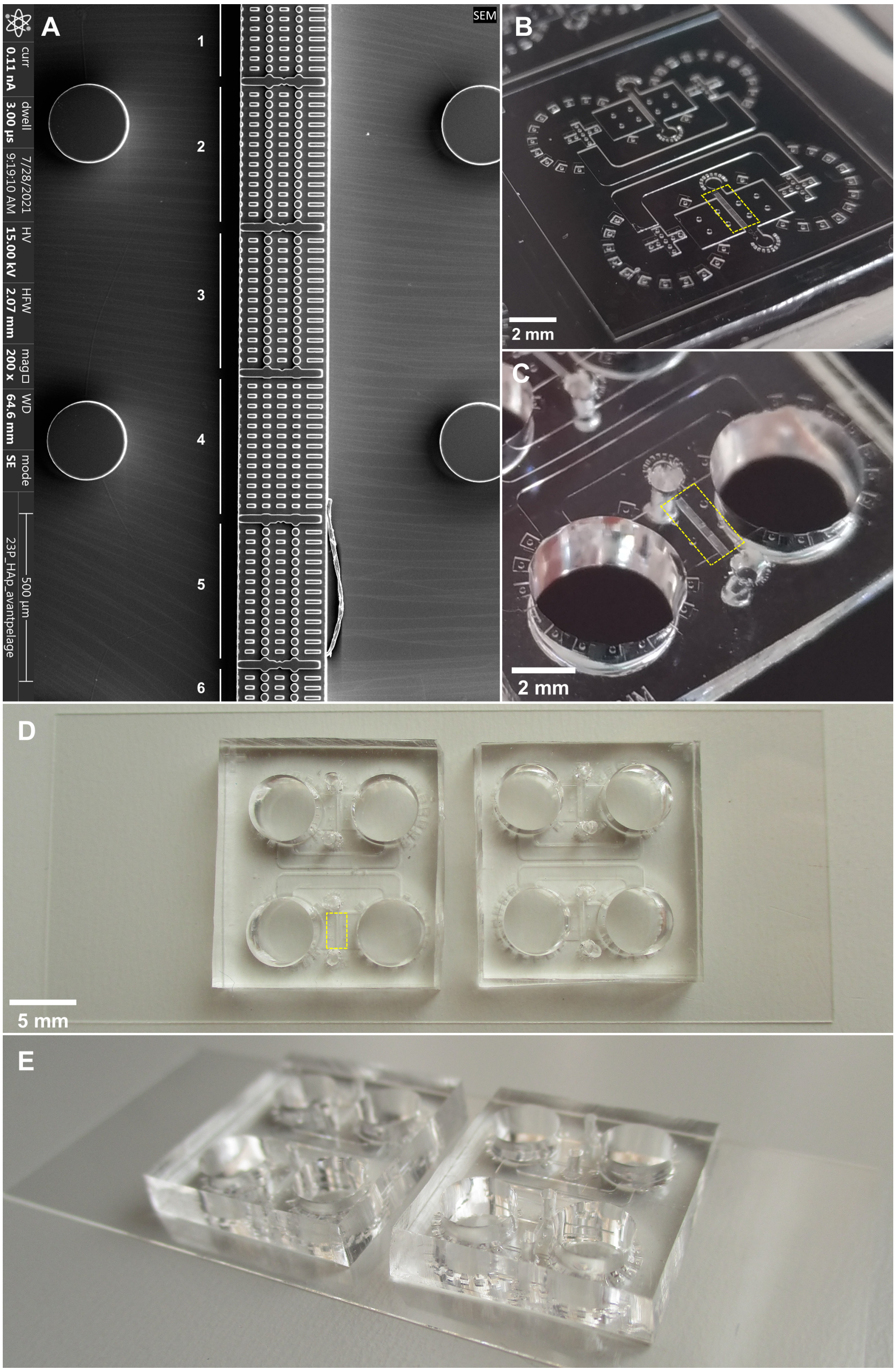
A
curr 0.11 nA
dwell 3.00 µs
7/28/2021 9:19:10 AM
HV 15.00 kV
HFW 2.07 mm
mag 200 x
WD 64.6 mm
mode SE
500 µm
23P_HAp_avantpelage
SEM
1
2
3
4
5
6
B
2 mm
C
2 mm
D
5 mm
E

Figure 3.1: **Images from the PDMS devices used to study cell migration under confinement.** (A) Scanning electron microscopy (SEM) image from the microstructural pattern of a PDMS device (selected region indicated by the yellow rectangles in (B), (C) and (D)). Six sections (labeled from 1 to 6) can be observed: 1) a section with a 5 µm distance between round micropillars (not shown in its entirety); 2) a section with a 3 µm distance between round micropillars; 3) a section with a 2 µm distance between round micropillars; 4) a section with no round micropillars; 5) another section with a 3 µm distance between round micropillars; 6) and another section with a 2 µm distance between round micropillars (not shown in its entirety). Image provided by the Institut Pierre-Gilles de Gennes (IPGG). (B) PDMS replica of the SU-8 device mold. (C) Close-up of a PDMS device. (D) and (E) Images of two PDMS devices attached to a glass slide (two different views).

incubated at 37° C for 1 hour. After 45 minutes of incubation, cells in the 6-well plate were washed with PBS and trypsinized with 200 µl of trypsin in each well. Cells were then resuspended in 1 ml of medium and centrifuged at 0.3 g for 5 minutes. During centrifugation, the devices were taken out of the incubator and the PBS and fibronectin mixture was aspirated. The medium reservoirs of the devices were washed with 100 µl of PBS and 100 µl of medium were added to each reservoir. After centrifugation, cells were resuspended in appropriate volume of medium according to their confluency in the 6-well plate. For a 50% confluent well, for example, 30 µl was an appropriate volume for cell resuspension. 5 µl of cells were carefully, although not too slowly, pipetted into the cell inlet closest to the edge of the device for each condition. The goal was to have cells already in the micropillar area right after cell seeding, in order to facilitate the observation of cells migrating through the micropillars later on. In some cases, it was necessary to add more cells to the same reservoir, as it was seen under the microscope that there were not enough cells in the desired area of the device. The side in which the cells were for each condition was checked under the microscope and 100 µl of medium were added to the medium reservoir in the opposite side of the cells to avoid their displacement. Due to the interconnectivity of the reservoirs, more medium was added to the same reservoir after the opposite reservoir started to load with medium, in order to fill up both reservoirs.

3.6 Preparation of devices for microscopy

One day after cell seeding, the devices with cells were analyzed under the microscope to choose the best one for imaging. The preparation of the devices for imaging was done right before taking the sample to the microscope. Two tubes were prepared, one with 1 ml of medium and another with 500 µl of medium and 50 µl of hepatocyte growth factor (HGF) human recombinant (100-39B, tebu-bio). The medium in the device reservoirs was aspirated slowly with a pipette, and 100 µl of PBS were slowly added to the reservoirs and then slowly aspirated. Holding two pipettes at the same time, the mixture with HGF was added to the medium reservoir in the opposite side of the cells and the medium was added to the reservoir in the same side of the cells, at the same time, to establish a chemotactic gradient for the triggering of cell migration across the micropillars. The reservoirs were filled to the top, although not excessively to avoid the formation of a bulge above the device surface. Two glass cover slips (22 x 22 mm) were then used to cover the two devices to minimize medium evaporation during the experiment.

3.7 Imaging of cells in migration devices

For cell migration experiments with PDMS devices, a widefield fluorescence microscope was used – either ZEISS Cell Observer SD or ZEISS Cell Observer, the former being equipped with a sCMOS camera (ORCA-Flash4.0 V2, Hamamatsu) and the latter with a CCD camera (Axiocam 506 mono, ZEISS), and both being equipped with a motorized stage (ZEISS). The software used to carry out the experiments was ZEN 2.6 (blue edition) for experiments with ZEISS Cell Observer SD and ZEN 3.0 (blue edition) for experiments with ZEISS Cell Observer. The glass slide with the devices was placed in the microscope stage inside a temperature-controlled incubator pre-heated at 37° C and with 5% CO_2 supply. Positions for image acquisition were chosen, namely the micropillar sections in both devices that were in a good state and with a considerable number of cells. Because thermal drift occurs in the devices when the temperature of the whole system is not stabilized, thus altering the desired focal plane of the cells, the system was left to stabilize after placing the sample in the microscope until no changes in the selected Z plane were observed, after which the image acquisition was initiated. Widefield images were acquired with a 20x objective in the selected positions every 10 minutes for an overnight period between 12 and 18 hours total. A Z-stack of either 3 or 5 slices (centered in the focal plane) within a range of 4.24 µm was acquired for every position, in order to compensate for possible changes in the focal plane due to thermal drift during image acquisition. Brightfield images, as well as red and green fluorescence images using LED lights of 561 nm and 488 nm, respectively, were acquired.

3.8 Analysis of images from cell migration in PDMS devices

Images from all completed sequences using migration devices were analyzed and the migration of selected cells was quantified. Despite the large amount of data resulting from experiments, the cells that were effectively quantified were significantly less than the cells that were imaged due to the application of specific criteria for quantification of nuclear transmigration, in order to avoid the analysis of unreliable results. We only analyzed cells that appeared healthy, did not divide or result from cell division at a critical time point for migration through the constrictions, with no adjoining dead or live cells that could affect the migration dynamics, and passing through undamaged micropillars.

Prior to cell migration quantification, image registration and pre-processing were performed in FIJI (ImageJ). For a given XY position, and after the best slice from the Z-stack was selected, image registration was performed using the MultiStackReg plugin, in order to align all frames from the time-lapse that were slightly misaligned due to imperfect positioning of the microscope stage between acquisitions. This procedure was only performed in the brightfield images, as these show static regions with high contrast, namely the device microstructure, that are not seen in the fluorescence images. The transformation matrix resulting from image alignment was then applied to the fluorescence images and the two channels were merged, in order to obtain the brightfield and fluorescence images overlapped. After image registration, the images were slightly rotated so that the vertical lines of the device microstructure were perfectly aligned with a reference vertical line.

For quantification of cell migration through the constrictions, a rectangle with approximately 10 µm of width was drawn in FIJI in the center of the micropillars through which the cell passed. The reason for not drawing a rectangle with exactly 10 µm of width was due to the impossibility to achieve such precise value because of pixel size. For images acquired in Zeiss Cell Observer SD rectangles 9.45 µm-wide were drawn and for images acquired in Zeiss Cell Observer rectangles 9.46 µm-wide were drawn, again due to slight differences in pixel size. After having the rectangle drawn, four key time points in the migration of the cell through the micropillars were considered: the time point at which the cell nucleus first reaches the left side of the rectangle ($t1$), which is considered to be 0 for simplification, the time point at which the nucleus first reaches the right side of the rectangle ($t2$), the time point at which the nucleus first passes through the left side of the rectangle ($t3$), and the time point at which the nucleus first passes through the right side of the rectangle ($t4$) (see Figure 3.2 for an example). The time that passed between each of these time points was then calculated for each cell, namely $t2 - t1$, denoted as enter period, $t3 - t2$, denoted as cross period, $t4 - t3$, denoted as exit period, and $t4 - t1$, denoted as transit period. Different plots of these periods were then produced in GraphPad Prism 8 for comparison between siRNA transfection conditions and constriction sizes. Additionally, the width of the constriction through which each cell migrated was measured in FIJI and a plot was produced in GraphPad Prism 8 to represent the real distances measured between micropillars for each constriction size category (2 µm, 3 µm and 5 µm).

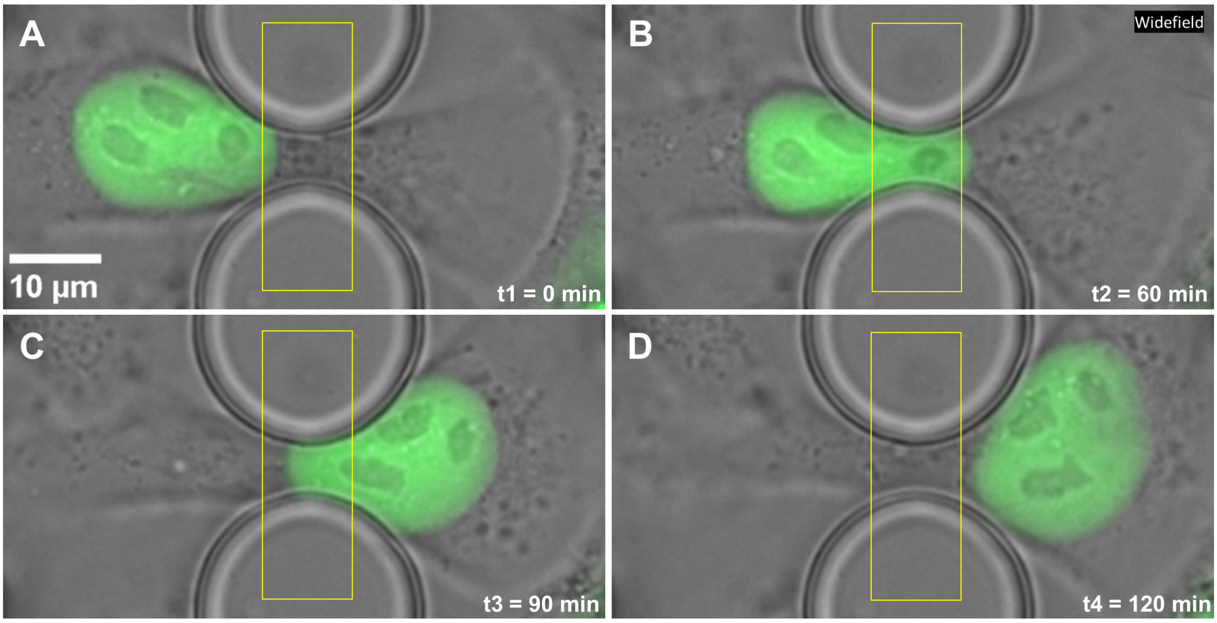

Figure 3.2: Selected frames from a widefield microscopy (brightfield and fluorescence images overlapped) time-lapse recording of a cell migrating through a microconstriction, in which the cell nucleus is marked with NLS-GFP. (A) Time point at which the nucleus first reaches the left side of the yellow rectangle ($t1$). (B) Time point at which the nucleus first reaches the right side of the yellow rectangle ($t2$). (C) Time point at which the nucleus first passes through the left side of the yellow rectangle ($t3$). (D) Time point at which the nucleus first passes through the right side of the yellow rectangle ($t4$). Time resolution: 10 minutes.

3.8.1 Statistical analysis

Groups for which there was enough migration quantification data for the use of meaningful statistical tests were tested for significant difference among means using an ordinary one-way ANOVA test. Tukey's multiple comparisons test was also employed to assess which were the groups whose means were significantly different among themselves. A *p*-value of less than 0.05 was considered significant. Statistical analysis was performed with GraphPad Prism 8.

3.9 Assembly of pumps for correlative microscopy with NanoJ-Fluidics

The NanoJ-Fluidics system makes use of LEGO®-based syringe pumps to automate fluid exchange procedures in microscopy. The pumps are controlled by an Arduino®, an open-source electronic prototyping platform, which is expanded with motor shields for an easy control of the pump motors. The pumps include syringes to handle the fluids, which are coupled with tubing via syringe needles to deliver the fluids to the sample. A peristaltic pump is used to remove the liquid waste from the sample chamber. The software that controls the system is provided as an ImageJ/µManager plugin or as a stand-alone package for independent fluidics control. The various components of NanoJ-Fluidics were assembled and installed according to the available wiki made by the authors [71], unless stated otherwise.

Eight multiplexed LEGO® pumps were first assembled. Pictures of an array of four LEGO® pumps can be observed in Figure 3.3A,B. The LEGO® Digital Designer software was used for guidance, as it allowed a clear 3D visualization of the assembled pumps from the file made available in the wiki [72]. All LEGO® pieces that were used to build eight multiplexed pumps can be found in Figures A.1 to A.5 in the Appendix. A 3D-printed version of the pumps was later assembled to use for the microscopy experiments as it would confer increased stability to the construct when compared to the original LEGO® pumps. The 3D-printed structures used to assemble the pumps in the present work were printed with polylactic acid (PLA) and kindly provided by Ricardo Henriques (Instituto Gulbenkian de Ciência, IGC), from the designs of Matthew Meyer (The Ohio State University, OSU), which can be found in the wiki. Specifically, the 3D-printed pump designs that were used in this work were the syringe pump unit main structure [73] and U-shaped pieces of two sizes to fit the syringes in [74, 75]. To assemble the pumps using the 3D-printed structures, the pump unit main structures were first tailored for the LEGO® pieces to properly fit in, as 3D printing often leaves filament residues apart from the desired structure. For this, a drill was used to enlarge the holes where the axle for the motor goes into, which were not perfectly circular after printing, until the motor could rotate the axle smoothly. Filament remains on the part of the structure where the motor is placed were also scraped off, so that the LEGO® piece could fit in properly. The LEGO® pieces that were necessary to complete the construction of the pumps, such as gears, axels, linear actuators and motors, as well as the U-shaped 3D-printed pieces to fit the syringes in, were then assembled onto the 3D-printed structure in a similar way as performed for the pumps fully made of LEGO®. Pictures of a pump built with 3D-printed structures can be observed in Figure 3.3C,D. The LEGO® parts that were used to build this version of the pumps can be found in Figures A.4 and A.5 in the Appendix, highlighted in blue. However, only four pumps making use of 3D-printed constructs were built, meaning that, from the parts highlighted in blue in the list, only half of the quantity of pieces was used for each part type. One fully built pump making use of 3D-printed structures was gifted by Pedro Pereira (Instituto de Tecnologia Química e Biológica, ITQB). A custom-made stand for the pumps and electronics hardware was made using regular LEGO® pieces and DUPLO® pieces.

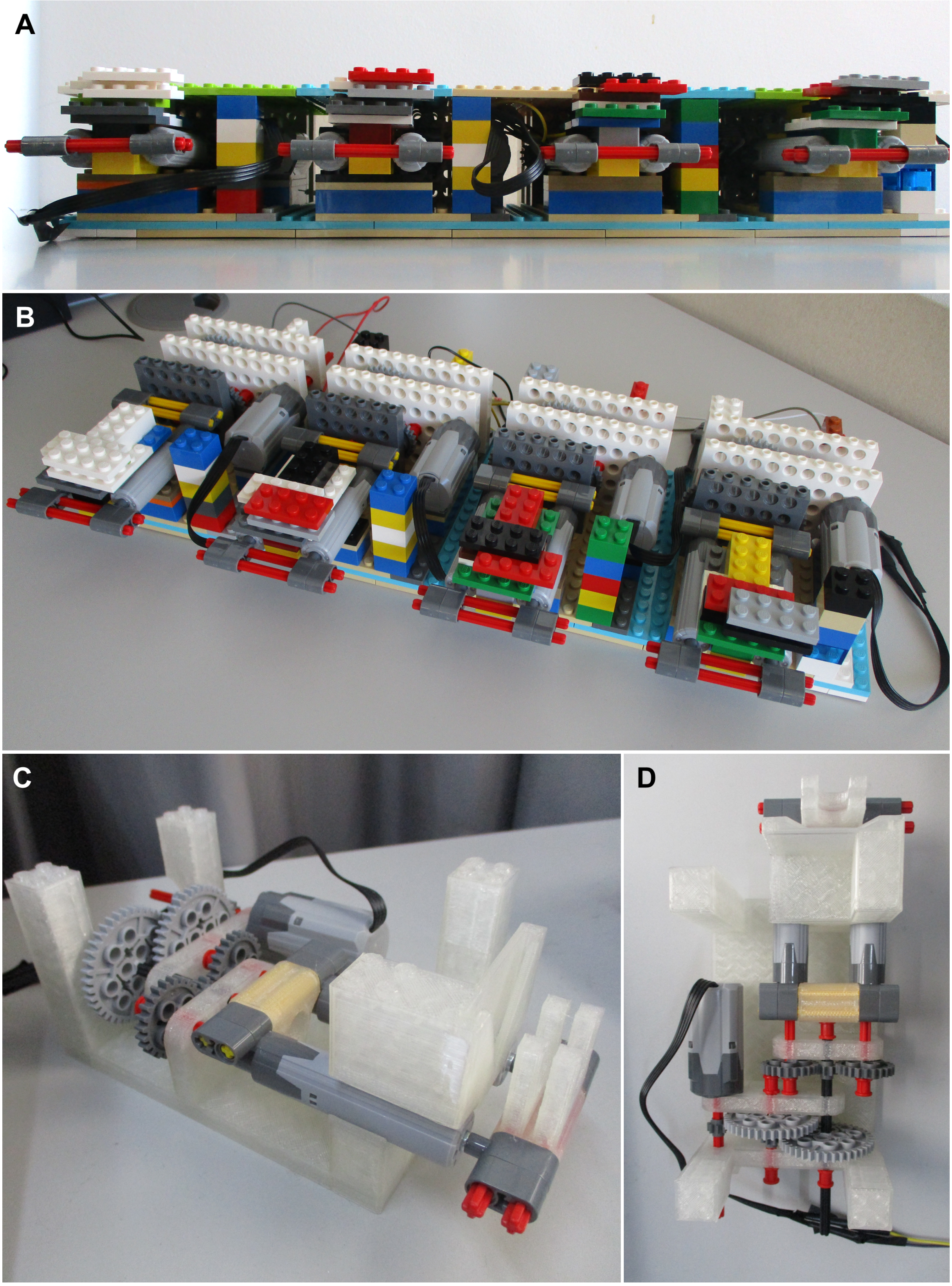

Figure 3.3: **Two versions of LEGO® pumps for NanoJ-Fluidics.** (A) and (B) Array of four LEGO® pumps with (A) and without (B) top cover. (C) and (D) Pump built with 3D-printed structures and LEGO® parts (two different views).

3.10 Pump control electronics hardware

For this work, the Keyestudio Uno R3 development board (KS0001, Keyestudio), fully compatible with Arduino® Uno Rev3, and the Adafruit motor-stepper-servo shield for Arduino® v2 kit (1438, Adafruit) were used. As one motor shield can control up to four DC motors and the goal was to have between 5 and 8 pumps working, two motor shields were installed, soldered and stacked on top of the Arduino®-compatible board. To allow shield stacking, shield stacking headers for Arduino® R3 (85, Adafruit) were soldered onto the motor shields. After modification of the LEGO® motors cables, the pumps were connected to the motor shields using female-male jumper wires (096-4681, Mauser). A 12 V peristaltic pump (1150, Adafruit) was connected to one of the motor shields, and the Arduino®-compatible board was connected to the computer using a USB 2.0 A-B cable.

3.11 Pump control firmware and software

After the shields were soldered and stacked on the Arduino®-compatible board, the firmware was installed. In short, the Arduino® IDE software and the Adafruit Motor Shield V2 Library were installed, followed by the download of the firmware file available in the wiki [76], and the Arduino® program was adapted to include the correct number of motor shields that were installed.

The pumps were controlled using the NanoJ-Fluidics graphical user interface (GUI). For the experiments developed in this work, the stand-alone version of the software was chosen, which was installed using the GUI file available in the wiki [77]. After having all the pumps connected to the motor shields and the Arduino®-compatible board with the firmware installed connected to the computer, the software was connected to the pumps in the GUI after first selecting “NanoJ Lego Control Hub” in the pump type and the USB port where the pumps were connected in the serial port.

3.12 NanoJ-Fluidics labware

Syringes, needles and tubing of two different types were used for liquids to be used in small volumes and liquids to be used in large volumes, respectively, in the experiments under the microscope. For liquids to be injected in small volumes, two-part 2 ml syringes (4020.000V0, HSW HENKE-JECT) were used. For liquids to be pumped in larger volumes, three-part Luer-lock 20 ml syringes (CH03020LL, CHIRANA) were used. Two types of TYGON® tubing with different internal diameters were used for the two different syringe sizes and liquid removal: TYGON® ND 100-80 tubing with internal diameter of 0.51 mm and external diameter of 1.52 mm (AAD04103, Saint-Gobain) for the small volume syringes, and TYGON® LMT 55 tubing with internal diameter of 0.76 mm and external diameter of 2.46 mm (070534-08L-ND, Saint-Gobain) for the large volume syringes and liquid waste removal. The needles that were used for the small internal diameter tubing and large internal diameter tubing were, respectively, 25G x 25 mm and 21G x 25 mm hypodermic needles (112510 and 112110, SOL-M).

To hook the tubing onto the sample during an experiment, holes were poked on the lid of a cell culture dish using a heated syringe needle. The culture dishes that were used for the experiments performed under the microscope were 35-mm glass-bottomed dishes (81158, ibidi), which feature a lid that locks onto the dish, allowing for more stability to hold the tubes in place during the experiment. To collect the waste, the large internal diameter tubing was connected to the peristaltic pump and the outlet tubing was taped to the inside of a glass container.

After every experiment, the labware was properly washed with deionized water for reutilization in future experiments. The tubing dedicated to the antibodies, as well as the tubing connected to the peristaltic pump, were also washed with an aqueous solution of NaCl (S9888-1KG, Merck) at 500 mM to effectively remove antibody remains. Each set of labware (syringe, needle and tubing) was always used for the same liquid in the same pump, for which all this material was numbered according to each different pump.

3.13 Pump usage

The pumps were set and maneuvered with a few modifications since the wiki is specific for the pumps fully made of LEGO® and the pumps used in this work made use of 3D-printed constructs. For example, to load a syringe onto the pumps, the syringe was simply fitted in the two dedicated slots in the pump. For 20 ml syringes, it was necessary to use rubber bands to secure the syringe in the U-shaped piece. Before using the pumps at any time, the linear actuators were manually extended to a length that matched that of the plunger of the syringes already containing the desired volume of liquid. Additionally, after fitting the syringe in the pump, the linear actuators were slightly retracted manually to ensure that once the pump started functioning, liquid would be pumped out of the syringe shortly after.

3.14 Pump calibration

For the pumps to inject the correct volume, they had to be calibrated. Calibration was performed with the appropriate components (syringe, needle and tubing) that were planned to be used in the experiments under the microscope. Briefly, an analytical balance was used to measure the mass of water that was injected by each pump for a pumping time of 10 seconds, which was later converted to volume by using ρ = 1 g cm^{-3} as the density of water. The calibration procedure was performed with water as all liquids to be used in the experiments had a density comparable to this value. For each pump, 10 measurements on the same conditions were performed, and the weighed volume was averaged for each pump. To calculate the maximum flow rate of each pump, the average volume pumped in 10 seconds was divided by the pumping time, and the resulting value was then multiplied by 0.25 to obtain the minimum flow rate. Calculations were performed in Microsoft Excel. The values for the maximum and minimum flow rates were input in the software for each pump, together with the internal diameter of each syringe type (see Figure 3.4). The software then extrapolated the correct flow rate at different syringe diameters for each pump, in order to inject the correct volumes. To ensure that the calibration was successful, tests with water were performed to assess if the volume that was injected by the pump

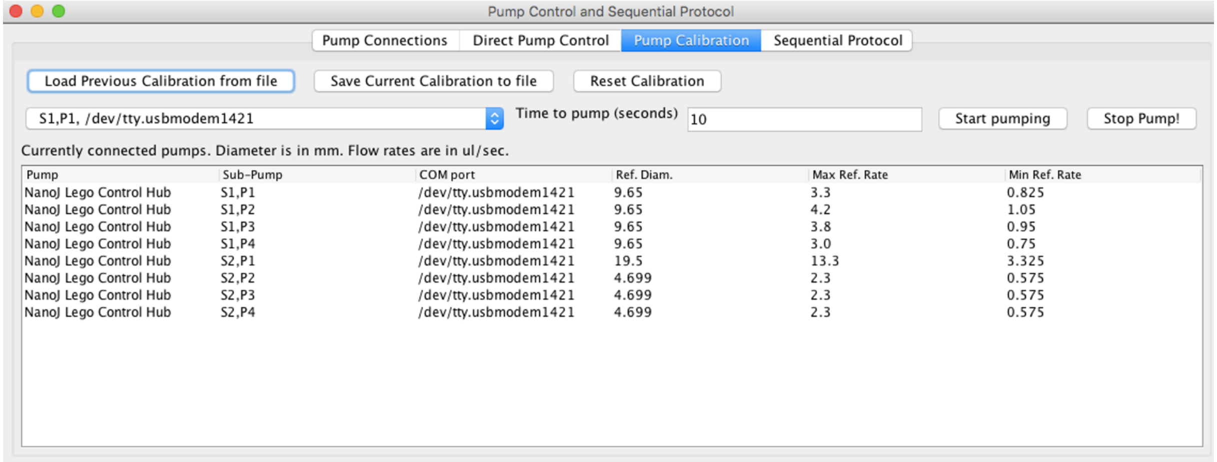

S1,P1, /dev/tty.usbmodem1421

Time to pump (seconds) 10

Currently connected pumps. Diameter is in mm. Flow rates are in ul/sec.

Pump	Sub-Pump	COM port	Ref. Diam.	Max Ref. Rate	Min Ref. Rate
NanoJ Lego Control Hub	S1,P1	/dev/tty.usbmodem1421	9.65	3.3	0.825
NanoJ Lego Control Hub	S1,P2	/dev/tty.usbmodem1421	9.65	4.2	1.05
NanoJ Lego Control Hub	S1,P3	/dev/tty.usbmodem1421	9.65	3.8	0.95
NanoJ Lego Control Hub	S1,P4	/dev/tty.usbmodem1421	9.65	3.0	0.75
NanoJ Lego Control Hub	S2,P1	/dev/tty.usbmodem1421	19.5	13.3	3.325
NanoJ Lego Control Hub	S2,P2	/dev/tty.usbmodem1421	4.699	2.3	0.575
NanoJ Lego Control Hub	S2,P3	/dev/tty.usbmodem1421	4.699	2.3	0.575
NanoJ Lego Control Hub	S2,P4	/dev/tty.usbmodem1421	4.699	2.3	0.575

Figure 3.4: NanoJ-Fluidics GUI exhibiting the values for the maximum and minimum flow rates that were introduced for each pump after the pump calibration calculations, together with the internal diameter of each syringe type. The values for the last three pumps remained unaltered, as these pumps were not used in the experiments.

corresponded to the volume defined in the GUI.

3.15 Live imaging of NIH 3T3 fibroblasts

The microscope used for live and fixed imaging of NIH 3T3 fibroblasts for correlative microscopy was Nikon Eclipse Ti, equipped with a CCD camera (Andor Neo 5.5 sCMOS, Oxford Instruments) and a motorized stage (Nikon). The software used to carry out the experiments was NIS-Elements AR 5.11.01. A 35-mm glass-bottomed dish containing cells at approximately 20% confluency was placed under the microscope in a small stage temperature-controlled incubator pre-heated at 37° C and with 5% CO_2 supply. The sample was covered with the lid comprising the holes for the tubing and the tubing was connected to the sample, making sure that the dish was stable in the incubator to avoid its misplacement, in order not to compromise the final goal of imaging the same cells in live and fixed-cell imaging. Only the tube for liquid waste aspiration was left touching the bottom of the dish. Eight positions containing cells that seemed interesting to image were selected for the time-lapse recording and later fixed-cell fluorescence imaging. The live imaging sequence consisted in the acquisition of widefield phase contrast images with a 60x objective in oil immersion in the selected positions every 60 seconds for a total period of 30 minutes. A Z-stack of 9 slices (centered in the focal plane) with a 0.5 µm step was acquired for every position, in order to capture several cellular structures that could be of interest to analyze. The focal plane was chosen in a way to capture the cell protrusions with detail. The Perfect Focus System was used for hardware focus control to ensure that the focal plane of the images would remain unaltered throughout the time-lapse acquisition.

Images from live-cell imaging of NIH 3T3 fibroblasts were selected and registered in FIJI. After choosing XY positions containing cells of interest for further analysis, we selected the slice of each Z-stack that better depicted cell protrusions in detail. Image registration was performed using the MultiStack-

Reg plugin for alignment of the time-lapse frames. Lastly, we created, for each chosen XY position, a montage exhibiting a selection of time-lapse frames equally spaced in time.

3.16 Staining protocol used for experiments with NanoJ-Fluidics

In this work, NIH 3T3 fibroblasts were stained for vinculin, phalloidin and DAPI. Before performing the staining protocol under the microscope using NanoJ-Fluidics, several staining procedures were executed on the bench, in order to adjust the protocol for optimal staining of these cells. The final cell staining procedure that was used in the experiments with NanoJ-Fluidics is described here. After medium aspiration, cells in 35-mm glass-bottomed dishes at approximately 20% confluency were fixed with 2 ml of 4% paraformaldehyde (PFA) in PBS, prepared from a 16% PFA aqueous solution (E15711, Science Services), which was left in the dish for 10 minutes. Cells were washed five times with 1 ml of PBS for 2 minutes and then permeabilized with 1 ml of Triton™ X-100 (X100-1L, Merck) diluted at 0.5% in PBS for 5 minutes, followed by another three 1 ml PBS washes of 5 minutes each. A volume of 500 µl of mouse monoclonal anti-vinculin antibody (V9264-200UL, Merck) diluted at 1:200 in 10% goat serum (G9023-10ML, Merck) in PBS was added to the cells and left in the dish for 30 minutes, after which cells were washed three times with 1 ml of PBS for 5 minutes. A volume of 500 µl of DAPI (32670-5MG-F, Merck) and Alexa Fluor® 488 Phalloidin (A12379, Thermo Fisher Scientific) diluted at 1:100 and Alexa Fluor® 555 goat anti-mouse IgG (H+L) highly cross-adsorbed secondary antibody (A-21424, Thermo Fisher Scientific) diluted at 1:600 in 10% goat serum in PBS was added to the cells and left in the dish for 30 minutes. Cells were washed three times with 1 ml of PBS for 5 minutes and left covered in 1 ml of PBS.

For the experiments performed with NanoJ-Fluidics, four syringe pumps plus the peristaltic pump were used. Although a pump for the fixative solution was initially assembled to use in the experiments under the microscope, the fixative was injected manually and not by a pump to ensure that the staining would not be compromised in case the pump containing the fixative would fail to pump the liquid right after the time lapse acquisition of the cells ended. The fixative, the Triton™ X-100 solution in PBS, the primary antibody and the secondary antibody together with DAPI and phalloidin volumes were put in four 2 ml syringes, respectively, the last three having been incorporated in pumps. The fourth syringe pump was for PBS, which was put in a 20 ml syringe but filled only at half capacity, as the full length of the linear actuators of the pumps was smaller than the length of a full 20 ml syringe. In this case, a PBS refill was done midway the experiment. For the liquids contained in 2 ml syringes, 0.5 ml of air was put in each syringe together with the liquid to ensure that all liquid was pumped to the sample instead of being partially left in the tubing, which was particularly relevant for the antibodies so not to waste any. In these cases, to guarantee that liquid alone was pumped first and not mixed with air, the pumps were tilted by 15-20° by placing an object underneath. Pictures of the NanoJ-Fluidics set-up that was used in correlative microscopy experiments can be found in Figure 3.5.

A sequential protocol was created in the GUI for a sequence of steps to be performed by the pumps, in order to allow an automatic cell staining procedure. A sequential protocol with the system was first

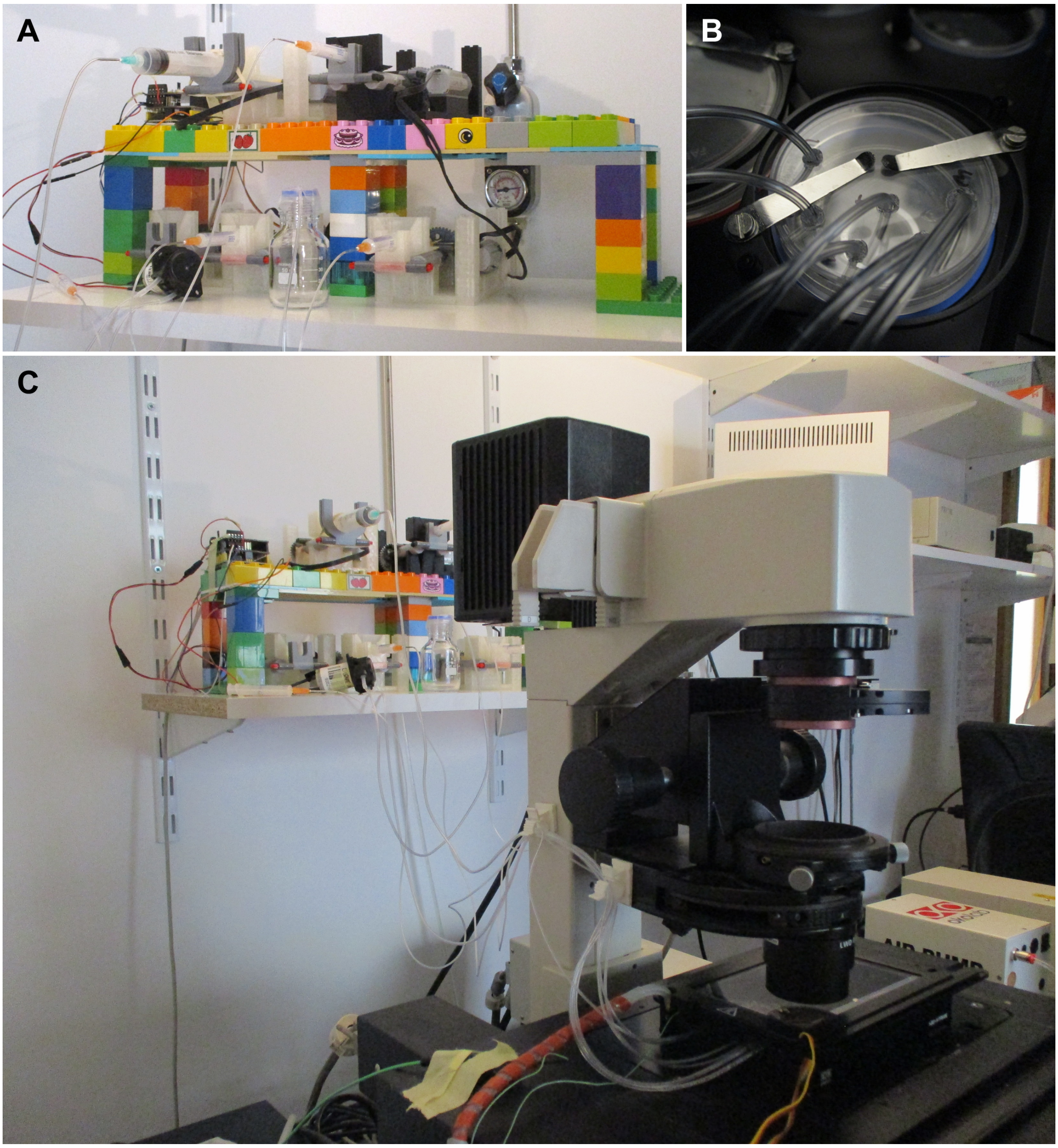

Figure 3.5: **NanoJ-Fluidics set-up used for correlative microscopy experiments.** (A) Pump set-up that was used for cell staining procedures, which includes the custom-made pump stand, the syringe pumps and peristaltic pump with respective labware, the electronics hardware, and a glass container for liquid waste. (B) 35-mm glass-bottomed sample dish covered with a pierced lid holding the tubing, placed in the microscope incubator. (C) All components of the setting used for correlative microscopy (excluding the computer), including the NanoJ-Fluidics pump set-up with respective tubing, which is by turn connected to the sample inside the temperature-controlled incubator of the Nikon Eclipse Ti microscope.

tried using only water in order to make protocol optimization and troubleshooting before executing the staining experiment. All steps described above were included in the protocol created in the GUI except for the fixation step, as the fixative was injected manually. A screenshot of the sequential protocol defined in the GUI is depicted in Figure 3.6. The volumes to be injected by each pump that were inserted in the GUI did not correspond exactly to the volume of liquid to send to the sample for the 2 ml syringes due to extra air having been put in the syringe, as explained above. For the primary antibody and secondary antibody together with DAPI and phalloidin, a volume of 0.6 ml was found to be optimal to be introduced in the GUI being, on one hand, large enough for all liquid be injected to the sample and, on another hand, small enough for the linear actuators not to get fully retracted prematurely since the system is not able to order the pumps to stop working once the linear actuators get fully retracted. For the Triton™ X-100 solution in PBS, a volume of 1.15 ml was found to be optimal to be introduced in the GUI, for the same reasons. A pumping time of 12 seconds for the peristaltic pump was found to be optimal being, on one hand, large enough for all liquid in the dish to be aspirated and, on another hand, small enough for the sample not to get completely dry. Due to the toxicity of PFA, the liquid waste container, which was sealed with aluminum foil or Parafilm M®, was replaced after the first PBS washes of the protocol in order to properly dispose of the fixative solution as soon as possible.

In short, right after the time-lapse acquisition of cells ended, the medium was aspirated using the peristaltic pump through the GUI, and the fixative was manually injected right after. 10 minutes after injecting the fixative, the sequential protocol defined in the GUI was started. The goal of proceeding in this manner was to allow the performance of correlative microscopy, meaning that the last frame of the time-lapse of a given cell could be accurately correlated with an image of several stained structures of the same cell.

3.17 Imaging of fixed cells

Fixed-cell imaging consisted in the acquisition of widefield phase contrast and fluorescence images with a 60x objective in oil immersion in the selected positions. A Z-stack of 11 slices (centered in the same focal plane as for the time-lapse acquisition) with a 0.5 µm step was acquired for every position, again in order to capture several cellular structures that could be of interest to analyze. Fluorescence images were acquired using the Intensilight Hg Pre-Centered Fiber Illuminator (Nikon) exciting the sample either in the 528-553 nm, 465-495 nm or 340-380 nm ranges to obtain either red, green or blue fluorescence images, respectively. Additionally, in order to produce super-resolution images of the fixed cells using SRRF, 100 fluorescence images were taken in a row of each position containing cells of interest, in the desired focal plane and for each desired fluorescence channel.

After image acquisition, fluorescence images were selected in FIJI for correlation with the time-lapse images. Specifically, we selected the XY positions containing the cells of interest for further analysis, together with the slice of each Z-stack that better depicted each stained structure in detail.

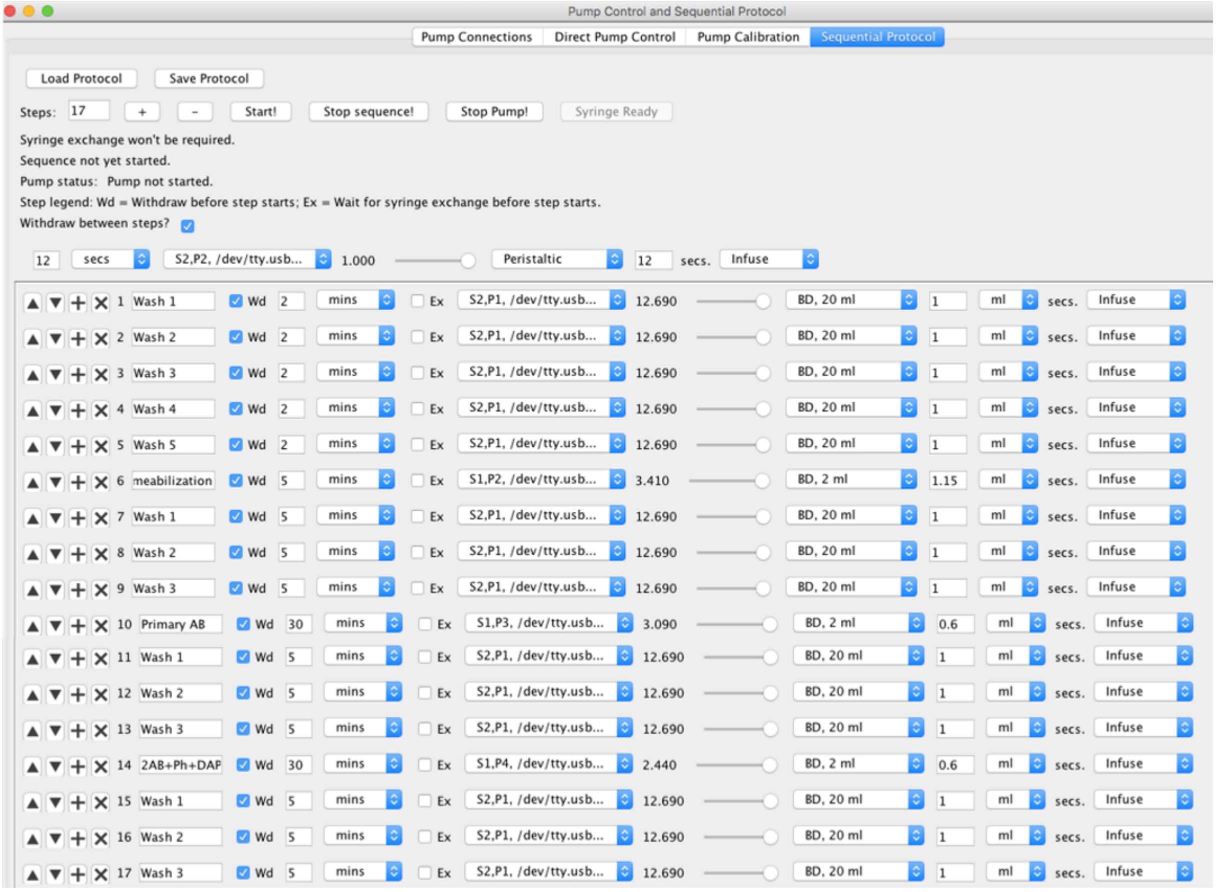

Steps: 17

Syringe exchange won't be required.

Sequence not yet started.

Pump status: Pump not started.

Step legend: Wd = Withdraw before step starts; Ex = Wait for syringe exchange before step starts.

Withdraw between steps? ☑

12 secs S2,P2, /dev/tty.usb... 1.000 Peristaltic 12 secs. Infuse

1	Wash 1	☑ Wd	2	mins	☐ Ex	S2,P1, /dev/tty.usb...	12.690	BD, 20 ml	1	ml	secs.	Infuse
2	Wash 2	☑ Wd	2	mins	☐ Ex	S2,P1, /dev/tty.usb...	12.690	BD, 20 ml	1	ml	secs.	Infuse
3	Wash 3	☑ Wd	2	mins	☐ Ex	S2,P1, /dev/tty.usb...	12.690	BD, 20 ml	1	ml	secs.	Infuse
4	Wash 4	☑ Wd	2	mins	☐ Ex	S2,P1, /dev/tty.usb...	12.690	BD, 20 ml	1	ml	secs.	Infuse
5	Wash 5	☑ Wd	2	mins	☐ Ex	S2,P1, /dev/tty.usb...	12.690	BD, 20 ml	1	ml	secs.	Infuse
6	meabilization	☑ Wd	5	mins	☐ Ex	S1,P2, /dev/tty.usb...	3.410	BD, 2 ml	1.15	ml	secs.	Infuse
7	Wash 1	☑ Wd	5	mins	☐ Ex	S2,P1, /dev/tty.usb...	12.690	BD, 20 ml	1	ml	secs.	Infuse
8	Wash 2	☑ Wd	5	mins	☐ Ex	S2,P1, /dev/tty.usb...	12.690	BD, 20 ml	1	ml	secs.	Infuse
9	Wash 3	☑ Wd	5	mins	☐ Ex	S2,P1, /dev/tty.usb...	12.690	BD, 20 ml	1	ml	secs.	Infuse
10	Primary AB	☑ Wd	30	mins	☐ Ex	S1,P3, /dev/tty.usb...	3.090	BD, 2 ml	0.6	ml	secs.	Infuse
11	Wash 1	☑ Wd	5	mins	☐ Ex	S2,P1, /dev/tty.usb...	12.690	BD, 20 ml	1	ml	secs.	Infuse
12	Wash 2	☑ Wd	5	mins	☐ Ex	S2,P1, /dev/tty.usb...	12.690	BD, 20 ml	1	ml	secs.	Infuse
13	Wash 3	☑ Wd	5	mins	☐ Ex	S2,P1, /dev/tty.usb...	12.690	BD, 20 ml	1	ml	secs.	Infuse
14	2AB+Ph+DAP	☑ Wd	30	mins	☐ Ex	S1,P4, /dev/tty.usb...	2.440	BD, 2 ml	0.6	ml	secs.	Infuse
15	Wash 1	☑ Wd	5	mins	☐ Ex	S2,P1, /dev/tty.usb...	12.690	BD, 20 ml	1	ml	secs.	Infuse
16	Wash 2	☑ Wd	5	mins	☐ Ex	S2,P1, /dev/tty.usb...	12.690	BD, 20 ml	1	ml	secs.	Infuse
17	Wash 3	☑ Wd	5	mins	☐ Ex	S2,P1, /dev/tty.usb...	12.690	BD, 20 ml	1	ml	secs.	Infuse

Figure 3.6: Sequential protocol defined in the NanoJ-Fluidics GUI for a cell staining procedure. The fixation step is not included as it was performed manually.

3.18 SRRF imaging of fixed cells

With the goal of obtaining images containing cellular structures with more definition than that achieved with widefield fluorescence imaging, SRRF images were produced in FIJI using the plugin “Nano-J SRRF” and choosing “SRRF Analysis”. For each fluorescence channel of interest, namely red for vinculin and green for actin, 100 fluorescence images of a cell of interest were given as input and the default parameters of the software were used, as they were found to be optimal for image quality overall. To analyze the sharpness of the structures obtained with SRRF and compare it with that of the widefield fluorescence images, phalloidin staining images of a chosen cell were used, in which the intensity profiles of the pixels sitting in a small line drawn perpendicularly to an actin filament were traced in FIJI for both the widefield fluorescence image and its corresponding SRRF image. The same process was applied in an area where an indistinguishable number of actin filaments could be seen in the fluorescence widefield image, but apparently clearer in the SRRF image.

Chapter 4

Results

4.1 MDA cells migrating through 2, 3 and 5 µm-wide constrictions

Time-lapse brightfield and fluorescence image acquisitions of MDA cells migrating through the microdevice constrictions were successfully obtained, for all constriction widths and siRNA transfection conditions. For the first migration experiments that were performed, the MDA cell line expressing NLS-GFP and LifeActin-mcherry was used, meaning that both green and red fluorescence images were obtained for observation of the cell nuclei and actin filaments, respectively. However, technical problems of various nature occurred throughout the experiments, thus altering the overall experimental work timeline, and consequently contributing to the decision of abandoning the initial goal of analyzing the dynamics of actin filaments from LifeActin-mcherry fluorescence signal. Hence, given that most of the experiments were carried out with MDA cells expressing NLS-GFP alone and that no analysis on fluorescence signal from actin filaments was performed, only images with green fluorescence signal from the cell nuclei are shown here. Representative time-lapse images of MDA cells transfected with control, Eps8L2 or Ctdnep1 siRNA migrating through constrictions of different widths can be seen in Figures 4.1, 4.2 and 4.3, respectively, showing only cells for which quantification of migration dynamics was performed. For cells transfected with Ctdnep1 siRNA, no quantification of cell migration through 2 µm-wide constrictions was performed due to lack of reliable data for quantification in these conditions.

As exemplified in Figures 4.1, 4.2 and 4.3, cells migrated through the constrictions formed by micropillars according to the chemotactic gradient of HGF, as it was expected. Cells, most noticeably the nuclei, underwent deformation to fit into the constrictions of several dimensions, having deformed more significantly for narrower constrictions. The first contact of each cell with a constriction was with the cytoplasm, which was extended and reshaped to fit into the constriction. The nucleus of the cell then underwent a squeezing mechanism to fit through the constriction, resembling the side view of a biconcave discoid when in the middle of the constriction. As the cell exited the constriction, the nucleus regained its original shape, even for the narrowest constrictions, suggesting that these nuclear deformations are fully reversible. These highly pronounced changes in the shape of the nucleus have been observed *in vivo* during cancer cell spreading [78, 79] and diapedesis [80].

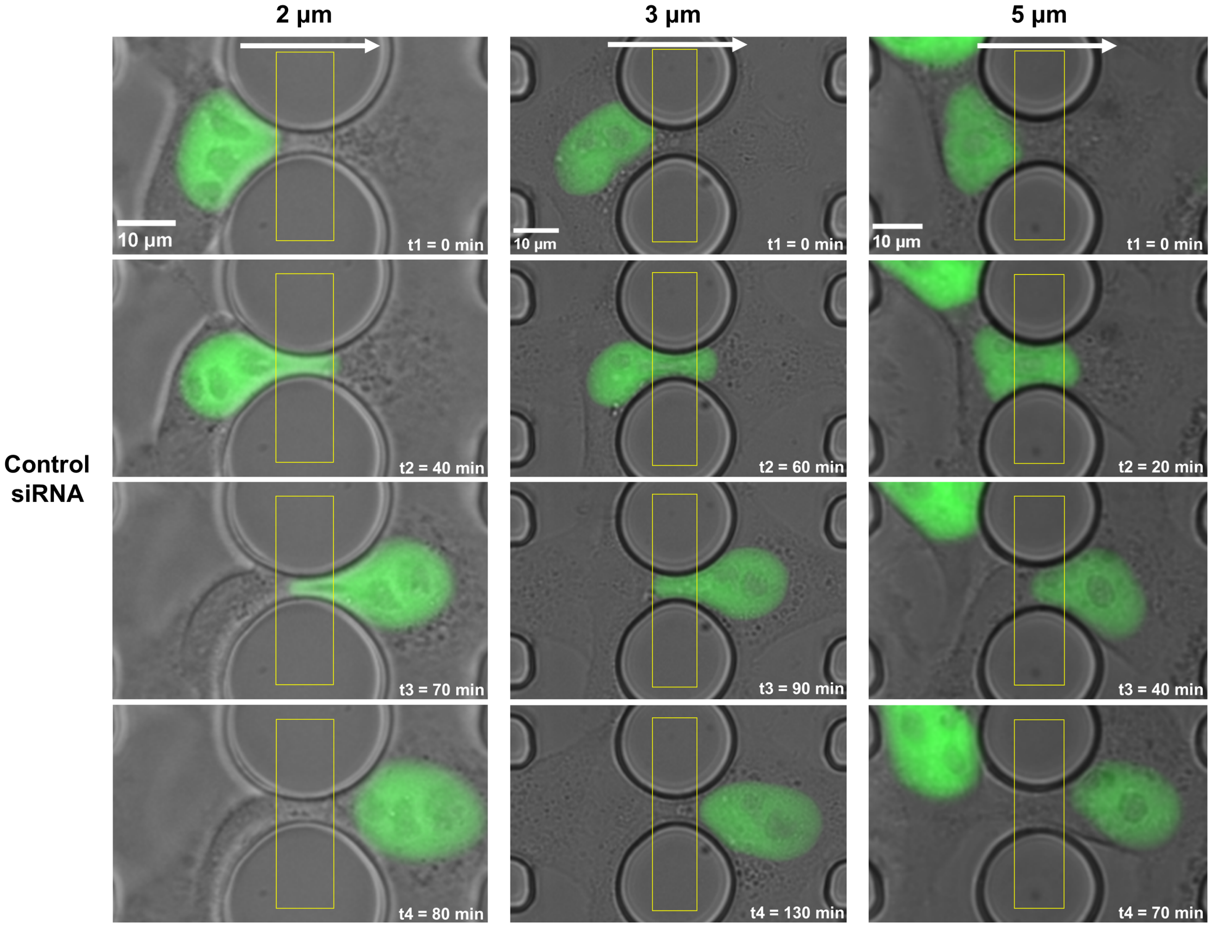

Figure 4.1: Selected frames from widefield microscopy (brightfield and fluorescence images overlapped) time-lapse recordings of three different cells transfected with control siRNA migrating through PDMS microconstrictions with 2, 3 and 5 µm of width, respectively, in which the cell nucleus is marked with NLS-GFP. The four selected frames for each cell represent the frames at which the time points $t1$, $t2$, $t3$ and $t4$ were measured, respectively. Arrows indicate migration direction according to HGF gradient.

The time period between acquisitions of the cell migration time-lapses that was chosen, 10 minutes, demonstrated to be appropriate, being well-adjusted to the migratory capacity of these cells in this environment. On one hand, it was long enough to ensure the acquisition of all selected positions in the device and respective Z-stacks, as well as to avoid the generation of excessively heavy data files. On another hand, it was short enough to observe the cell nuclei reaching each relevant time point in the constriction area for the quantification of confined nuclear migration dynamics.

It can be seen from Figures 4.1, 4.2 and 4.3 that the PDMS micropillars do not seem to have constant shape and size for constrictions of the same width, as it would be expected from the way the device was designed. This could be due to several factors involving the condition of the device SU-8 molds and PDMS devices preparation.

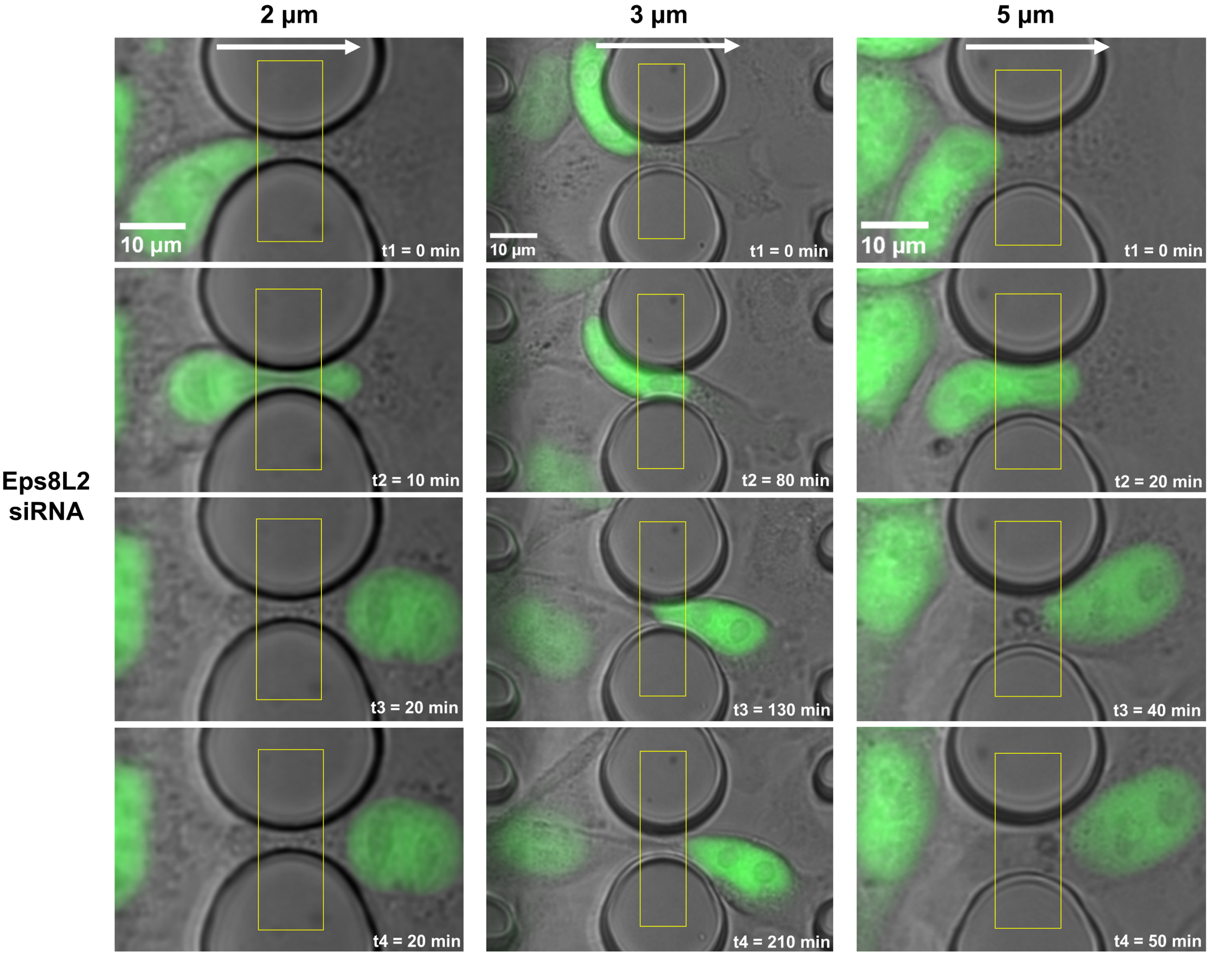

Figure 4.2: Selected frames from widefield microscopy (brightfield and fluorescence images overlapped) time-lapse recordings of three different cells transfected with Eps8L2 siRNA migrating through PDMS microconstrictions with 2, 3 and 5 µm of width, respectively, in which the cell nucleus is marked with NLS-GFP. The four selected frames for each cell represent the frames at which the time points $t1$, $t2$, $t3$ and $t4$ were measured, respectively. Arrows indicate migration direction according to HGF gradient.

4.2 Measurement of microconstriction widths

In order to assess how similar the constriction widths of the microdevices were when compared to the widths of the original device design, namely 2 µm, 3 µm and 5 µm, the distances between round micropillars for all cells that were quantified were measured. A plot containing all the measurements made for each constriction width category is presented in Figure 4.4.

It can be observed in Figure 4.4 that the means of the distances measured between round micropillars are higher than the expected values, for all constriction types. This could be a consequence of the conditions of the mold that was used for the fabrication of the devices and of a shrinkage effect that cured PDMS can experience [81–84]. Additionally, there is a high variability in the measured distance between round micropillars among each constriction width category, and there is even an overlap between measurements of constrictions belonging to different types of micropillar sections in device. An explanation for this could be the fact that PDMS shrinkage effect does not always occur to the same extent.

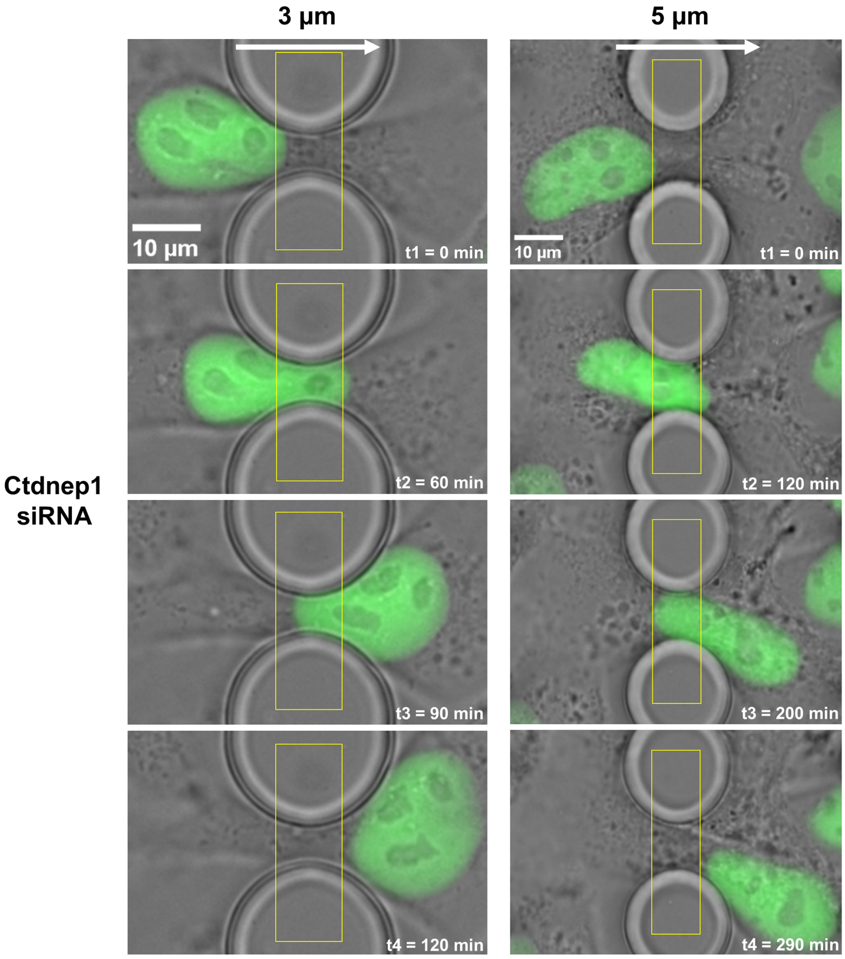

Figure 4.3: Selected frames from widefield microscopy (brightfield and fluorescence images overlapped) time-lapse recordings of two different cells transfected with Ctdnep1 siRNA migrating through PDMS microconstrictions with 3 and 5 µm of width, respectively, in which the cell nucleus is marked with NLS-GFP. The four selected frames for each cell represent the frames at which the time points $t1$, $t2$, $t3$ and $t4$ were measured, respectively. Arrows indicate migration direction according to HGF gradient.

4.3 Confined migration of MDA cells transfected with control siRNA

Quantification of nuclear migration through the micropillar constrictions of the PDMS devices was performed as described in the Materials and Methods chapter (section 3.8). In brief, the duration of each period of nuclear migration through the constriction – enter, cross, exit and transit – was calculated and plots were created in GraphPad Prism 8. First, the duration of each nuclear migration period for the cells transfected with control siRNA was plotted for all three constriction widths, namely 2 µm, 3 µm and 5 µm, to assess if the constriction size had an effect on the duration of the migration periods (see Figure 4.5).

As it can be observed from Figure 4.5 and respective statistical analysis, no statistically significant difference among means of each period duration for different constriction sizes could be found. This data suggests that constriction sizes does not influence nuclear migration dynamics under confinement, namely the velocity of nuclear migration through a constriction.

In order to visualize the data from cells transfected with control siRNA on another perspective and

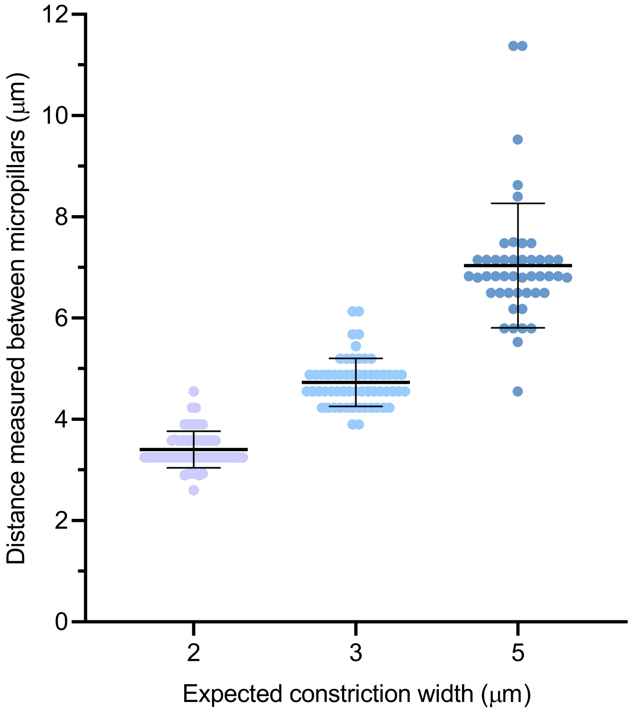

Figure 4.4: Distances measured between round micropillars for all cells whose nuclear migration dynamics were quantified, for each constriction width category (2 µm, 3 µm and 5 µm). For each column, the mean and standard deviation of the data are represented with black lines. n = 57 cells for the 2 µm-wide constrictions group, n = 58 cells for the 3 µm-wide constrictions group, and n = 46 cells for the 5 µm-wide constrictions group.

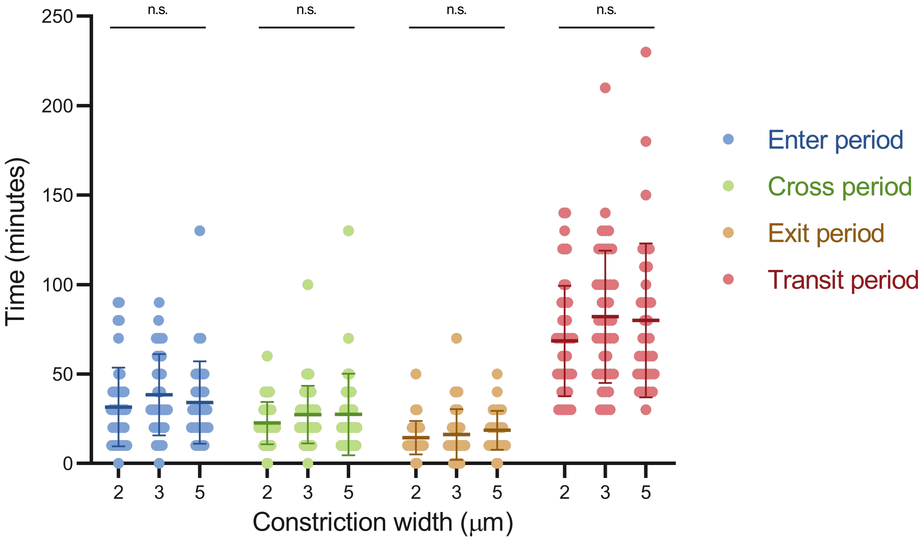

Figure 4.5: Duration of each nuclear migration period for different constriction widths in NLS-GFP-expressing MDA cells transfected with control siRNA. For each column, the mean and standard deviation of the data are represented with darker-colored lines. n = 46 cells for the 2 µm-wide constrictions group, n = 45 cells for the 3 µm-wide constrictions group, and n = 35 cells for the 5 µm-wide constrictions group. n.s., non-significant, $p > 0.05$ (ANOVA test).

establish different comparisons between groups, the duration of the several nuclear migration periods was plotted for each constriction width, namely 2 µm, 3 µm and 5 µm, to study how nuclear migration periods are different from one another (see Figure 4.6).

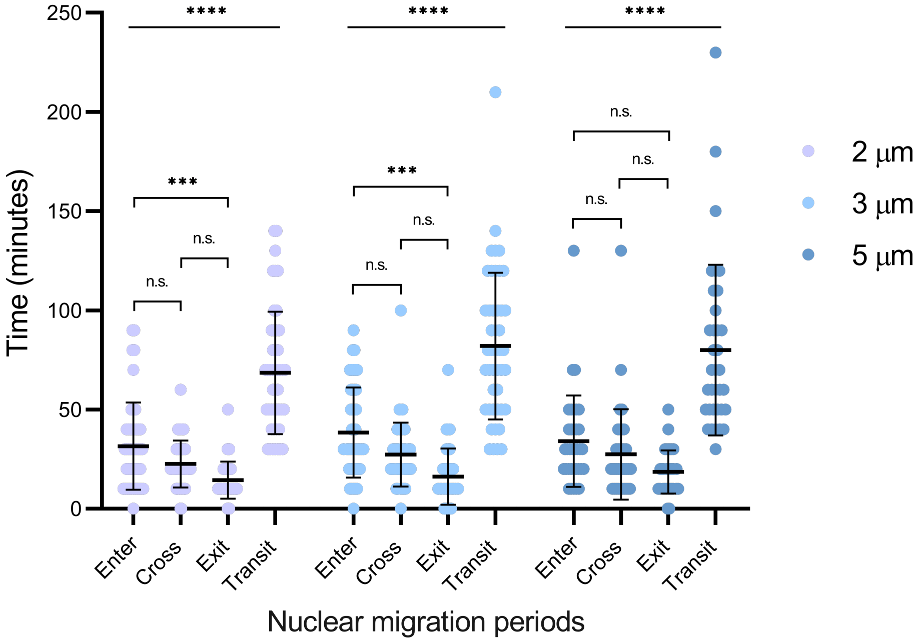

Figure 4.6: Duration of all nuclear migration periods for each constriction width in NLS-GFP-expressing MDA cells transfected with control siRNA. For each column, the mean and standard deviation of the data are represented with black lines. n = 46 cells for the 2 µm-wide constrictions group, n = 45 cells for the 3 µm-wide constrictions group, and n = 35 cells for the 5 µm-wide constrictions group. ****, $p < 0.0001$ (ANOVA test). n.s., non-significant, $p > 0.05$; ***, $p = 0.005$ for the 2 µm group and $p = 0.001$ for the 3 µm group (Tukey's multiple comparisons test).

Figure 4.6 and respective statistical analysis of the data show that there was a statistically significant difference among means of nuclear migration periods for each constriction size. Further statistical analysis revealed that the means of the enter and exit periods were significantly different from one another for the 2 and 3 µm-wide constriction cell groups, suggesting, together with the visual representation of the data in the plot, that the exit period is shorter than the enter period for constrictions of smaller widths. For the 5 µm-wide constriction cell groups, however, these two periods do not seem to be significantly different.

4.4 Effect of siRNA transfection in MDA cells for confined nuclear migration

To analyze the effect of MDA cell transfection with the different siRNAs in confined cell migration, each nuclear migration period for cells transfected with control, Eps8L2 and Ctdnep1 siRNA was plotted for all three constriction widths, namely 2 µm, 3 µm and 5 µm. The resulting plots can be found in Figures 4.7, 4.8 and 4.9, respectively.

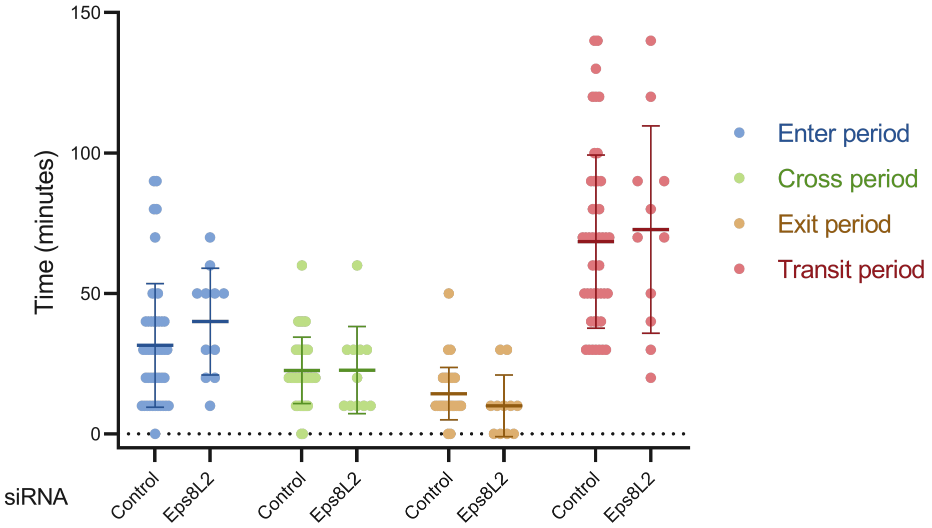

Figure 4.7: Duration of each nuclear migration period for NLS-GFP-expressing MDA cells transfected with control siRNA and Eps8L2 siRNA migrating through 2 µm-wide constrictions. For each column, the mean and standard deviation of the data are represented with darker-colored lines. n = 46 for cells transfected with control siRNA and n = 11 for cells transfected with Eps8L2 siRNA.

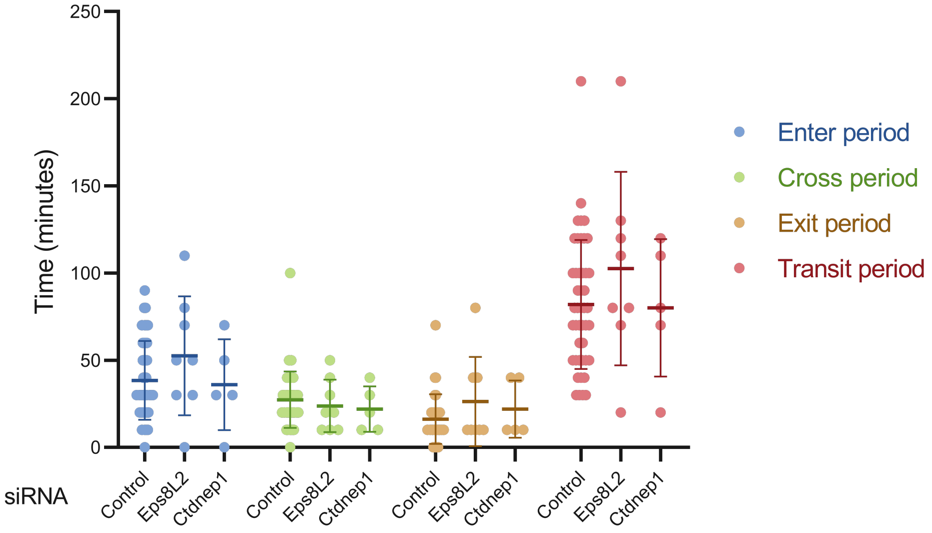

Figure 4.8: Duration of each nuclear migration period for NLS-GFP-expressing MDA cells transfected with control, Eps8L2 or Ctdnep1 siRNA migrating through 3 µm-wide constrictions. For each column, the mean and standard deviation of the data are represented with darker-colored lines. n = 45 for cells transfected with control siRNA, n = 8 for cells transfected with Eps8L2 siRNA and n = 5 for cells transfected with Ctdnep1 siRNA.

Due to the lack of quantification data from cells transfected with Eps8L2 and Ctdnep1 siRNA when compared to the data obtained from cells transfected with control siRNA, statistical analysis was not performed to compare these groups of data, as the results could potentially be unreliable due to the discrepancy in data quantity. Moreover, when analyzing the plots in Figures 4.7, 4.8 and 4.9, no obvious effect from transfection with Eps8L2 or Ctdnep1 siRNA in the nuclear migration periods can be seen in comparison with the values from cells transfected with control siRNA. An exception to this observation

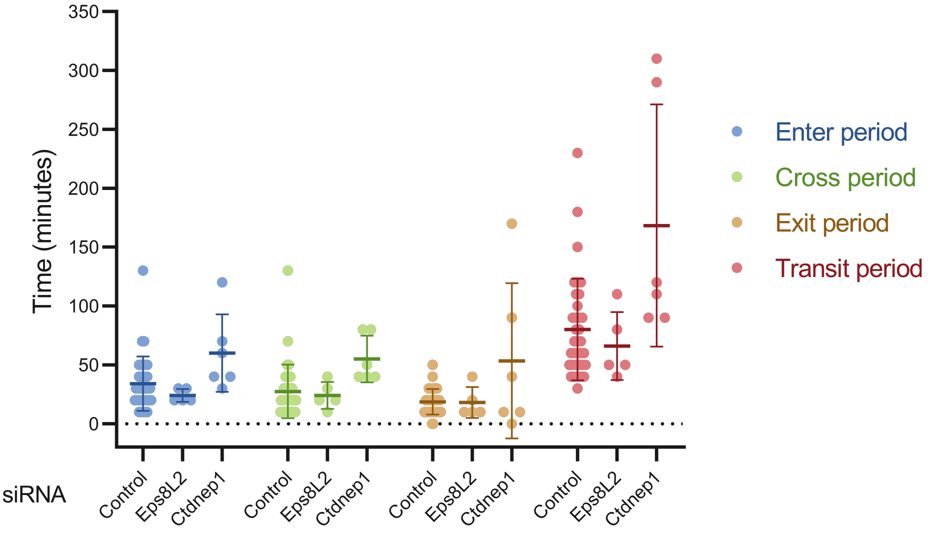

Figure 4.9: Duration of each nuclear migration period for NLS-GFP-expressing MDA cells transfected with control, Eps8L2 or Ctdnep1 siRNA migrating through 5 µm-wide constrictions. For each column, the mean and standard deviation of the data are represented with darker-colored lines. n = 35 for cells transfected with control siRNA, n = 5 for cells transfected with Eps8L2 siRNA and n = 6 for cells transfected with Ctdnep1 siRNA.

is, perhaps, the group of cells migrating through 5 µm-wide constrictions (Figure 4.9) where the means of the nuclear migration periods for cells transfected with Ctdnep1 siRNA are consistently higher than the values for the other conditions.

4.5 Widefield images from correlative microscopy experiments

Correlative microscopy experiments were carried out with NIH 3T3 fibroblasts using the assembled NanoJ-Fluidics set-up as described in the Materials and Methods chapter. The staining procedure was performed successfully using the defined sequential protocol, and it was possible to obtain both phase contrast images from live imaging and fluorescence images from fixed imaging of the same cells, allowing the correlation of cell dynamics with structural information from the cell staining.

When doing live imaging of cells, it was noticed that there were cells which were more static and did not seem to migrate or expand, and there were cells which, on the other hand, were more dynamic and migrated during the 30-minute acquisition period. For this reason, it seemed interesting to compare the structures of these cells after the staining procedure, while also correlating the fluorescence images from the fixed cells with the images from the phase contrast time-lapse, specifically the last frame. Widefield images from ”static” and ”dynamic” cells in the sample before and after the staining procedure with NanoJ-Fluidics can be seen in Figures 4.10 and 4.11, respectively.

As it can be seen from Figure 4.10B, the cell on top of the selected sample region did not migrate throughout the time-lapse acquisition, while the cell from Figure 4.11B migrated and spread between acquisitions. When viewing the staining images from both cells (see Figures 4.10C and 4.11C), it is possible to conclude that the last frame from live imaging was correctly correlated with an image con-

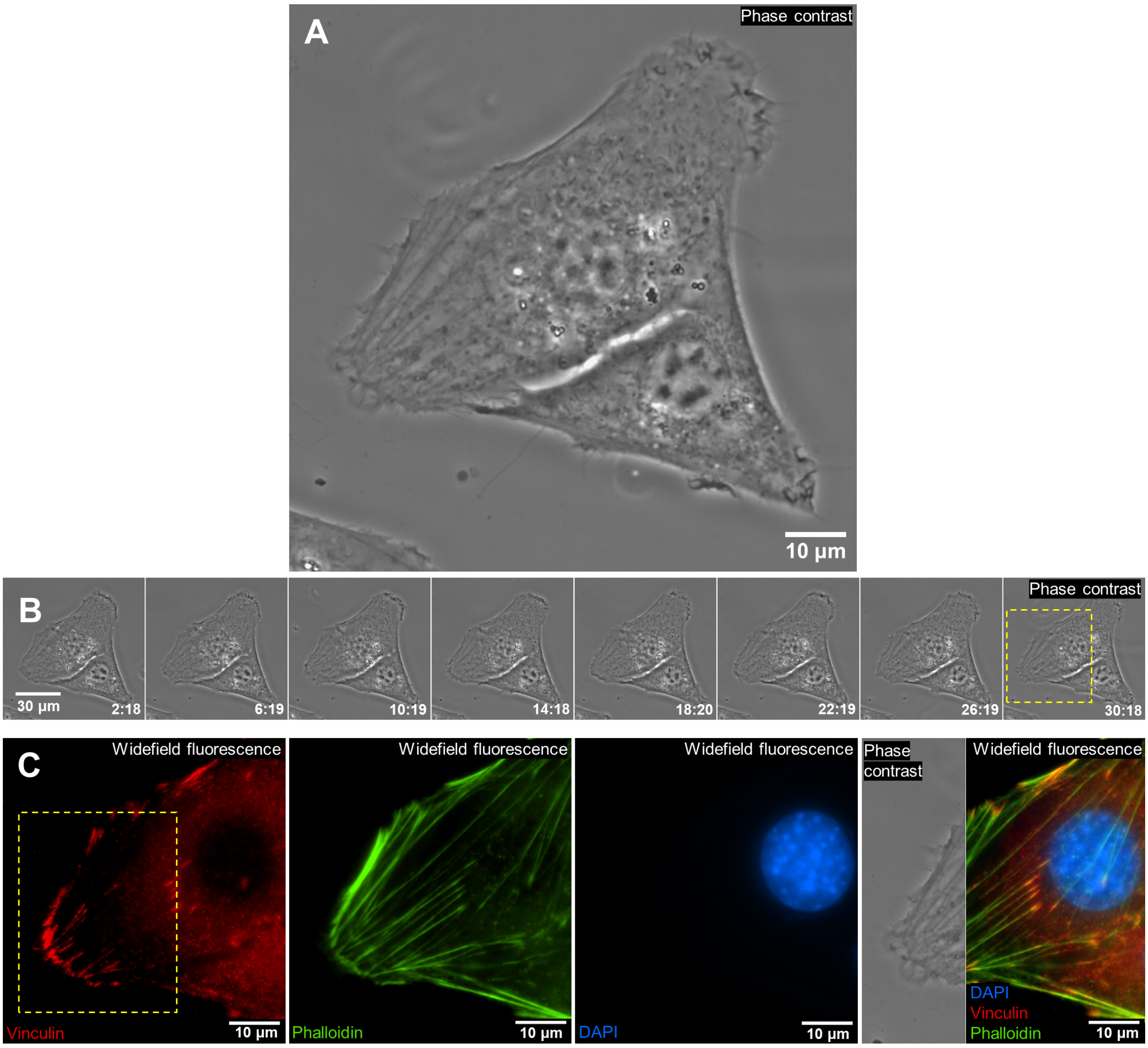
A
Phase contrast
10 µm
B
30 µm
2:18
6:19
10:19
14:18
18:20
22:19
26:19
Phase contrast
30:18
C
Widefield fluorescence
Vinculin
10 µm
Widefield fluorescence
Phalloidin
10 µm
Widefield fluorescence
DAPI
10 µm
Phase contrast
Widefield fluorescence
DAPI
Vinculin
Phalloidin
10 µm

Figure 4.10: **Widefield images of ”static” cell(s) in the sample obtained before and after performing a staining procedure using NanoJ-Fluidics.** (A) Widefield phase contrast image from two ”static” cells in the sample immediately before fixation. (B) Frames from a time-lapse recording of the cells represented in (A), where the last frame is the last image acquired right before fixation. (C) Widefield fluorescence images of the top cell represented in (A) acquired after the staining procedure (selected region indicated by the yellow rectangle in (B)). From left to right: vinculin staining (red), actin staining with phalloidin (green), nucleus staining with DAPI (blue), and a portion from the last frame of the time-lapse next to a fluorescence image of the three staining images overlapped. The image of the DAPI staining is from a different focal plane than that of the remaining staining images, in order to allow a good visualization of all stained structures.

taining all fluorescence channels from the cell staining overlapped. Regarding differences between the fluorescence images from the two cells, which include staining for vinculin, present in focal adhesions, actin filaments and the nucleus, Figure 4.10C shows that the ”static” cell had a high amount of actin stress fibers with focal adhesions in their extremities, while Figure 4.11C shows that the ”dynamic” cell did not have these structures, showing less defined actin filaments instead and less localized vinculin. These observations suggest that the cell on top of the selected sample region depicted in Figure 4.10A could be migrating in a mesenchymal mode, while the cell depicted in Figure 4.11A could be migrating

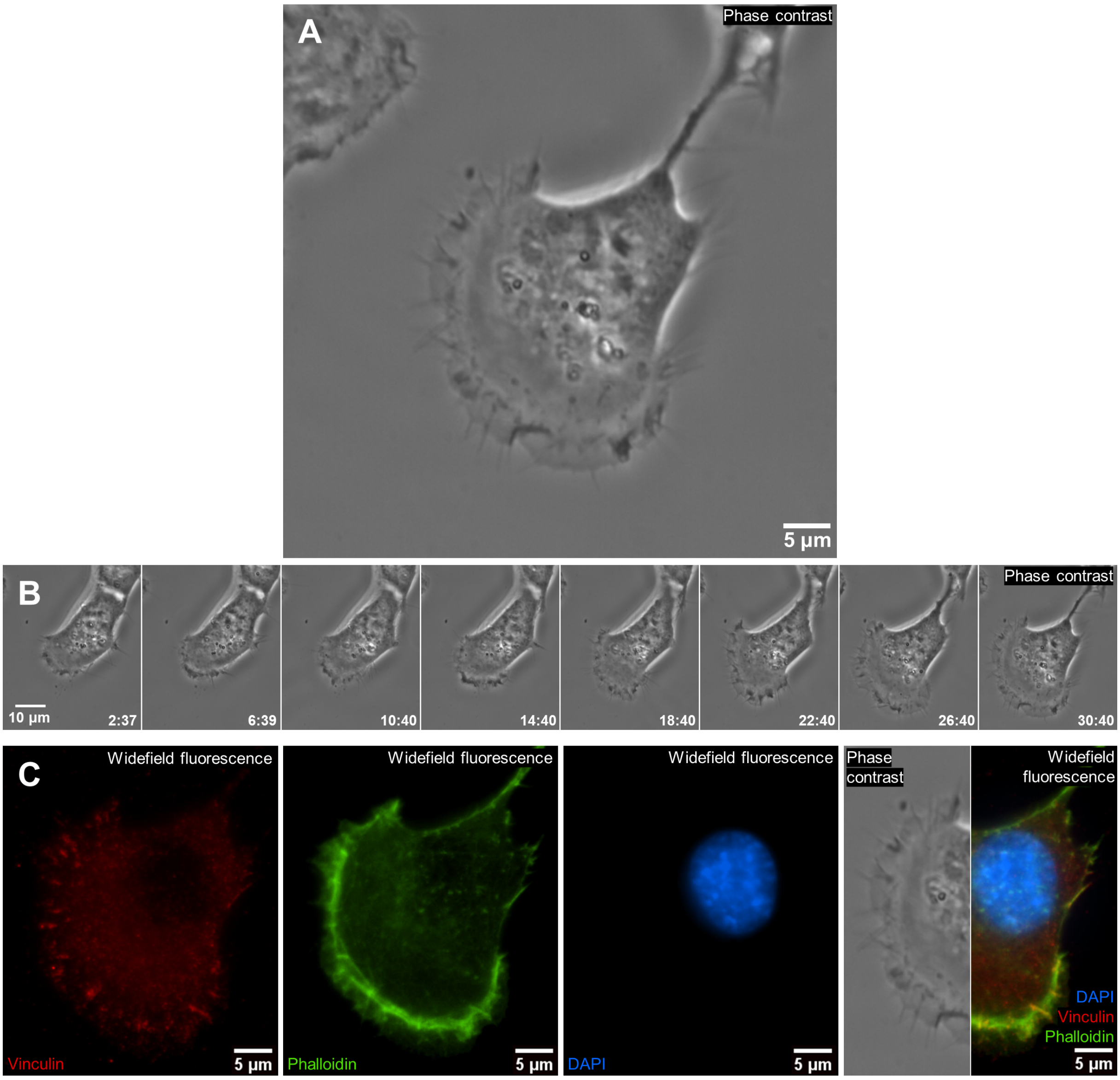
A
Phase contrast
5 µm
B
Phase contrast
10 µm
2:37
6:39
10:40
14:40
18:40
22:40
26:40
30:40
C
Widefield fluorescence
Vinculin
5 µm
Widefield fluorescence
Phalloidin
5 µm
Widefield fluorescence
DAPI
5 µm
Phase contrast
Widefield fluorescence
DAPI
Vinculin
Phalloidin
5 µm

Figure 4.11: **Widefield images of a ”dynamic” cell in the sample obtained before and after performing a staining procedure using NanoJ-Fluidics.** (A) Widefield phase contrast image from a ”dynamic” cell in the sample immediately before fixation. (B) Frames from a time-lapse recording of the cell represented in (A), where the last frame is the last image acquired right before fixation. (C) Widefield fluorescence images of the cell represented in (A) acquired after the staining procedure. From left to right: vinculin staining (red), actin staining with phalloidin (green), nucleus staining with DAPI (blue), and a portion from the last frame of the time-lapse next to a fluorescence image of the three staining images overlapped. The image of the DAPI staining is from a different focal plane than that of the remaining staining images, in order to allow a good visualization of all stained structures.

in an amoeboid mode, given the key differences between these two modes of migration, which were described in the Background chapter (subsection 2.1.2). This hints that, with correlative microscopy using the NanoJ-Fluidics system, it is possible to identify and visualize different modes of cell migration in two dimensions.

4.6 SRRF imaging of fixed cells

After the acquisition of fluorescence images to visualize the cell staining performed with the system, SRRF images were obtained from fluorescence images to analyze how much better resolution the generated images had in comparison with the widefield images. It was possible to generate SRRF images from the cells shown in Figures 4.10 and 4.11 with relatively good quality. The resulting images can be found in Figures 4.12 and 4.13.

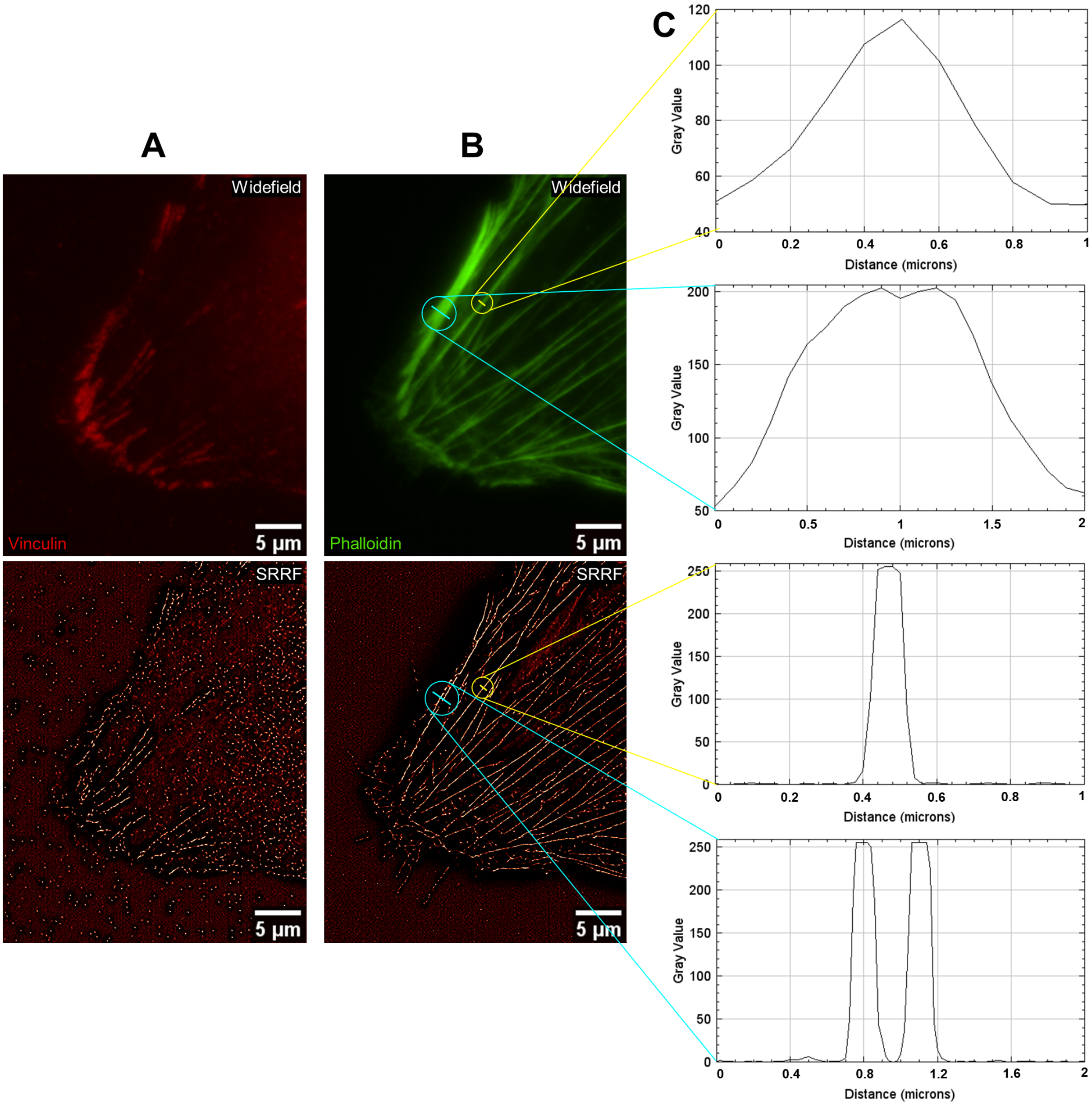
C
A
B
Widefield
Widefield
Vinculin
5 µm
Phalloidin
5 µm
SRRF
SRRF
5 µm
5 µm
Gray Value
Distance (microns)
120
100
80
60
40
0
0.2
0.4
0.6
0.8
1
200
150
100
50
0
0.5
1
1.5
2
250
200
150
100
50
0
0.4
0.8
1.2
1.6

Figure 4.12: **Widefield fluorescence and SRRF images from the vinculin and phalloidin staining of the top cell shown in Figure 4.10 (selected region indicated by the yellow rectangle in Figure 4.10C).** (A) and (B) Widefield fluorescence (top) and SRRF (bottom) images from vinculin (A) and phalloidin (B) staining. Each fluorescence image was selected from the 100 raw frames that were used to produce each SRRF image. (C) Intensity profiles of the pixels selected by the yellow and blue rectangular lines in (B) from the fluorescence image of the phalloidin staining (top two plots) and its corresponding SRRF image (bottom two plots).

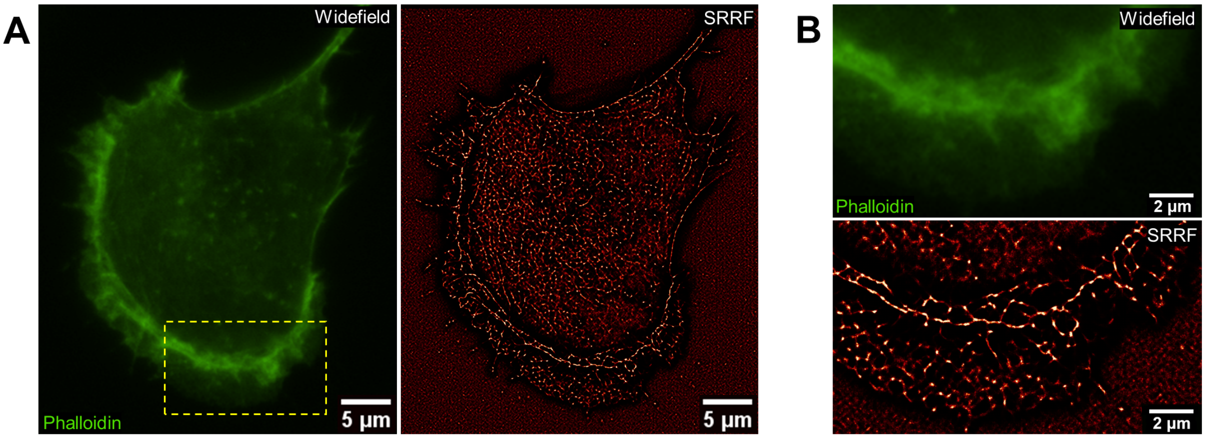

Figure 4.13: **Widefield fluorescence and SRRF images from the phalloidin staining of the cell shown in Figure 4.11.** (A) Widefield fluorescence (left) and SRRF (right) images from the phalloidin staining. The fluorescence image was selected from the 100 raw frames that were used to produce the SRRF image. (B) Close-up of the selected cell region indicated by the yellow rectangle in (A) – fluorescence image from the phalloidin staining at the top and corresponding SRRF image at the bottom.

From Figures 4.12 and 4.13, it is possible to infer that the SRRF images were able to provide a sharper visualization of the stained structures, especially actin filaments, when compared to their corresponding widefield fluorescence images. In particular, the pixel intensity profiles from Figure 4.12C show that the SRRF image resolves better the actin filaments than the widefield fluorescence image. In Figure 4.13B it is also possible to see that the SRRF image allows a clearer visualization of the actin filaments when compared to the widefield fluorescence image.

Chapter 5

Discussion

With the implemented methodology, it was possible to observe MDA cells transfected with control, Eps8L2 or Ctdnep1 siRNA migrating through microconstrictions of different widths, namely 2 µm, 3 µm or 5 µm. Successful cell transmigration implicated significant nucleus deformation, especially for narrower constrictions. We observed that PDMS micropillars exhibited inconstant shape and size for constrictions of the same width, and found large discrepancies for the measured constriction widths. Regarding the quantification of nuclear transmigration dynamics of MDA cells transfected with control siRNA, we did not find a statistically significant difference among means of nuclear migration periods for different constriction widths. On the contrary, we found that the enter period was statistically significant higher than the exit period for cells migrating through 2 and 3 µm-wide constrictions. Concerning transfection of MDA cells with the different siRNAs, we did not obtain sufficient data from cells transfected with Eps8L2 and Ctdnep1 siRNA, and thus no statistical analysis was performed to compare the results from the different siRNA transfection groups. As for the correlative microscopy experiments NIH 3T3 fibroblasts, we could successfully correlate cell dynamics from live-cell imaging with structural information from fixed-cell imaging by employing an automatic staining protocol with NanoJ-Fluidics. Moreover, it was possible to observe different types of cellular dynamics in the sample, namely cells employing mesenchymal and amoeboid modes of migration, and respective differences in cellular structures. Finally, SRRF images were successfully generated from fluorescence images of the stained cells, which indeed allowed a sharper visualization of certain cellular structures, in particular actin filaments.

5.1 Aspects affecting quantification of MDA cell migration in PDMS devices

As mentioned in the Results chapter (section 4.1), several technical issues occurred throughout the experiments with migration devices which hampered the experimental work that was planned, resulting in the obtainment of less results than it was desired. One of the most significant issues that occurred several times in the experiments under the microscope was focus drift, that is, the alteration of the focal plane of the sample, in the time-lapse acquisition experiments. An explanation for this is thermal drift occurring on the sample and microscope, which can be caused by changes in air flow and room temperature the experiment, for example [85]. Additionally, vibrations and mechanical relaxation might contribute to focus drift in the sample [86, 87]. Although in most cases this loss of focus was compensated by the extra image slices obtained from the Z-stack acquisitions, in other cases it was not, thus impeding the quantification of cell migration as the device and cell nuclei structures were not defined enough to ensure a reliable quantification. To address this issue, automatic focus strategies were employed in the ZEN software, though they did not prove useful as the composition of the sample, namely the device with cells on different focal planes, was too complex for the software to be able to maintain focus.

Besides issues with image acquisition on the microscope, there were also cases in which some micropillar sections of the devices did not have enough quality for quantification of cell migration, namely the presence of defects in the PDMS microstructures. This occurred occasionally probably in part due to imperfect peeling of the PDMS from the devices mold. Also, as the molds that were used for device making had already been used previously for a significant amount of time, they were not in impeccable conditions, meaning that the round micropillars did not have a perfect circular shape. Quantification was still performed in cases where the micropillars did not have a perfectly round shape, except when the structure was too flawed to ensure a reliable quantification.

Incomplete PDMS bonding to the glass slides also occurred occasionally, making the quantification for micropillars that were not properly attached to the glass impossible, as the cells migrated underneath the PDMS pillars. This could happen due to not enough pressure being applied when the device is pressed against the glass slide for bonding [88]. Another way to improve adhesion of the PDMS to the glass would be to place the devices already attached to a glass cover slip onto a hot plate at 95° C for 5 minutes [88]. This was not performed as it did not seem necessary given that the devices were properly attached to the glass in almost all cases.

Air bubbles in the medium were also present in the device channels in some cases. This occurred mainly due to medium evaporation in the first experiments that were performed, which was caused by improper sealing of the glass cover slips onto the PDMS devices for the acquisitions under the microscope. To overcome this, the class cover slips were gently pressed against the device before taking the sample to the microscope so that they were better sealed onto the PDMS. Another explanation for the presence of air bubbles within the device is unintentional injection of air into the devices when performing cell seeding or medium change [88]. The presence of air bubbles within the device and medium evaporation affected cell migration, thus preventing quantification from being accomplished in these.

Another factor that significantly hampered quantification of cell migration was the presence of too many cells in the devices. With a large number of cells migrating in the micropillar areas of the device, cell migration of individual cells becomes affected as the cells can block or push one another, thus possibly increasing or decreasing the nuclear migration periods through the constrictions. The main explanation for the presence of a high number of cells inside the devices was the need to get a large quantity of cells inside the devices, in particular in the area with the micropillars, in order to increase the changes of having cells whose migration to quantify. In a lot of experiments, the quantity of cells that were seeded into the devices was not enough, making the imaging of certain micropillar sections useless in a lot of cases. This called for the need to attempt to seed more cells into the devices, and hence the performance of cell seeding multiple times through the same device cell inlets as described in the Materials and Methods chapter (section 3.5). However, some devices inevitably ended up with too many cells inside, thus leading to the problems described above. For these reasons, it was complicated to find a balance between having too little cells and too many cells within the devices.

5.2 Size and shape of constriction pillars in migration devices

As shown in the Results chapter (see Figures 4.1 to 4.4), the size and shape of the round micropillars of the PDMS devices creating the constrictions for the cells to pass are not consistent among the same category of constriction width. In section 5.1, it was mentioned that imperfect shape of the micropillars was probably due to imperfect peeling of the cured PDMS away from the SU-8 mold and the fact that the molds used in this work were not new, thus probably being slightly deformed. Further exploring this matter, it is during the detachment of the PDMS replica from the mold that damage to the microstructures defined in the master or the replica typically occurs [83]. To overcome this, the molds for replica molding are usually coated with a fluorinated molecule or polymer to facilitate the separation of the two components [83], which was the case for the molds that were used in this work. Additionally, the use of elastomeric polymers (such as PDMS) in replica molding contributes to the preservation of the device microstructures [83]. Despite this, we still observed the deformation of micropillars in our devices.

Regarding the size of the micropillars, as it was seen in the Results chapter (section 4.2), it differs from the one of the original device microdesign, which can be explained by several reasons. When PDMS is cured at elevated temperatures, which was the case for the present work (70° C), it shrinks when compared to the mold dimensions [81–84]. Two characteristics that affect the quality of a polymer replica are the shrinkage that the polymer undergoes during curing and the coefficient of thermal expansion of the mold [83]. Polymer shrinkage can occur due to cross-linking of the polymer, evaporation of solvents and thermal expansion of the polymer, for curing at elevated temperature [83]. Molds or replicas made of polymers with large coefficients of thermal expansion, which is the case for PDMS, can have their dimensions altered due to changes in the temperature [83]. There can be several ways to overcome this issue, among which the two following exist: design the original mold to account for PDMS shrinkage during curing [81, 83, 84] and let PDMS cure at room temperature [81, 82, 84]. Curing PDMS at room temperature can be inconvenient as it takes much longer, such as an overnight period or even two days, than it would take at elevated temperatures, such as 1 hour, as for the present work [81, 82, 84]. Temperature induced shrinkage is not commonly included in the design probably due to the inexistence of reliable quantitative data on the degree of PDMS contraction [81]. For this reason, Madsen et al. (2014) reported a study of the shrinkage of PDMS with different mixing ratios and curing temperatures, ranging from 40° C to 120° C, and provided a model to allow for the correction of the design dimensions of a mold for PDMS fabrication [81]. If one desired to account for PDMS shrinkage when designing the mold for the device, this model could be used.

In what pertains to the variability of sizes among constrictions belonging to the same section type of the device, meaning that, in theory, their constriction widths should be the same, the PDMS shrinkage phenomenon can be an explanation. As it was said above, the degree of PDMS shrinkage can be complex to predict, since it depends on multiple factors and it is challenging to assure always the exact same conditions when preparing the PDMS devices. For example, it is difficult to ensure that the PDMS always stays the same exact amount of time in the oven at 70° C and at room temperature before being detached from the mold, as it is to always maintain a stable room temperature in the place where the devices are prepared. Hence, it is not so surprising that the shrinkage degree is not the same for all PDMS replicas that are fabricated, yielding variable results for constriction size even for the same constriction type.

5.3 Confined migration of MDA cells transfected with control siRNA

It was possible to quantify the dynamics of confined nuclear migration for a relatively high amount of MDA cells transfected with control siRNA. Hence, it is useful to analyze these data to investigate general aspects of confined cell migration before taking into consideration Eps8L2 and Ctdnep1 knockdown. In particular, using the quantification data from cells transfected with siRNA, it is possible to investigate the effect of constriction size on the nuclear migration periods, as well as analyze differences between these periods.

5.3.1 Effect of constriction size in nuclear migration periods

By analyzing Figure 4.5 from the Results chapter, it is possible to infer that no statistically significant difference among means of each period duration for different constriction sizes could be found. These results suggest that the size of the constriction through which the cell migrates does not affect nuclear migration dynamics, meaning that the nucleus of the cell does not migrate any faster or slower through constrictions of different sizes. Given the results that were obtained for the real constriction sizes of the migration devices, these results are not necessarily surprising. Figure 4.4 of the Results chapter shows that there is an overlapping to some extent between measurements of constrictions of supposedly different widths. For example, when considering the constrictions that were measured as being 4 µm-wide, it can be seen that part of those constrictions belongs to the 2 µm group, while the other part belongs to the 3 µm group. The same is seen for constrictions with widths between approximately 5 and 6 µm, part of them belonging to the 3 µm group and the rest belonging to the 5 µm group. Hence, with this data, it can be difficult to draw conclusions about the effect of constriction size on the nuclear migration dynamics of cells.

Despite the variability of constriction sizes verified in the present work, comparisons with the literature concerning the effect of constrictions of different dimensions on cell migration can still be performed. For example, Lautscham et al. (2015) thoroughly studied the migration of several cells, among which MDA-MB-231 cells, in PDMS devices with microconstrictions of varying widths (from 1.7 to 11.2 µm) in 3.7 µm-tall channels [51]. They found that cells altogether migrated at nearly constant velocity when passing constrictions wider than 8 µm, the nuclei of the cells not being visibly stretched, but that cell migration velocity when passing constrictions narrower than 8 µm started to oscillate due to a need for the nucleus to squeeze to fit through the constriction. The authors of this study also divided the nuclear migration dynamics through the constrictions into several periods, namely entrance, channel, and exit, and found that, gathering data from all cells, the entrance velocity decreased with decreasing constriction width, and that the exit velocity increased. However, when analyzing the data from MBA-MB-231 cells only, it was found that these cells migrated at approximately similar velocity in constrictions of varying widths, which is comparable to the results of this work.

Conversely, Irimia and Toner (2009) performed a study on cell migration with MDA-MB-231 cells using PDMS microfluidic devices with channels for confined cell migration that were 3 µm-tall [52]. The authors found that the velocity of cell migration increased with channel width ranging from 6 to 25 µm, as opposed to the present work. However, it is important to note that, besides the migration dynamics having been analyzed at the cell level and not at the nucleus level, the channel width range in which their experiments were performed was not the same as for the present work. In another study, Nath et al. (2019) found, using PDMS microdevices, that transit velocity for MDA-MB-468 breast cancer cells through confined gaps increased with increasing constriction width, for constriction sizes of 10, 12 and 15 µm, which was also verified for the constriction entry time alone [89]. Relatedly, a study by Fu et al. (2012) with MDA-MB-231 cells migrating through 5 µm-tall PDMS microchannels revealed that, the narrower the channel, comprising widths of 12, 8 and 4 µm, the lower the percentage of cells that migrated through the 100 µm long channels, due to the higher extent of deformation of the nucleus that is required for smaller microchannels [34]. Interestingly, transmigration of the cells did not occur when the microchannel width was reduced to 2 µm, which was not observed in the present work. It should be noted, however, that the 2 µm-wide constrictions through which cells migrated in this work were in reality wider than 2 µm, being in average between 3 and 4 µm-wide for cells whose nuclear migration dynamics were quantified. Furthermore, Wolf et al. (2013) found that, in the absence of matrix proteolysis, migration of MDA-MB-231 cells, among other cells, through 3D collagen matrices was affected by pore size [35]. In particular, for pore diameters ranging approximately from 1 to 6 µm, the speed of cell migration across pores increased with pore size. Similarly, Tong et al. (2012) found that the migration speed of HOS cancer cells across PDMS microchannels increased with channel width (for channels 3, 6 and 10 µm-wide) [55].

Given the results of the aforementioned studies, most of which were obtained for MDA-MB-231 cells as well, it would have been plausible to find a statistically significant difference between groups of nuclear migration periods for different constriction widths in the present work. An explanation for this not being the case could be, as mentioned above, the disparities among constriction widths for each type of constrictions and overlapping of constriction sizes for different categories. Additionally, as MDA-MB-231 cells are a highly invasive breast cancer cell line, it might be possible that the non-observation of an effect of constriction size in nuclear migration dynamics is a consequence of that property, making cells equally capable of traveling through constrictions of different sizes within the tested range. Importantly, it was verified that the measured constriction widths were larger than predicted, meaning that an effect of constriction size on the nuclear migration periods could have been seen if the constrictions were smaller to the point where transmigration dynamics would be affected, even for a highly invasive cell line.

Some authors also considered the effect of cell size or nuclear size in their confined cell migration studies [51, 89, 90]. Lautscham et al. (2015) found that smaller than average nuclei migrate faster through large and medium-sized constrictions, while no changes in nuclear velocity were found for the smallest channels. The authors found that the explanation for this phenomenon was the squeezing ratio of the nucleus, calculated as the cross section of the undeformed nucleus divided by the width of the constriction. Specifically, when the squeezing ratio of the nucleus exceeded 4, the migration velocity did not decrease further. As this is an interesting factor that could help interpret data from nuclear migration dynamics, this could be an aspect to consider for future work in the line of the present study.

5.3.2 Differences between nuclear migration periods

As demonstrated in the Results chapter (section 4.3), it was found that the means of the enter and exit periods were significantly different from one another for the 2 and 3 µm-wide constriction cell groups, suggesting that the exit period is shorter than the enter period for constrictions of smaller widths. On the other hand, it was shown that for the 5 µm-wide constriction cell groups these two periods did not seem to be, on average, significantly different. A way to interpret these findings is by having in mind that, the wider the constriction, the closer the conditions are to a 2D environment. Therefore, it might be logical that there are different mechanisms of nuclear compression and relaxation for narrower constrictions and not for wider constrictions, as the latter do not affect the entry and exit of the nucleus as much. Naturally, a 5 µm-wide constriction still places the cell under confinement, but it is not as pronounced as it is for the 2 and 3 µm-wide constrictions. Additionally, it was found that the 5 µm-wide constrictions are, in reality, about 7 µm-wide in average for cells whose nuclear migration periods were calculated, further contributing to the plausibility of this hypothesis.

Comparing the present findings with the literature, Lautscham et al. (2015) did not obtain similar results for MDA-MB-231 cells [51]. The authors found that the migration velocities of MDA cells were approximately similar for the three constriction regions that they defined, comparable to the enter, cross, and exit periods in this work. However, there are several studies with various cell types, including cancer cells, that refute these findings, being in line with the results obtained in the present study [32, 53, 70, 91]. Davidson et al. (2015) and Krause et al. (2019), for example, and although for different types of cells (NIH 3T3 fibroblasts and HT1080 cancer cells, respectively), found that, in nuclear migration through constrictions 2 µm-wide also divided into several periods, the speed of nuclear migration is significantly higher when the nucleus is exiting the constriction than when it is entering [53, 70]. Additionally, for Krause et al., this difference was not observed for 15 µm-wide constrictions, for which the speed of confined nuclear migration was approximately constant. Despite the differences between these studies and the present study, the results here obtained for the differences between the enter and exit periods might be validated by the literature.

Regarding the finding that the entry and exit periods are significantly different for cells migrating through 2 and 3 µm-wide constrictions, this could indicate that, as mentioned above, there are different mechanisms for nuclear compression and nuclear relaxation. In particular, the mechanisms that drive cell entry into the constriction seem to be more costly to the cell than those necessary for exiting the constriction, since the enter periods for these two constrictions groups were higher than the exit periods. When analyzing images of cell migration through the constrictions, it was observed that nuclear squeezing was necessary for the cell to pass the constriction, especially for narrower constrictions. Given that it was found that the enter period was higher than the exit period for these conditions, and since the enter period is the time it takes the nucleus to first enter the constriction, these results might be in line with the notion that the deformation of the nucleus is the rate-limiting step during confined migration (explored in subsection 2.1.3 of the Background chapter), as it was found in a variety of confined cell migration studies, not only for MBA-MB-231 cells [34, 35, 51], but also for a variety of other cell types [36, 53, 70, 92].

Two of the main aspects determining the ability of the nucleus to squeeze or deform are chromatin and the nuclear lamin network, as described in the Background chapter (subsection 2.1.3). Because nuclear squeezing or deformation is necessary for its entry into a constriction, chromatin condensation and Lamin A/C expression levels seem to be particularly relevant for nuclear compression in the enter period. Other explored mechanisms contributing to the entry of the nucleus into a constrictions, namely the pull and push mechanisms via de LINC complex for nucleus translocation across confined spaces, might also be important in the nuclear compression process for the enter period. Additionally, Mak et al. (2013) found that MDA cells migrated into constrictions in a rolling motion, which could possibly reduce the energy required to squeeze the nucleus [4]. The mechanisms here described might altogether contribute to the occurrence of a general, complex process that drives nucleus entry into confined spaces, which possibly differs from the mechanisms trough which cells exit confined spaces.

Concerning the exit period, Lautscham et al. (2015) found, with data gathered from several cell types, that cell nuclei migrate faster in the exit period when constriction width decreases [51]. The authors hypothesize that this phenomenon could be explained by a pulling forces mechanism that the cells employ more pronouncedly when passing through narrower constrictions due to increased friction, for compensation. Additionally, because these increased pulling forces lead to higher nuclear deformation, part of its energy may be stored elastically, which would then be rapidly released, thus explaining the quick exit of the nucleus out of the constriction [51]. This could then be a mechanism for fast nuclear exit from the constriction. Supporting these findings, Krause et al. (2019) have described the cyclic processes of confined nuclear migration and hypothesized that, during phase II (here enter period), when the nucleus acts as a physical barrier, there is an accumulation of deformation energy which is then released during phase IV (here exit period), aiding the cell to push through the constriction [53]. Combining, in a way, the several aforementioned mechanisms for nuclear compression and relaxation, Krause et al. also hypothesized that the nuclear deformation energy stored during accentuated confinement that is freed into nuclear rounding in phase IV of transmigration is proportional to chromatin condensation and Lamin A/C expression, which mediate nuclear elasticity [53]. These authors then suggest that chromatin condensation and Lamin A/C are also relevant for the nuclear migration dynamics at the exit of the constriction.

5.4 Role of Ctdnep1 and Eps8L2 in migration of MDA cells under confinement

Regarding the analysis of the role of Ctdnep1 and Eps8L2 in the migration of MDA cells under confinement, not enough quantification data of nuclear migration dynamics was obtained. Hence, it is not possible to establish reliable comparisons between the migration data from cells transfected with Eps8L2 or Ctdnep1 siRNAs with data from cells transfected with control siRNA. It can then be concluded that more data are needed in order to assess the importance of these proteins in MDA cell migration under confinement. Despite this, as mentioned in the Results chapter, one can observe in Figure 4.9 that, for 5 µm-wide constrictions, the means of the nuclear migration periods for cells transfected with Ctdnep1 siRNA are consistently higher than the values for the other conditions. Although there is no statistical significance for this comparison, this finding could hint at a possible role for this protein in the migration of MDA cells under confinement, given that, with its knockdown, the cells seem to have taken more time to migrate through the constrictions when comparing with the other conditions. Moreover, this observation can be, in part, backed up by the literature. In particular, Calero-Cuenca et al. (2021) reported a role for Ctdnep1 on nuclear positioning and cell migration in NIH 3T3 fibroblasts in a 2D setting [5]. It was found that Ctdnep1 knockdown using siRNA resulted in the inhibition of nuclear positioning away from the cell centroid and centrosome orientation, suggesting a role for Ctdnep1 in nuclear positioning. Since nuclear positioning is a key phenomenon during cell migration [17], this indicates that Ctdnep1 is involved in cell migration. Moreover, since the observation that MDA cells transfected with Ctdnep1 siRNA took longer to transmigrate than the other groups was for 5 µm-wide constrictions, which were, in reality, 7 µm-wide on average, it can be hypothesized that these cells were closer to a 2D environment that the cells migrating through narrower constrictions. Hence, these results seem to be backed up by the findings of Calero-Cuenca et al. (2021). However, more quantification data from confined nuclear migration would be necessary to make more robust and reliable comparisons with the literature.

5.5 Performance of NanoJ-Fluidics in correlative microscopy

Using NanoJ-Fluidics, it was possible to accurately correlate live and fixed-cell imaging to observe the details of certain cell structures, namely the nucleus, actin filaments and focal adhesions (from vinculin staining), in cells with different types of dynamics. Notably, the visualization and acquisition of images of the exact same cells during live and fixed imaging was achieved in a convenient manner, with minor effort. If the cell staining had been performed manually, it would have been significantly more difficult to achieve the same results, given that it would be necessary to remove the sample from the microscope stage after live imaging and later place the sample back under the microscope after the staining procedure. This would then require the exhausting task of finding the same cells in the microscope field of view for fixed-cell imaging. Moreover, the reliability provided by automatic performance of the staining procedure using the NanoJ-Fluidics software allowed to overcome some issues of non-automated approaches, such as their time consuming nature and possible lack of standardization.

A notable aspect that was possible to observe in cells using correlative microscopy was the presence of structural differences in actin filaments and focal adhesions of cells exhibiting different dynamics during time-lapse acquisitions. Specifically, cells that appeared to remain static throughout the time-lapse exhibited a high quantity of actin stress fibers with focal adhesions localized in their extremities, whereas cells that showed a more dynamic behavior did not have these structures, exhibiting shorter and less defined actin filaments and less localized vinculin (see Figures 4.10 and 4.11 in section 4.5). It is then hypothesized that the analyzed ”static” cell was, during the time-lapse acquisition, employing a mesenchymal mode of migration, while the ”dynamic” cell was employing an amoeboid mode of migration. This association seems plausible due to the fact that, when employing a mesenchymal mode of migration, cells exhibit actin-rich protrusions and are strongly adherent to the ECM via mature focal adhesions, which are localized in the extremities of stress fibers, contributing to a slow migration speed [93]. This is exactly what is seen in the cell from Figure 4.10. Moreover, the actin-rich protrusion exhibited by the analyzed ”static” cell seems to be lamellipodia, as they have flat appearance as opposed to thin, elongated filopodia. The fact that this cell, claimed to be employing a mesenchymal mode of migration, seemed to be static throughout the 30 minute-long time-lapse, might be due to the fact that the live-cell acquisition was not long enough capture cell displacement in this rather slow mode of migration. Additionally, it can be seen in Figure 4.10 that the analyzed cell is adherent to a neighboring cell, which might also impact its migration dynamics. Regarding the ”dynamic” cell, its association with an amoeboid mode of migration seems logical as cells migrating in this manner exhibit a more rounded shape, absence of stress fibers and mature focal adhesions, and fast migration dynamics in comparison to the mesenchymal mode of migration, which is precisely what can be seen in Figure 4.11. Furthermore, regarding the type of amoeboid migration that this cell seems to be employing, actin-driven protrusions, namely pseudopods, are observed rather than blebs characteristic of contraction-based migration, in addition to the fact that the cell does not seem to contract throughout the time-lapse acquisition. This then suggests that this more dynamic cell was employing an amoeboid migration driven by the formation of pseudopods.

Furthermore, super-resolution images were produced using SRRF in order to assess if it was possible to visualize structural information of fixed cells with more resolution that than of widefield fluorescence imaging with the images obtained with NanoJ-Fluidics. It was observed that the generated SRRF images indeed allowed a sharper visualization of focal adhesions (vinculin) and, more notably, actin filaments in comparison to widefield fluorescence images. As for the analyzed ”static” cell, Figure 4.12 in section 4.6 shows that the SRRF images are able to provide with more accuracy the source of the fluorescence signal than the widefield fluorescence images. This can be inferred upon analysis of the pixel intensity profiles from the same actin filaments in both images. For the case of the selected pixels indicated by a yellow line, it can be observed that, while the intensity profile of those pixels in the widefield fluorescence image for a single actin fiber takes the form of a wide spread peak, the corresponding intensity profile from the SRRF image shows a narrower, well-defined peak, corresponding to a single actin filament.

Similarly, for the case of the selected pixels indicated by a blue line, it is observed that the intensity profile of those pixels in the SRRF images shows two narrow distinct peaks, corresponding to two actin filaments, while the intensity profile of the pixels in the same region of the widefield fluorescence image shows a much wider intensity profile where, simply by observing it, two peaks corresponding to two actin filaments can barely be distinguished. Similar results were obtained by the authors who developed this super-resolution approach [69]. Additionally, when observing the widefield and super-resolution images from the stained structures of the analyzed ”dynamic” cell (see Figure 4.13 from section 4.6), it was possible to notice an apparent increase in resolution of the actin filaments in the SRRF image in comparison to its corresponding widefield fluorescence image, despite the absence of long, well-defined stress fibers that are seen in the analyzed ”static” cell. In particular, it is seen in Figure 4.13B that, in the selected region of the cell, the SRRF image is able to provide a visualization of the actin filaments with more detail, allowing the distinguishment of small, individual filaments with more accuracy than that provided by the widefield fluorescence image.

These findings show how SRRF can allow a sharper visualization of stained cell structures, with special emphasis on the actin filaments, in this case, in comparison to widefield fluorescence microscopy, even with standard microscopy equipment. However, even better SRRF images could have been possibly obtained if a different system had been used instead. This is because it is known that the resolution improvement provided by super-resolution imaging techniques such as SRRF depends on the photon yield, camera detector sensitivity, and resolving power of the equipment [94]. In particular, when observing the SRRF image that was generated from the fluorescence images of the vinculin staining in the analyzed ”static” cell (see Figure 4.12A from section 4.6), it can be noticed that the reconstructed image picked up a significant amount of noise which was not as visible in the corresponding widefield fluorescence image. This could be due to a decreased signal intensity from the red fluorophores in comparison to the green fluorophores in the actin staining, or could be due to unspecific binding of antibodies to the dish that were not properly washed off. Nevertheless, perhaps images with a better signal-to-noise ratio could have been obtained with improved equipment. Despite this, it is still possible to see clearly the higher-intensity pixels defining the focal adhesions structures from the vinculin staining signal, which showcases the powerful capacity for SRRF to generate super-resolution images even when the fluorescence signal is possibly low.

In conclusion, using NanoJ-Fluidics to perform correlative microscopy was particularly advantageous in this work, having even been possible to correlate super-resolution images of structural information of the cell with its dynamics observable in live imaging. This technique shows high potential for the study of cell migration, in particular cancer cell migration, allowing the direct correlation of its dynamics with cellular structures. Moreover, it is possible to go even further with NanoJ-Fluidics and also use SRRF for the study of this subject. For example, while the correlative microscopy procedures that were carried out in this work required manual initiation of the staining protocol for fixed-cell imaging and in no particular time point of interest in cell dynamics, unsupervised live-to-fixed microscopy could be used to automatically trigger cell fixation and subsequent staining procedure once a certain morphological cue was detected by specialized software [6]. This would allow the visualization of structural information in the cell exactly during an event of interest. Regarding the generation of super-resolution images using SRRF, this can be performed not only using fluorescence images from fixed cells, but also with fluorescence images acquired throughout various time points in live imaging, in case the cells have certain structures marked with fluorescent proteins [69]. Therefore, it could be possible to analyze selected cell structures at super resolution not only after the cells are fixed, but also during live imaging, posing a major advantage in the study of cell migration.

Chapter 6

Conclusions

6.1 Achievements

With this work, it was possible to study cancer cell migration under confinement, as well as successfully implement a correlative microscopy workflow for the correlation of cell dynamics with its underlying structural information. Regarding experiments with MDA-MB-231 cells in PDMS migration devices, we could replicate the cell, and, more pronouncedly, nuclear squeezing behavior that is typically observed in cells migrating across narrow spaces. Moreover, we found that the enter period of nuclear transmigration was, on average, higher than the exit period for cells migrating across 2 and 3 µm-wide constrictions, which was not verified for 5 µm-wide constrictions. Together with the important observation that the nucleus is the rate-limiting step during confined migration, these results are in line with a wide variety of similar studies performed by other authors, possibly validating our findings. Additionally, we established an association between the differences observed in the enter and exit nuclear migration periods and possible different mechanisms employed by the cell for these two distinct phases in migration across microconstrictions.

Moreover, we assembled a novel system in the lab, the NanoJ-Fluidics framework, for the performance of correlative microsocopy. This system showed to be a powerful tool for bridging the gap in the complex task of performing live and fixed imaging on the same cells. Particularly, we were able to image live cells through a time-lapse acquisition, fix the cells right after, initiate an automatic staining protocol directly on the microscope stage, and image the stained cell structures with fluorescence microscopy, without losing the cell positions initially defined in the imaging software. Additionally, NanoJ-Fluidics showed to be reliant and effective in the cell staining procedures, with good-quality fluorescence images having been obtained for all stained structures, namely focal adhesions via vinculin, actin filaments via phalloidin and the nucleus via DAPI. It was then possible to visualize how cellular elements such as actin and vinculin were arranged in the cell to drive different types of cell migration, namely mesenchymal with lamellipodia and amoeboid with pseudopods, as validated by the literature. Lastly, we were able to generate SRRF images with the acquisition of fluorescence images from vinculin and actin stainings, and observed that they were able to provide with more accuracy the fluorophore signal source in comparison to the widefield fluorescence images. These findings indicate that the established correlative microscopy set-up allowed the production of super-resolution images, further showcasing the applicability and usefulness of the NanoJ-Fluidics system.

Bearing in mind the presented achievements of the present work, it can be concluded that it was possible to explore different workflows for the study of cancer cell migration, with different strong assets concerning the nature of their achievable findings. On one hand, studying confined cancer cell migration using microfabricated PDMS devices can allow for a better understanding of the mechanisms involved in events required for migration in tight, complex 3D environments, such as nuclear squeezing, although imaging of cellular structures in detail can be limited. On another hand, using correlative microscopy to associate intracellular structural information with the exhibited cell dynamics provides a better understanding of the mechanisms driving certain phenomena in cell migration, although studies in two-dimensions are not as physiologically relevant as in three-dimensions. However, if brought together somehow, these two workflows could provide one common set of enhanced findings, although that was not possible to accomplish in the present work.

6.2 Limitations and Future Work

There are several approaches that could be considered to conduct future work in the lines of the present study. Firstly, one can address limitations of this work that could be overcome, as well as improvements on certain steps of the implemented methodology that could lead to better outcomes.

It was observed that the shape and size of the micropillars in the migration devices were not according to what was expected, namely a round shape and same size for constrictions belonging to the same width category. In future studies, the quality of the molds for the devices could be checked periodically to guarantee that its structures are not deformed, thus preventing the fabrication of devices with irregular micropillars. Additionally, the design for the mold could account for the PDMS shrinkage effect and the curing conditions could be better controlled, in order to ensure regular and correctly-sized microconstrictions. By employing these strategies, more accurate results for the quantification of nuclear transmigration dynamics could be obtained.

One of the objectives of this work, namely assessing the role of Ctdnep1 and Eps8L2 in confined cell migration, was not achieved. Hence, further studies can again include the knockdown of these proteins in an attempt to obtain more quantification data of nuclear migration dynamics, in order to understand the role of these proteins in cell migration in this setting. Similarly, since it was not possible to obtain results for actin filaments dynamics in confined migration, further work can include the study of actin behavior in this context. Additionally, the role of Ctdnep1 and Eps8L2 in actin dynamics during confined migration could be investigated.

A limitation of this work could be the fact that only one cell line was analyzed in confined cell migration studies. In the context of breast cancer, the findings obtained for MDA-MB-231 cells may not be the same as for other types of breast cancer cells. Additionally, it is important to compare the results obtained for cancer cells with healthy cells. With these observations in mind, future work could include the use of not only other types of breast cancer cells, but also the use of healthy cells for comparison, in order to have a better notion of the context of the obtained results.

Another aspect that could be raised as a limitation of this work is the fact that the system used for confined cancer cell migration studies is not physiologically accurate. For example, PDMS is stiffer than tissues encountered by cancer cells *in vivo*, and this system did not contemplate any other cell types that can be naturally present in environments where cancer cells are found, thus possibly leading to different results. In this regard, future work could include a study of confined cell migration comprising other cell types, for example endothelial cells to recreate cancer cell intravasation and extravasation in blood vessels, and the microdevices could include an ECM membrane to mimic the microarchitecture of *in vivo* tissues.

Finally, as briefly mentioned above, one could combine the two distinct workflows carried out in this study for future work. In particular, the study of cancer cell migration under confinement could be performed using the same microfabricated devices, but integrated in a correlative microscopy framework with the use of NanoJ-Fluidics. This would involve the connection of the two systems through appropriate microfluidic design, thereby allowing the delivery and removal of fluids via tubing to the PDMS devices. With such a set-up, it could be possible to perform a time-lapse acquisition of cells migrating through the constrictions, followed by a staining procedure carried out with NanoJ-Fluidics directly on the microscope stage, for the acquisition of fluorescence images. If stained for the Ctdnep1 and Eps8L2 proteins, assuming the availability of the necessary antibodies, it would even be possible to analyze with detail the location of these proteins during, for example, nuclear squeezing, presenting a major improvement on the current line of work. Additionally, if relevant, SRRF imaging could also be performed, further expanding the possibilities of findings obtained with such framework. Moreover, cell fixation in this context could be automatically triggered by a certain morphological cue, such as nuclear shape during migration across microconstrictions, thus taking full advantage of the potentialities of NanoJ-Fluidics.

In conclusion, and considering the possible future work here discussed, there is a variety of approaches that can be employed for the study of cancer cell migration, namely in complex 3D environments. The platforms and workflows here presented for the study of cancer cell migration can contribute to a better understanding of the phenomena involved in cancer cell migration for metastization as well as other clinically relevant phenomena, not being restricted to cancer. The work here developed can then pave the way for studies with higher clinical relevance, namely drug development and investigation of preventive measures for metastasis formation, thus contributing to an amelioration of the current cancer paradigm that is felt worldwide.

Bibliography

[1] N. Pasha and N. C. Turner. Understanding and overcoming tumor heterogeneity in metastatic breast cancer treatment. *Nature Cancer*, 2:680–692, 2021. doi: 10.1038/s43018-021-00229-1.

[2] WHO. Cancer, 2021. URL `https://www.who.int/en/news-room/fact-sheets/detail/cancer`. Online; accessed October 2021.

[3] Y.-H. V. Ma, K. Middleton, and L. You. A review of microfluidic approaches for investigating cancer extravasation during metastasis. *Microsystems & Nanoengineering*, 4:17104, 2018. doi: 10.1038/micronano.2017.104.

[4] M. Mak, C. Reinhart-King, and D. Erickson. Elucidating mechanical transition effects of invading cancer cells with a subnucleus-scaled microfluidic serial dimensional modulation device. *Lab on a chip*, 13(3):340–348, 2013. doi: 10.1039/c2lc41117b.

[5] F. J. Calero-Cuenca, D. S. Osorio, S. Carvalho-Marques, S. C. Sridhara, L. M. Oliveira, Y. Jiao, J. Diaz, C. S. Janota, B. Cadot, and E. R. Gomes. Ctdnep1 and Eps8L2 regulate dorsal actin cables for nuclear positioning during cell migration. *Current Biology*, 31(7):1521–1530.e8, 2021. doi: 10.1016/j.cub.2021.01.007.

[6] P. Almada, P. Pereira, S. Culley, G. Caillol, F. Boroni-Rueda, C. Dix, G. Charras, B. Baum, R. Laine, C. Leterrier, and R. Henriques. Automating multimodal microscopy with NanoJ-Fluidics. *Nature Communications*, 10(1):1223, 2019. doi: 10.1038/s41467-019-09231-9.

[7] I. J. Fidler. The pathogenesis of cancer metastasis: the 'seed and soil' hypothesis revisited. *Nature Reviews Cancer*, 3(6):453—458, 2003. doi: 10.1038/nrc1098.

[8] C. Paul, P. Mistriotis, and K. Konstantopoulos. Cancer cell motility: lessons from migration in confined spaces. *Nature Reviews Cancer*, 17:131–140, 2016. doi: 10.1038/nrc.2016.123.

[9] S. Seetharaman and S. Etienne-Manneville. Cytoskeletal Crosstalk in Cell Migration. *Trends in Cell Biology*, 30(9):720–735, 2020. doi: 10.1016/j.tcb.2020.06.004.

[10] V. te Boekhorst, L. Preziosi, and P. Friedl. Plasticity of Cell Migration In Vivo and In Silico. *Annual Review of Cell and Developmental Biology*, 32(1):491–526, 2016. doi: 10.1146/annurev-cellbio-111315-125201.

[11] D. G. Blackley, J. H. Cooper, P. Pokorska, and A. Ratheesh. Mechanics of developmental migration. *Seminars in Cell & Developmental Biology*, 2021. ISSN 1084-9521. doi: 10.1016/j.semcdb.2021.07.002.

[12] P. O'Neill, J. Castillo-Badillo, X. Meshik, V. Kalyanaraman, K. Melgarejo, and N. Gautam. Membrane Flow Drives an Adhesion-Independent Amoeboid Cell Migration Mode. *Developmental Cell*, 46(1):9–22.e4, 2018. doi: 10.1016/j.devcel.2018.05.029.

[13] B. Alvarez-González, R. Me, R. Firtel, E. Bastounis, J. C. Del Alamo, and J. Lasheras. Cytoskeletal Mechanics Regulating Amoeboid Cell Locomotion. *Applied mechanics reviews*, 66(5):0508041–05080414, 2014. doi: 10.1115/1.4026249.

[14] J. C. Meiring, B. I. Shneyer, and A. Akhmanova. Generation and regulation of microtubule network asymmetry to drive cell polarity. *Current Opinion in Cell Biology*, 62:86–95, 2020. doi: 10.1016/j.ceb.2019.10.004.

[15] K. Yamada and M. Sixt. Mechanisms of 3D cell migration. *Nature Reviews Molecular Cell Biology*, 20(12):1–15, 2019. doi: 10.1038/s41580-019-0172-9.

[16] N. Ecker and K. Kruse. Excitable actin dynamics and amoeboid cell migration. *PLOS ONE*, 16(2):1–22, 2021. doi: 10.1371/journal.pone.0246311.

[17] F. J. Calero-Cuenca, C. S. Janota, and E. R. Gomes. Dealing with the nucleus during cell migration. *Current Opinion in Cell Biology*, 50:35–41, 2018. doi: 10.1016/j.ceb.2018.01.014.

[18] E. R. Gomes, S. Jani, and G. G. Gundersen. Nuclear Movement Regulated by Cdc42, MRCK, Myosin, and Actin Flow Establishes MTOC Polarization in Migrating Cells. *Cell*, 121(3):451–463, 2005. doi: https://doi.org/10.1016/j.cell.2005.02.022.

[19] C. S. Janota, F. J. Calero-Cuenca, J. Costa, and E. R. Gomes. SnapShot: Nucleo-cytoskeletal Interactions. *Cell*, 169(5):970—970.e1, 2017. doi: 10.1016/j.cell.2017.05.014.

[20] G. W. G. Luxton, E. R. Gomes, E. S. Folker, E. Vintinner, and G. G. Gundersen. Linear Arrays of Nuclear Envelope Proteins Harness Retrograde Actin Flow for Nuclear Movement. *Science*, 329(5994):956–959, 2010. doi: 10.1126/science.1189072.

[21] R. de Leeuw, Y. Gruenbaum, and O. Medalia. Nuclear Lamins: Thin Filaments with Major Functions. *Trends in Cell Biology*, 28(1):34–45, 2018. doi: 10.1016/j.tcb.2017.08.004.

[22] J. Wu, I. Kent, N. Shekhar, T. Chancellor, A. Mendonca, R. Dickinson, and T. Lele. Actomyosin Pulls to Advance the Nucleus in a Migrating Tissue Cell. *Biophysical Journal*, 106(1):7–15, 2014. doi: 10.1016/j.bpj.2013.11.4489.

[23] M. L. Suvà and D. N. Louis. Next-generation molecular genetics of brain tumours. *Current Opinion in Neurology*, 26(6):681–687, 2013. doi: 10.1097/WCO.0000000000000027.

[24] Y. Kim, M. S. Gentry, T. E. Harris, S. E. Wiley, J. C. Lawrence, and J. E. Dixon. A conserved phosphatase cascade that regulates nuclear membrane biogenesis. *Proceedings of the National Academy of Sciences*, 104(16):6596–6601, 2007. doi: 10.1073/pnas.0702099104.

[25] R. Satow, T. chuan Chan, and M. Asashima. Molecular cloning and characterization of dullard: a novel gene required for neural development. *Biochemical and Biophysical Research Communications*, 295(1):85–91, 2002. doi: 10.1016/S0006-291X(02)00641-1.

[26] J. Lee, K. McKinney, A. Pavlopoulos, M. Niu, J. Kang, J. Oh, K. p. kim, and S. Hwang. Altered Proteome of Extracellular Vesicles Derived from Bladder Cancer Patients Urine. *Molecules and cells*, 41(3):179–187, 2018. doi: 10.14348/molcells.2018.2110.

[27] M. Hertzog, F. Milanesi, L. Hazelwood, A. Disanza, H. Liu, E. Perlade, M. G. Malabarba, S. Pasqualato, A. Maiolica, S. Confalonieri, C. Le Clainche, N. Offenhauser, J. Block, K. Rottner, P. P. Di Fiore, M.-F. Carlier, N. Volkmann, D. Hanein, and G. Scita. Molecular Basis for the Dual Function of Eps8 on Actin Dynamics: Bundling and Capping. *PLOS Biology*, 8(6):1–23, 2010. doi: 10.1371/journal.pbio.1000387.

[28] N. Offenhäuser, A. Borgonovo, A. Disanza, P. Romano, I. Ponzanelli, G. Iannolo, P. P. Di Fiore, and G. Scita. The eps8 Family of Proteins Links Growth Factor Stimulation to Actin Reorganization Generating Functional Redundancy in the Ras/Rac Pathway. *Molecular Biology of the Cell*, 15(1): 91–98, 2004. doi: 10.1091/mbc.e03-06-0427.

[29] A. Di Meo, I. Batruch, M. D. Brown, C. Yang, A. Finelli, M. A. Jewett, E. P. Diamandis, and G. M. Yousef. Searching for prognostic biomarkers for small renal masses in the urinary proteome. *International Journal of Cancer*, 146(8):2315–2325, 2020. doi: 10.1002/ijc.32650.

[30] E. Colas, C. Perez, S. Cabrera, N. Pedrola, M. Monge, J. Castellvi, F. Eyzaguirre, J. Gregorio, A. Ruiz, M. Llaurado, M. Rigau, M. Garcia, T. Ertekin, M. Montes, R. Lopez-Lopez, R. Carreras, J. Xercavins, A. Ortega, T. Maes, E. Rosell, A. Doll, M. Abal, J. Reventos, and A. Gil-Moreno. Molecular markers of endometrial carcinoma detected in uterine aspirates. *International Journal of Cancer*, 129(10):2435–2444, 2011. doi: 10.1002/ijc.25901.

[31] J. Yao, S. Weremowicz, B. Feng, R. C. Gentleman, J. R. Marks, R. Gelman, C. Brennan, and K. Polyak. Combined cdna array comparative genomic hybridization and serial analysis of gene expression analysis of breast tumor progression. *Cancer Research*, 66(8):4065–4078, 2006. doi: 10.1158/0008-5472.CAN-05-4083.

[32] A. L. McGregor, C.-R. Hsia, and J. Lammerding. Squish and squeeze—the nucleus as a physical barrier during migration in confined environments. *Current Opinion in Cell Biology*, 40:32–40, 2016. doi: 10.1016/j.ceb.2016.01.011.

[33] L. Liu, Q. Luo, J. Sun, and G. Song. Nucleus and nucleus-cytoskeleton connections in 3D cell migration. *Experimental Cell Research*, 348(1):56–65, 2016. doi: 10.1016/j.yexcr.2016.09.001.

[34] Y. Fu, L. K. Chin, T. Bourouina, A. Liu, and A. Vandongen. Nuclear deformation during breast cancer cell transmigration. *Lab on a chip*, 12:3774–8, 2012. doi: 10.1039/c2lc40477j.

[35] K. Wolf, M. te Lindert, M. Krause, S. Alexander, J. te Riet, A. L. Willis, R. M. Hoffman, C. G. Figdor, S. J. Weiss, and P. Friedl. Physical limits of cell migration: Control by ECM space and nuclear deformation and tuning by proteolysis and traction force. *Journal of Cell Biology*, 201(7): 1069–1084, 2013. doi: 10.1083/jcb.201210152.

[36] P. Davidson, C. Denais, M. Bakshi, and J. Lammerding. Nuclear deformability constitutes a rate-limiting step during cell migration in 3-D environments. *Cellular and Molecular Bioengineering*, 7 (3):293–306, 2014. doi: 10.1007/s12195-014-0342-y.

[37] M. Doolin, R. Moriarty, and K. Stroka. Mechanosensing of Mechanical Confinement by Mesenchymal-Like Cells. *Frontiers in physiology*, 11:365, 2020. doi: 10.3389/fphys.2020.00365.

[38] X. Cao, E. Moeendarbary, P. Isermann, P. Davidson, X. Wang, M. Chen, A. Roberts, J. Lammerding, R. Kamm, and V. B. Shenoy. A Chemomechanical Model for Nuclear Morphology and Stresses during Cell Transendothelial Migration. *Biophysical Journal*, 111(7):1541–52, 2016. doi: 10.1016/j.bpj.2016.08.011.

[39] T. Harada, J. Swift, J. Irianto, J.-W. Shin, K. R. Spinler, A. Athirasala, R. Diegmiller, P. D. P. Dingal, I. L. Ivanovska, and D. E. Discher. Nuclear lamin stiffness is a barrier to 3D migration, but softness can limit survival. *Journal of Cell Biology*, 204(5):669–682, 2014. doi: 10.1083/jcb.201308029.

[40] R. Petrie, H. Koo, and K. Yamada. Generation of Compartmentalized Pressure by a Nuclear Piston Governs Cell Motility in 3D Matrix. *Science*, 345(6200):1062–5, 2014. doi: 10.1126/science.1256965.

[41] D. G. Thomas, A. Yenepalli, C. M. Denais, A. Rape, J. R. Beach, Y.-l. Wang, W. P. Schiemann, H. Baskaran, J. Lammerding, and T. T. Egelhoff. Non-muscle myosin IIB is critical for nuclear translocation during 3D invasion. *Journal of Cell Biology*, 210(4):583–594, 2015. doi: 10.1083/jcb.201502039.

[42] C. M. Denais, R. M. Gilbert, P. Isermann, A. L. McGregor, M. te Lindert, B. Weigelin, P. M. Davidson, P. Friedl, K. Wolf, and J. Lammerding. Nuclear envelope rupture and repair during cancer cell migration. *Science*, 352(6283):353–358, 2016. doi: 10.1126/science.aad7297.

[43] J. Irianto, Y. Xia, C. R. Pfeifer, A. Athirasala, J. Ji, C. Alvey, M. Tewari, R. R. Bennett, S. M. Harding, A. J. Liu, R. A. Greenberg, and D. E. Discher. DNA Damage Follows Repair Factor Depletion and Portends Genome Variation in Cancer Cells after Pore Migration. *Current Biology*, 27(2):210–223, 2017. doi: 10.1016/j.cub.2016.11.049.

[44] S. SenGupta, C. Parent, and J. Bear. The principles of directed cell migration. *Nature Reviews Molecular Cell Biology*, 22(8):529–547, 2021. doi: 10.1038/s41580-021-00366-6.

[45] C. Capo-Chichi, K. Cai, J. Smedberg, P. Ganjei-Azar, A. Godwin, and X.-X. Xu. Loss of A-type lamin expression compromises nuclear envelope integrity in breast cancer. *Chinese journal of cancer*, 30 (6):415–25, 2011. doi: 10.5732/cjc.010.10566.

[46] M. Mak, C. A. Reinhart-King, and D. Erickson. Microfabricated Physical Spatial Gradients for Investigating Cell Migration and Invasion Dynamics. *PLOS ONE*, 6(6):1–8, 2011. doi: 10.1371/journal.pone.0020825.

[47] R. Chiotaki, H. Polioudaki, and P. A. Theodoropoulos. Differential nuclear shape dynamics of invasive andnon-invasive breast cancer cells are associated with actin cytoskeleton organization and stability. *Biochemistry and Cell Biology*, 92(4):287–295, 2014. doi: 10.1139/bcb-2013-0120.

[48] N. Zuela-Sopilniak and J. Lammerding. Engineering approaches to studying cancer cell migration in three-dimensional environments. *Philosophical Transactions of the Royal Society B: Biological Sciences*, 374(1779):20180219, 2019. doi: 10.1098/rstb.2018.0219.

[49] C. D. Paul, W.-C. Hung, D. Wirtz, and K. Konstantopoulos. Engineered Models of Confined Cell Migration. *Annual Review of Biomedical Engineering*, 18(1):159–180, 2016. doi: 10.1146/annurev-bioeng-071114-040654.

[50] J. Tien, U. Ghani, Y. Dance, A. Seibel, M. a. Karakan, K. Ekinci, and C. Nelson. Matrix Pore Size Governs Escape of Human Breast Cancer Cells from a Microtumor to an Empty Cavity. *iScience*, 23(11):101673, 2020. doi: 10.1016/j.isci.2020.101673.

[51] L. Lautscham, C. Kämmerer, J. Lange, T. Kolb, C. Mark, A. Schilling, P. Strissel, R. Strick, C. Gluth, A. Rowat, C. Metzner, and B. Fabry. Migration in Confined 3D Environments Is Determined by a Combination of Adhesiveness, Nuclear Volume, Contractility, and Cell Stiffness. *Biophysical Journal*, 109:900–13, 2015. doi: 10.1016/j.bpj.2015.07.025.

[52] D. Irimia and M. Toner. Spontaneous migration of cancer cells under conditions of mechanical confinement. *Integrative biology: quantitative biosciences from nano to macro*, 1(8-9):506–12, 2009. doi: 10.1039/b908595e.

[53] M. Krause, F. W. Yang, M. te Lindert, P. Isermann, J. Schepens, R. J. A. Maas, C. Venkataraman, J. Lammerding, A. Madzvamuse, W. Hendriks, J. te Riet, and K. Wolf. Cell migration through three-dimensional confining pores: speed accelerations by deformation and recoil of the nucleus. *Philosophical Transactions of the Royal Society B: Biological Sciences*, 374(1779):20180225, 2019. doi: 10.1098/rstb.2018.0225.

[54] M. Zanotelli, A. Rahman, J. Vanderburgh, P. Taufalele, A. Jain, D. Erickson, F. Bordeleau, and C. Reinhart-King. Energetic costs regulated by cell mechanics and confinement are predictive of migration path during decision-making. *Nature Communications*, 10(1):1–12, 2019. doi: 10.1038/s41467-019-12155-z.

[55] Z. Tong, E. M. Balzer, M. R. Dallas, W.-C. Hung, K. J. Stebe, and K. Konstantopoulos. Chemotaxis of Cell Populations through Confined Spaces at Single-Cell Resolution. *PLOS ONE*, 7(1):1–10, 2012. doi: 10.1371/journal.pone.0029211.

[56] W. Kuang, Q. Deng, C. Deng, W. Li, S.-W. Shu, and M. rong Zhou. Hepatocyte growth factor induces breast cancer cell invasion via the PI3K/Akt and p38 MAPK signaling pathways to up-regulate the expression of COX2. *American journal of translational research*, 9(8):3816–3826, 2017.

[57] L. Tweedy, P. A. Thomason, P. I. Paschke, K. Martin, L. M. Machesky, M. Zagnoni, and R. H. Insall. Seeing around corners: Cells solve mazes and respond at a distance using attractant breakdown. *Science*, 369(6507):eaay9792, 2020. doi: 10.1126/science.aay9792.

[58] Y.-J. Huang, J. Samorajski, R. Kreimer, and P. C. Searson. The Influence of Electric Field and Confinement on Cell Motility. *PLOS ONE*, 8(3):1–10, 2013. doi: 10.1371/journal.pone.0059447.

[59] M. Mak and D. Erickson. Mechanical decision trees for investigating and modulating single-cell cancer invasion dynamics. *Lab Chip*, 14(5):964–971, 2014. doi: 10.1039/C3LC51173A.

[60] Y. Choi, E. Hyun, J. Seo, C. Blundell, H. C. Kim, E. Lee, S. H. Lee, A. Moon, W. K. Moon, and D. Huh. A microengineered pathophysiological model of early-stage breast cancer. *Lab on a chip*, 15(16):3350–7, 2015. doi: 10.1039/c5lc00514k.

[61] D. E. Ingber. Reverse Engineering Human Pathophysiology with Organs-on-Chips. *Cell*, 164(6): 1105–9, 2016. doi: 10.1016/j.cell.2016.02.049.

[62] S. Knowlton, S. Onal, C. H. Yu, J. J. Zhao, and S. Tasoglu. Bioprinting for cancer research. *Trends in Biotechnology*, 33(9):504–513, 2015. doi: 10.1016/j.tibtech.2015.06.007.

[63] Y. Zhao, R. Yao, L. Ouyang, H. Ding, T. Zhang, K. Zhang, S. Cheng, and W. Sun. Three-dimensional printing of Hela cells for cervical tumor model in vitro. *Biofabrication*, 6(3):035001, 2014. doi: 10.1088/1758-5082/6/3/035001.

[64] T. Huang, X. Qu, J. Liu, and S. Chen. 3d printing of biomimetic microstructures for cancer cell migration. *Biomedical microdevices*, 16(1):127–132, 2014. doi: 10.1007/s10544-013-9812-6.

[65] M. Hauser, M. Wojcik, D. Kim, M. Mahmoudi, W. Li, and K. Xu. Correlative Super-Resolution Microscopy: New Dimensions and New Opportunities. *Chemical Reviews*, 117(11):7428–7456, 2017. doi: 10.1021/acs.chemrev.6b00604.

[66] M. A. Karreman, L. Mercier, N. L. Schieber, G. Solecki, G. Allio, F. Winkler, B. Ruthensteiner, J. G. Goetz, and Y. Schwab. Fast and precise targeting of single tumor cells in vivo by multimodal correlative microscopy. *Journal of Cell Science*, 129(2):444–456, 2016. doi: 10.1242/jcs.181842.

[67] C. C. Moura, A. Miranda, R. O. Oreffo, and P. A. De Beule. Correlative fluorescence and atomic force microscopy to advance the bio-physical characterisation of co-culture of living cells. *Biochemical and Biophysical Research Communications*, 529(2):392–7, 2020. doi: 10.1016/j.bbrc.2020.06.037.

[68] L. Schermelleh, A. Ferrand, T. Huser, C. Eggeling, M. Sauer, O. Biehlmaier, and G. P. C. Drummen. Super-resolution microscopy demystified. *Nature Cell Biology*, 21:72–84, 2019. doi: 10.1038/s41556-018-0251-8.

[69] N. Gustafsson, S. Culley, G. Ashdown, D. Owen, P. Pereira, and R. Henriques. Fast live-cell conventional fluorophore nanoscopy with ImageJ through super-resolution radial fluctuations. *Nature Communications*, 7(1):12471, 2016. doi: 10.1038/ncomms12471.

[70] P. M. Davidson, J. Sliz, P. Isermann, C. Denais, and J. Lammerding. Design of a microfluidic device to quantify dynamic intra-nuclear deformation during cell migration through confining environments. *Integrative Biology*, 7(12):1534–1546, 2015. doi: 10.1039/c5ib00200a.

[71] NanoJ-Fluidics: open-source fluid exchange in microscopy, 2019. URL `https://github.com/HenriquesLab/NanoJ-Fluidics/wiki`. Online; accessed October 2021.

[72] Eight multiplexed pumps.lxf, 2018. URL `https://bit.ly/3lKuRBP`. Online; accessed October 2021.

[73] MMeyer_SolidPumpy_2_5.stl, 2019. URL `https://bit.ly/3BIOcuo`. Online; accessed October 2021.

[74] MMeyer_Pumpy_BD60ml_2_5.stl, 2019. URL `https://bit.ly/3BJadHT`. Online; accessed October 2021.

[75] MMeyer_Pumpy_BD3ml_2_5.stl, 2019. URL `https://bit.ly/3lFdIt8`. Online; accessed October 2021.

[76] Electronics Firmware, 2018. URL `https://bit.ly/3DX8QG7`. Online; accessed October 2021.

[77] GUI Install, 2018. URL `https://bit.ly/3aR7Gj4`. Online; accessed October 2021.

[78] S. Alexander, G. E. Koehl, M. Hirschberg, E. K. Geissler, and P. Friedl. Dynamic imaging of cancer growth and invasion: a modified skin-fold chamber model. *Histochemistry and cell biology*, 130(6):1147–54, 2008. doi: 10.1007/s00418-008-0529-1.

[79] K. Yamauchi, M. Yang, P. Jiang, M. Xu, N. Yamamoto, H. Tsuchiya, K. Tomita, A. R. Moossa, M. Bouvet, and R. M. Hoffman. Development of Real-time Subcellular Dynamic Multicolor Imaging of Cancer-Cell Trafficking in Live Mice with a Variable-Magnification Whole-Mouse Imaging System. *Cancer Research*, 66(8):4208–14, 2006. doi: 10.1158/0008-5472.CAN-05-3927.

[80] m.-B. Voisin, A. Woodfin, and S. Nourshargh. Monocytes and Neutrophils Exhibit Both Distinct and Common Mechanisms in Penetrating the Vascular Basement Membrane In Vivo. *Arteriosclerosis, thrombosis, and vascular biology*, 29(8):1193–9, 2009. doi: 10.1161/ATVBAHA.109.187450.

[81] M. Madsen, N. Feidenhans'l, P.-E. Hansen, J. Garnaes, and K. Dirscherl. Accounting for PDMS shrinkage when replicating structures. *Journal of Micromechanics and Microengineering*, 24(12):127002, 2014. doi: 10.1088/0960-1317/24/12/127002.

[82] H. Wu, T. Odom, D. Chiu, and G. Whitesides. Fabrication of Complex Three-Dimensional Microchannel Systems in PDMS. *Journal of the American Chemical Society*, 125(2):554–9, 2003. doi: 10.1021/ja021045y.

[83] D. B. Wolfe, J. C. Love, and G. M. Whitesides. *Nanostructures Replicated by Polymer Molding*, pages 2657–66. Marcel Dekker, Inc., New York, 2004. doi: 10.1201/9781439834398.ch174. 893.

[84] C. Moraes, Y. Sun, and C. Simmons. Solving the shrinkage-induced PDMS alignment registration issue in multilayer soft lithography. *Journal of Micromechanics and Microengineering*, 19(6):065015, 2009. doi: 10.1088/0960-1317/19/6/065015.

[85] D. J. Stephens and V. J. Allan. Light Microscopy Techniques for Live Cell Imaging. *Science*, 300 (5616):82–86, 2003. doi: 10.1126/science.1082160.

[86] R. McGorty, D. Kamiyama, and B. Huang. Active Microscope Stabilization in Three Dimensions Using Image Correlation. *Optical Nanoscopy*, 2(1):3, 2013. doi: 10.1186/2192-2853-2-3.

[87] A. Balinovic, D. Albrecht, and U. Endesfelder. Spectrally red-shifted fluorescent fiducial markers for optimal drift correction in localization microscopy. *Journal of Physics D: Applied Physics*, 52(20): 204002, 2019. doi: 10.1088/1361-6463/ab0862.

[88] J. Keys, A. Windsor, and J. Lammerding. *Assembly and Use of a Microfluidic Device to Study Cell Migration in Confined Environments: Methods and Protocols*, volume 1840, pages 101–118. 2018. ISBN 978-1-4939-8690-3. doi: 10.1007/978-1-4939-8691-0_10.

[89] B. Nath, A. P. Bidkar, V. Kumar, A. Dalal, M. K. Jolly, S. S. Ghosh, and G. Biswas. Deciphering Hydrodynamic and Drug-Resistant Behaviors of Metastatic EMT Breast Cancer Cells Moving in a Constricted Microcapillary. *Journal of Clinical Medicine*, 8(8), 2019. doi: 10.3390/jcm8081194.

[90] A. Adamo, A. Sharei, L. Adamo, B. Lee, S. Mao, and K. Jensen. Microfluidics-Based Assessment of Cell Deformability. *Analytical chemistry*, 84(15):6438–43, 2012. doi: 10.1021/ac300264v.

[91] P. Friedl, K. Wolf, and J. Lammerding. Nuclear mechanics during cell migration. *Current Opinion in Cell Biology*, 23(1):55–64, 2011. doi: 10.1016/j.ceb.2010.10.015.

[92] H. R. Thiam, P. Vargas, N. Carpi, C. Lage, M. Raab, E. Terriac, M. King, J. Jacobelli, A. Alberts, T. Stradal, A.-M. Lennon-Dumenil, and M. Piel. Perinuclear Arp2/3-driven actin polymerization enables nuclear deformation to facilitate cell migration through complex environments. *Nature Communications*, 7:10997, 2016. doi: 10.1038/ncomms10997.

[93] K. Hu, L. Ji, K. T. Applegate, G. Danuser, and C. M. Waterman-Storer. Differential Transmission of Actin Motion Within Focal Adhesions. *Science*, 315(5808):111–115, 2007. doi: 10.1126/science.1135085.

[94] J. Valli and J. Sanderson. Super-Resolution Fluorescence Microscopy Methods for Assessing Mouse Biology. *Current Protocols*, 1(8):e224, 2021. doi: 10.1002/cpz1.224.

Appendix A

Additional Materials

A.1 LEGO® pieces used for the assembly of syringe pumps

Name	Picture	Part	Quantity
BRICK 1X2 WITHOUT PIN	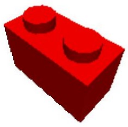	3065	16
BRICK 1X2 WITHOUT PIN		3065	16
BRICK 2X2		3003	64
BRICK 2X2		3003	32
BRICK 2X3		3002	8
BRICK 2X4		3001	8
BRICK 2X6	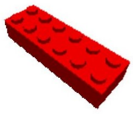	44237	16
BRICK 2X8		3007	8
TECHNIC BRICK 1X6, Ø4,9	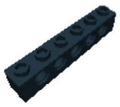	3894	16
TECHNIC BRICK 1X6, Ø4,9	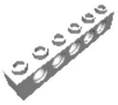	3894	24

Figure A.1: Part 1 of list of LEGO® pieces used to assemble eight pumps fully made of LEGO®.

Name	Picture	Part	Quantity
TECHNIC BRICK 1X10 Ø4.9		2730	32
TECHNIC BRICK 1X10 Ø4.9	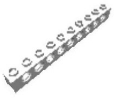	2730	48
PLATE 2X3		3021	8
PLATE 2X3		3021	8
PLATE 2X4	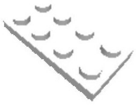	3020	56
PLATE 2X4	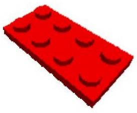	3020	32
PLATE 2X6	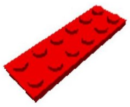	3795	8
PLATE 2X6		3795	16
PLATE 2X16	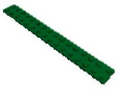	4282	20
PLATE 8X16	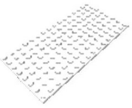	92438	9

Figure A.2: Part 2 of list of LEGO® pieces used to assemble eight pumps fully made of LEGO®.

Name	Picture	Part	Quantity
PLATE 8X16	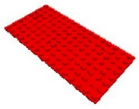	92438	9
PLATE 8X16		92438	6
PLATE 8X16		92438	17

Figure A.3: Part 3 of list of LEGO® pieces used to assemble eight pumps fully made of LEGO®.

Name	Picture	Part	Quantity
FUNC. MOTOR 24X6M	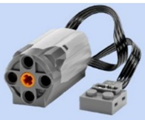	58120	8
BUSH FOR CROSS AXLE	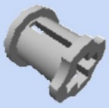	6590	56
BEAM 1X2 W/CROSS AND HOLE	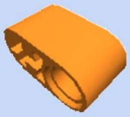	60483	32
CROSS AXLE 6M		3706	24
CROSS AXLE 7M		44294	16
CROSS AXLE 8M		3707	24
CROSS AXLE 12M		3708	8

Figure A.4: Part 4 of list of LEGO® pieces used to assemble eight pumps fully made of LEGO®. Part 1 of list of LEGO® pieces used to assemble four pumps built with 3D-printed structures (half of the quantity of pieces shown for each part type).

Name	Picture	Part	Quantity
Linear Actuator 10-15 M		61927	16
GEAR WHEEL T=8, M=1	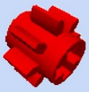	3647	8
GEAR WHEEL T=8, M=1		3647	16
GEAR WHEEL Z24	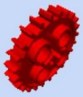	3648	16
GEAR WHEEL 40T	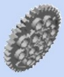	3649	16

Figure A.5: Part 5 of list of LEGO$^{®}$ pieces used to assemble eight pumps fully made of LEGO$^{®}$. Part 2 of list of LEGO$^{®}$ pieces used to assemble four pumps built with 3D-printed structures (half of the quantity of pieces shown for each part type).